AUGUST CHEŁKOWSKI INSTITUTE OF PHYSICS
FACULTY OF SCIENCE AND TECHNOLOGY
UNIVERSITY OF SILESIA IN KATOWICE

Angelina Łobejko

Experimental studies of the three nucleon system dynamics in the proton induced deuteron breakup at 108 MeV.

Ph.D. Thesis

Supervisor:

dr hab. Elżbieta Stephan, prof. UŚ

Co-supervisor:

dr Andrzej Wilczek

CHORZÓW 2022

Abstract

Studies of few-nucleon systems form the basis for understanding nuclear interactions and enable precise tests of the theoretical models. This work focuses on the experimental studies of the proton-deuteron breakup reaction at the beam energy of 108 MeV. The main goal was to determine the differential cross-section for this reaction.

The experiment was conducted in 2016 in collaboration with physicists from the University of Silesia, Jagiellonian University, Warsaw University, the Institute of Nuclear Physics of the Polish Academy of Sciences, and the Kernfysich Versneller Institute (KVI, University of Groningen, the Netherlands). For this purpose, the BINA detection system has been transported from KVI and successfully installed at Cyclotron Center Bronowice. This work concentrates on data registered by the BINA detector at the proton beam energy of 108 MeV, with the use of a liquid deuterium target. This measurement was a part of the broader program focused on testing the three-nucleon system dynamics at beam energies of 108, 135, and 160 MeV.

To determine the differential cross section, the experimental data were pre-selected, and a number of methods were applied to reconstruct the particle angles, identify particles, perform the energy calibration, and determine the efficiency of individual elements of the detection system. The data were normalized to the luminosity determined from a number of registered deuterons and the known cross section for a proton-deuteron elastic scattering.

This work presents differential cross sections for the breakup reaction for a set of 252 angular configurations of outgoing protons in the range of polar angles from 13 to 27 degrees, which gives 1767 data points. The experimental results are compared to the state-of-the-art theoretical calculations based on the CD-Bonn potential, considering the Three Nucleon Force (3NF) effects and Coulomb interactions between protons. The quality of the data description was determined by performing the chi-square test. The results show a significant influence of Coulomb interactions, while the effects of 3NF for the analyzed configurations are negligible.

Streszczenie

Pomiary obserwabli dla reakcji w układach kilku nukleonów umożliwiają precyzyjne testy modeli oddziaływań jądrowych. Niniejsza praca dotyczy eksperymentalnych badań reakcji rozbicia (breakupu) deuteronu przy energii wiązki protonowej wynoszącej 108 MeV. Jej celem było wyznaczenie różniczkowego przekroju czynnego na powyższą reakcję w szerokim zakresie przestrzeni fazowej.

Eksperyment został przeprowadzony w 2016 roku we współpracy grupy fizyków z Uniwersytetu Śląskiego, Jagiellońskiego, Warszawskiego oraz Instytutu Fizyki Jądrowej PAN i Kernfysich Versneller Instytut (KVI, Uniwersytet w Groningen, Holandia). Pomiaru dokonano za pomocą detektora BINA dla wiązki protonowej 108 MeV rozpraszanej na ciekłej tarczy deuteronowej. Dane będące podstawą niniejszej pracy zostały zebrane w pierwszym eksperymencie po przewiezieniu detektora z KVI i zainstalowaniu w Centrum Cyklotronowym Bronowice. Pomiary te stanowiły część szerszego programu badań układów trzech nukleonów przy energiach wiązki 108, 135 i 160 MeV.

W celu wyznaczenia różniczkowego przekroju czynnego dane eksperymentalne zostały poddane wstępnej selekcji, a następnie zastosowano szereg metod mających na celu zrekonstruowanie kątów cząstek, ich identyfikację, kalibrację oraz wyznaczenie wydajności poszczególnych elementów układu detekcyjnego. Ostatecznie przekrój czynny został znormalizowany poprzez wyznaczenie świetlności wiązki na podstawie liczby deuteronów pochodzących z rozpraszania sprężystego o znanym przekroju czynnym.

W pracy zaprezentowano różniczkowe przekroje czynne na reakcję breakupu dla zestawu 252 konfiguracji kątowych wylatujących protonów w zakresie kątów polarnych od 13 do 27 stopni, co daje 1767 punktów pomiarowych. Dane zostały porównane z dostępnymi obliczeniami teoretycznymi bazującymi na potencjale CD-Bonn, uwzględniającymi też inne przyczynki do dynamiki układu, jak siła trójnukleonowa (3NF), czy odpychanie kulombowskie między protonami. Jakość opisu danych określano na podstawie testu chi-kwadrat. Otrzymane wyniki uwidaczniają znaczny wpływ sił kulombowskich, a efekty 3NF dla analizowanych konfiguracji są znikome.

Contents

Chapter 1

Introduction

The Standard Model is the theory classifying elementary particles and describing almost all the observed interactions (except for gravity) as three elementary forces: electromagnetic, strong, and weak. The nuclear forces at the fundamental level emerge from the strong interaction described in the framework of quantum field theory called Quantum Chromodynamics (QCD). The strong force is mediated by the massless gauge bosons called gluons between the massive quarks, which constitute, in particular, the building blocks of nuclei (protons and neutrons). Despite the remarkable success of QCD at high energies, the theory cannot be applied for intermediate energies due to the so-called asymptotic freedom (i.e., quarks interact weakly only at high energies, allowing perturbative calculations). Thus, we need to use different methods to explain the interactions between nucleons at lower energies.

The first approach focuses on the so-called realistic potentials between two nucleons (2N). The interaction is based on the meson exchange theory proposed by Yukawa [1] and the semi-phenomenological approaches. The recent models proposed within this framework reproduce the nucleon-nucleon scattering data with impressive precision. Among them are Charge Dependent Bonn, Argonne v18, or Nijmegen I and II. The second approach, the so-called Chiral Effective Field Theory (ChEFT), is based on the general effective Lagrangian for goldstone bosons (pions) and matter fields (nucleons and perhaps Δ barions). The ChEFT is consistent with the (approximate) chiral symmetry of QCD and the other symmetries like parity and charge conjugation [2].

Whereas the realistic potentials very well reproduce the experimental data for the systems consisting of only two nucleons, the natural next step is to test them in the more complex systems. The simplest one, however nontrivial, is the system with three nucleons (3N). It turned out that the precise theoretical prediction limited to 2N interaction does not reproduce even the binding energy of the ^3H and ^3He [3]. The existing significant discrepancies can be explained by the additional dynamics related to the presence of the third nucleon, called the three-nucleon force (3NF). Contrary to the

1
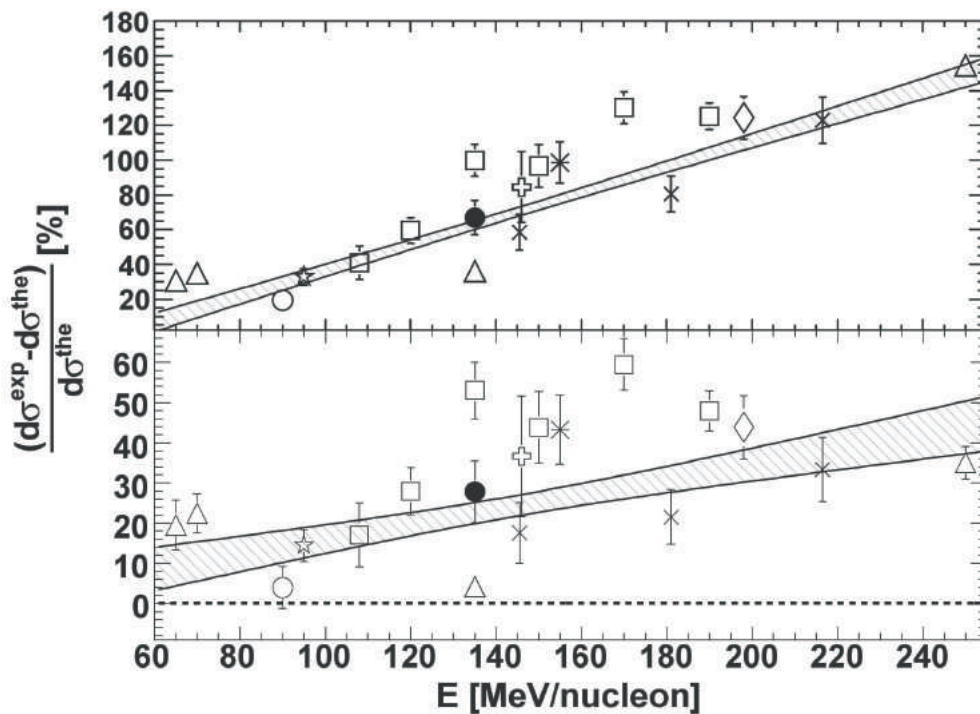
Fig. 1.1: The relative difference between the calculations by the Hannover-Lisbon theory group and the measured cross sections for the elastic $p+d$ scattering as a function of beam energy for $\theta_{CM} = 140°$ (for references to the data, see [11]). The top panel shows the differences when using the calculation based on the CD-Bonn potential and the Coulomb interaction, whereas for the bottom panel, an additional Δ isobar, inducing 3NF, has been taken into account. The band represents the result of a linear fit to the data, excluding the results obtained at 135 MeV. The width of the band corresponds to a 2σ error of the fit. Figure adopted from [11].

semi-phenomenological potentials, in the Chiral Effective Field Theory, the 3NF naturally appears in the next-to-next-to-leading order (NNLO). In the last few years, there has been significant progress towards calculations within Chiral Effective Field Theory [4–7].

The importance of 3NF implementation for systems of more than two nucleons was confirmed by solving the problem of cross section discrepancy for the nucleon-deuteron elastic scattering [8, 9] and describing the binding energies of ^3H and ^3He correctly [10]. The proton-deuteron elastic scattering at intermediate energies reveals significant sensitivity to 3NF effects. Fig. 1.1, *upper panel* shows that calculations based only on 2N interaction fail to reproduce experimental data at backward angles (c.f. at $140°$). The discrepancy is strongly reduced after including 3NF (Fig. 1.1, *lower panel*), however, a residual difference between the measured and calculated cross sections is still sizeable. It reveals a systematic increase with the proton energy leaving serious doubts concerning the completeness of the applied theory.

It is very intriguing whether, at such low energies, this trend can be explained by relativistic effects, although the first attempts at relativistic calculations predict influence on the elastic scattering cross section much too small to be responsible for the observed discrepancy and revealing its influence in

different kinematic regions [12–14]. Apart from deficiencies in the theoretical descriptions, also the experimental picture is not perfectly clear. Measurements at 135 MeV [11, 15–17] (see Fig. 1.1) are not consistent with each other, and those at higher energies demonstrate considerable discrepancies with theory, significantly above the linear trend approximation, shown in Fig. 1.1.

The constant development of theoretical calculations for a three-nucleon system comprises also: incorporating screened Coulomb interaction [18, 19], combining 3NF with such a Coulomb interaction [20], and calculations in a relativistic approach [13]. The impact of Coulomb interaction and relativistic effects on elastic scattering cross section is very small. The situation changes significantly when one studies the deuteron breakup in collision with a proton. This reaction is very interesting as a field of study since the three-body final state is rich in kinematic configurations revealing diverse sensitivity to specific effects. The sensitivity to 3NF was shown for a deuteron beam energy of 65 MeV/nucleon and 80 MeV/nucleon [21–23]. Moreover, a predicted huge influence of the Coulomb interaction [18, 19] was experimentally confirmed [24–26], even at energies as high as 170 MeV/nucleon. [27]. According to the theoretical prediction, the Coulomb effects barely depend on beam energy, and they are very significant for pp pair final state interaction (FSI). The cross-section's description is improved by extending theoretical models with both 3NF and Coulomb interaction [20]. For deuteron beam energy of 130 MeV (65 MeV/nucleon), the improvement of results in all phase space of a detector was recorded [25].

The relativistic approach is another current issue in the theoretical description of the 3N systems. Contrary to the elastic scattering calculations, the breakup reaction reveals a very strong cross section sensitivity to relativistic effects. At 200 MeV, the differential cross section for specific configurations is modified by a factor of 40% and even more [13]. So far, there is no direct confirmation of this modification by the experimental data. In certain configurations, a discrepancy rises with energy and is not removed by the relativistic calculations [23, 27].

So far, there are no calculations including all the dynamic ingredients; therefore, the database covering large reaction phase space and a wide range of beam energies is necessary to single out the particular effects in the range of their maximum visibility. The old data sets for deuteron breakup in collision with proton were usually taken with very limited angular acceptance [28–32]. Only recently, large detectors combined with modern data acquisition systems facilitate experiments covering large phase space regions, providing favorable conditions for controlling the systematic uncertainties. A series of experiments performed at KVI Groningen using SALAD and BINA detectors and FZ-Jülich with GeWall and WASA detectors founded the database of the breakup reaction following the approach of broad phase space coverage. The summary of the experimental data measured with the large acceptance detector is presented in Table 1.1.

Experimental overview with the large acceptance detector					
Detector	**Laboratory**	**Detector Acceptance**	**Reaction beam/target**	**Energy [MeV/nucleon]**	**Observables**
Ge-Wall	FZ-Jülich	$5° - 13°$	dp	65 [33, 34]	σ, A_x^d, A_y^d
WASA		4π	dp	150, 170 [27], 190, 200	σ
SALAD	KVI	$10° - 35°$	dp	65 [22, 35]	$\sigma, A_x^d, A_y^d,$
BINA		4π	dp	50 [36]	A_{xx}, A_{xy}, A_{yy}
				65 [26], 80 [23, 37]	σ
			pd	135 [38–40], 190 [41, 42]	σ, A_x^d, A_y^d
BINA	CCB	4π	pd	108, 135, 160	σ

Table 1.1: The summary of the experimental data measured for the proton-deuteron breakup reaction with the large acceptance detectors.

The accelerators providing proton and deuteron beams at intermediate energies (where the theoretically predicted 3NF effects are significant and below the pion production threshold) have recently almost vanished in Europe. Fortunately, since 2013 the Cyclotron Center Bronowice (CCB) at the Institute of Nuclear Physics PAS, Kraków, has been providing proton beams for the therapy of patients and nuclear physics research, offering a unique opportunity to continue the studies of three- and four-nucleon systems.

This work focuses on the experimental studies of the proton-deuteron breakup reaction at the beam energy of 108 MeV carried out in CCB as a part of the broader program focused on testing the three-nucleon system dynamics at beam energies of 108, 135, and 160 MeV. In the following, we point out the motivation for choosing those energies:

- 108 MeV: There exist data for the elastic scattering, in good agreement with the 3NF calculations, but no data for the breakup reaction. The main goal was to determine the differential cross section for ^{2}H(p,pp)n with the relative normalization of it to the known cross section of the elastic scattering ^{2}H(p,pd) [43].

- 135 MeV: There exist data for both the elastic scattering and breakup reaction. However, there is a discrepancy in the elastic scattering data for different experiments, especially in the region sensitive to 3NF. We concentrate on collected data for the elastic scattering to verify the existing data.

- 160 MeV: There is neither data for the elastic scattering nor the breakup reaction. We are interested in this energy since we expect a significant contribution from 3NF and the relativistic effects.

The thesis is organized in the following way: the theoretical background of the three-nucleon system is briefly described in Chapter 2. The experimental program and the detection setup description are contained in Chapter 3. Chapter 4 describes the data analysis procedures for charged particles. The breakup reaction analysis is presented in Chapter 5. Chapter 6 is devoted to the obtained differential cross section results and their qualitative and quantitative comparison with the theoretical calculations. The summary and outlook are given in the last chapter.

Chapter 2

Theoretical background

Due to the experimental character of the presented work, this chapter contains only the most basic information on the theoretical description of the few-nucleon interactions. It includes a brief description of the kinematical properties of the elastic scattering and three-body breakup reaction, followed by an overview of the existing models of nucleon-nucleon (NN) interactions and three-nucleon forces (3NF). The overview is concluded with information about the developments introducing Coulomb and relativistic effects.
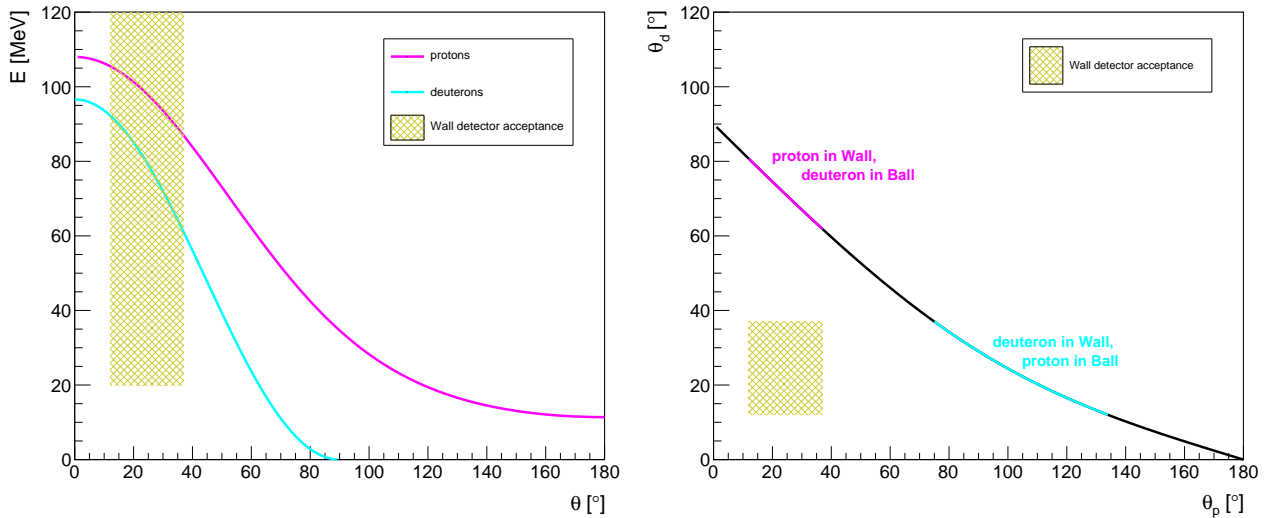
2.1   Kinematic relation

When the proton beam interacts with the deuteron target, we can register two kinds of reactions between hadrons: elastic scattering and the breakup process. Since we have a fixed target (the initial deuteron momentum is zero), the laboratory frame of reference (LAB) is the most convenient for describing the reaction kinematics. Hence, the system center is set in the center of the target, while the beam direction defines the Z-axis.

From the perspective of our experimental setup, we measure two charged particles in the final state: two protons from the breakup reaction and proton-deuteron pair from the elastic scattering. We define the angular relations in such a system to have complete information about the events of interest. The polar angles θ_1 and θ_2 are expressed as angles between the Z-axis and the direction of the outgoing particles' momenta. The azimuthal angles φ_1 and φ_2 are defined between the X-axis and the projection of the particle trajectory onto the XY plane. In accordance, the relative azimuthal angle is introduced as $\varphi_{12} = \varphi_1 - \varphi_2$. We will neglect the sign and use the definition $\varphi_{12} = |\varphi_1 - \varphi_2|$.

2.1.1 Elastic scattering

In the elastic scattering process, the particles collide and exchange momentum with each other, although the types of particles remain constant after the interaction. In the analyzed experiment, a proton beam hits a fixed deuteron target, so the particles in the initial state can be characterized by their mass and momentum, where m_p and p_p refer to the mass and momentum of the proton, whereas m_d and $p_d = 0$ to the deuteron. The momentum conservation law imposes a condition that the momenta of the outgoing particles have to be in one plane, making the relative azimuthal angle between them equal to $\varphi_{12} = 180°$. To fully describe the final state of all particles in the elastic scattering reaction (with known masses), we need information about one kinematic variable. Consequently, the θ angle of one particle determines the momenta and energies of both particles in their final state. The kinematic relations are presented in Fig. 2.1. In our detection setup, we register only one particle from elastic scattering in the forward part - Wall ($\theta < 35°$), while the coincident particle is scattered to the backward - Ball ($\theta > 40°$), see *Right panel* in Fig. 2.1. Due to the kinematic relation of proton and deuteron momentum, studying elastic scattering is an effective tool for verifying the system's geometry.

Fig. 2.1: Kinematic relations describing the *pd* elastic scattering at 108 MeV. The yellow dashed area corresponds to the acceptance of the Wall. *Left panel*: The energy of elastically scattered protons and deuterons as a function of their polar angle θ. *Right panel*: The relations between polar angles of deuteron vs. proton. The lack of Wall-Wall coincidences is clearly visible.

2.1.2 Three-body breakup

In the ^{2}H(p,pp)n reaction, the deuteron is broken after a collision with the proton, resulting in three particles in the final state: two protons and a neutron. The momenta of each outgoing particle $\vec{p_1}$, $\vec{p_2}$,

and $\vec{p_3}$ give us nine kinematic variables and define the final state. However, from the experimental perspective, it is more convenient to use a directly measured set of kinematic variables: the kinetic energies and both angles of each particle - polar θ and azimuthal φ. Within the introduced spherical coordinate system, we have the following relations defined in a non-relativistic way:

$$E_k = \frac{p_k^2}{2m}$$
$$\vec{p_k} = p_k(\cos\varphi_k\sin\theta_k, \sin\varphi_k\sin\theta_k, \cos\theta_k), \qquad (2.1)$$

where $k = 1, 2, 3$ and $p_k = |\vec{p_k}|$. In the above relation, we assume that the proton and neutron masses are approximately the same and equal m. Thus, according to energy and momentum conservation laws, the 9-dimensional momentum space can be reduced to a 5-dimensional phase space.

$$E_p = E_1 + E_2 + E_3 + Q,$$
$$\vec{p_p} = \vec{p_1} + \vec{p_2} + \vec{p_3}. \qquad (2.2)$$

E_p and $\vec{p_p}$ are the kinetic energy and momentum of the incident proton, while the E_1, E_2, E_3, and $\vec{p_1}, \vec{p_2}$, and $\vec{p_3}$ refer to the kinetic energies and momenta of outgoing particles. The Q value is the absolute value of the deuteron binding energy: $Q = 2.224$ MeV.

Due to the relation of energy and momentum conservation laws, we can eliminate the neutron kinematic variables and define the energy relation of the two protons as follows:

$$E_1 + E_2 - \sqrt{E_p E_1}\cos\theta_1 - \sqrt{E_p E_2}\cos\theta_2 + \sqrt{E_1 E_2}\cos\theta_{12} + \frac{Q}{2} = 0 \qquad (2.3)$$

where $\cos\theta_{12} = \cos\theta_1\cos\theta_2 + \sin\theta_1\sin\theta_2\cos\varphi_{12}$. According to Eq. (2.3), for a given angular configuration θ_1, θ_2, and φ_{12}, we can obtain a single curve on the E_1 vs. E_2 plane, the so-called kinematic curve. Fig. 2.2 shows the E_2 vs. E_1 relation for a few selected angular configurations for the pd breakup reaction. In this case, relativistic calculations were performed, and real masses of all nucleons were taken into account. Due to the energy relation of both protons, we apply one kinematic S-variable combining both energies. It is defined as the arc length measured along the kinematic curve with the starting point $S = 0$ chosen arbitrarily at the point where the energy of the second proton reaches the minimum, see Fig. 2.2.
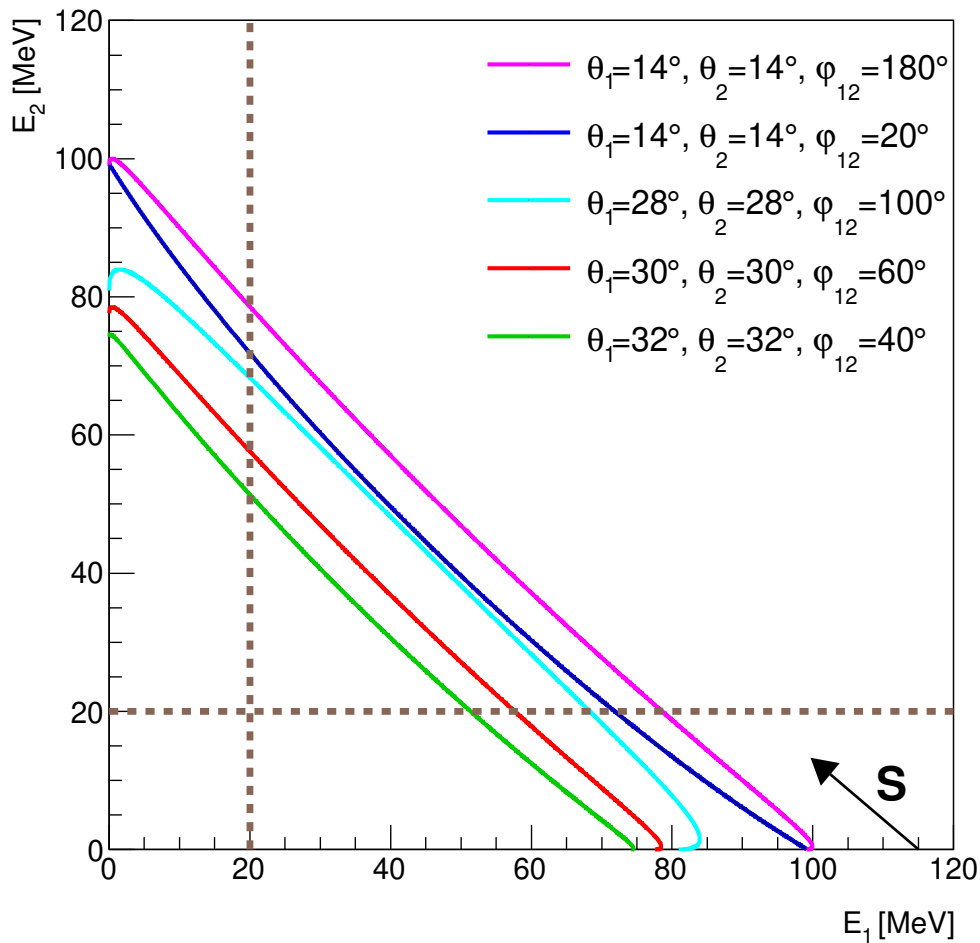
Fig. 2.2: A set of kinematic curves for several angular configurations (specified in the legend) of proton pairs from the breakup reaction at 108 MeV. The kinematic variable S, defined in the text, is graphically represented by an arrow.

2.2 The theoretical background of a few nucleon interactions

Due to the impossibility of describing nuclear interactions in the low and intermediate energy region in the QCD formalism, two different approaches are taken. In the first approach, so-called realistic potentials are constructed, i.e., semi-phenomenological models based on the meson-exchange picture. The Effective Field Theory (ChEFT) is the newest approach, based on the general effective Lagrangians for goldstone bosons (pions) and matter fields (nucleons). Both approaches provide a precise description within their framework, reproducing the nucleon-nucleon scattering data with impressive precision.

Concerning the three-nucleon system (3N) examined in this work, a special theoretical framework is required. The main technique to accurately calculate scattering observables for 3N systems was

developed by Faddeev [44]. In particular, the method provides a unique solution and convergence for its numerical discretized form. Based on this method, the cross-sections for the breakup reaction recently were calculated by different research groups, with the realistic NN potentials as well as with the three-nucleon force models described below.

2.2.1   Realistic potentials

The models of NN potential like Charge Dependent Bonn (CD-Bonn) [45, 46], Argonne v18 (Av18) [47], Nijmegen I and II [48], or Reid93 [48] express the long-range interaction due to the meson-exchange theory, first proposed by Yukawa [1], while the short-range component is phenomenological. Free parameters existing in these models are fitted to the experimental nucleon-nucleon scattering data with impressive precision. An exemplary shape of a few of them is presented in Fig. 2.3.
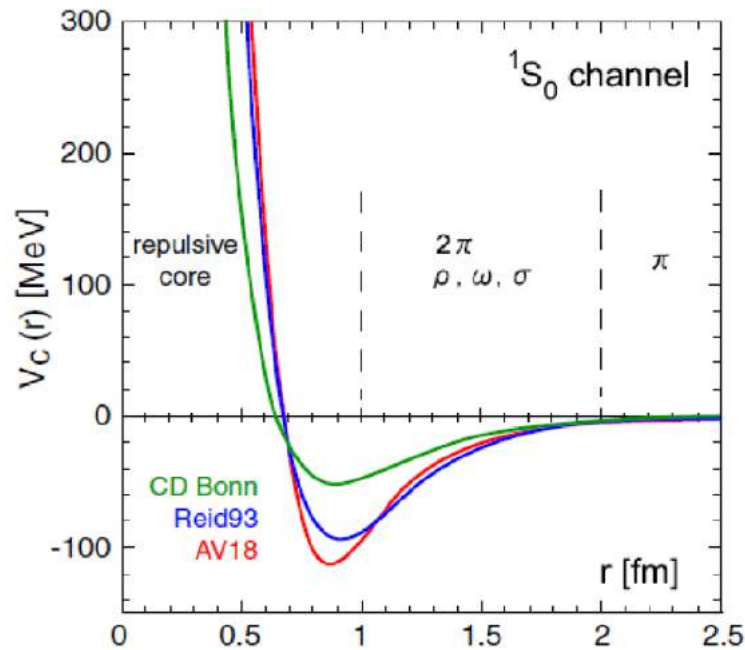

Fig. 2.3: Few models of NN potential: CD-Bonn, Reid93, and Av18. The differences in shape depict the various theoretical approaches to calculations. Figure adopted from [49].

One of the most widely used is the CD-Bonn potential. The charge dependence of the present potential is based upon the predictions by the Bonn full model for charge symmetry and charge-independence breaking in all partial waves with J<4 [46]. The potential is represented in terms of the covariant Feynman amplitudes for one-boson exchange, which are nonlocal. In the CD-Bonn model, the long-range part is determined by π mesons, while a ω meson describes the short-range component and the spin-orbit interaction. The 2π exchange mechanism defines the intermediate range.

2.2.2 Three-nucleon force models

The realistic potentials use nucleons and mesons as degrees of freedom. Due to the neglect of the internal structure of nucleons, the impact of suppressed degrees of freedom on observables in any system consisting of more than two nucleons is interesting. One may propose the additional dynamics related to the presence of the third nucleon, the so-called three-nucleon force (3NF), which cannot be reduced to the pairwise interactions. Historically, the first 3NF model was proposed by Fujita and Miyazawa [50], which is schematically presented in Fig. 2.4, *left panel*. In this interaction, there is a two-pion (2π) exchange - the first pion is exchanged between two nucleons leading to the excitation of the Δ-isobar particle, which, when decaying, exchanges the pion with the third nucleon. Nowadays, there are many models including the 3NF. The most popular are briefly described below.
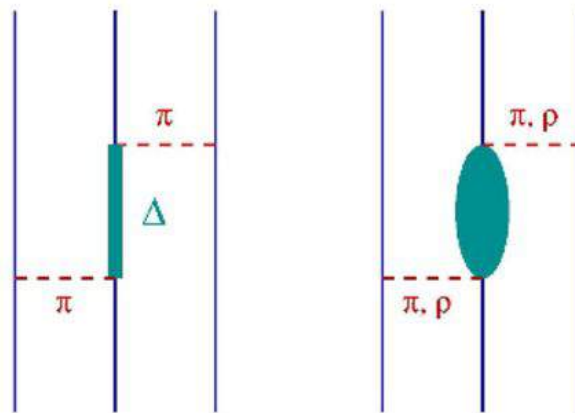
Fig. 2.4: The schematic presentation of the first 3NF model proposed by Fujita and Miyazawa as a two-pion exchange. Figure adopted from [51].

- Tucson-Melbourne

  The Tucson-Melbourne 3NF model [52, 53] is one of the most popular theoretical approaches. The latest version of the TM 3NF model, TM99, introduced by Coon and Han, is consistent with chiral symmetry [54] and uses more general algebra than p-wave πN scattering amplitude. This model has one free cut-off parameter Λ_{TM}, expressed in pion mass unit (m_π), which is selected for each combination of NN potentials in such a way to reproduce the ^3H binding energy [55].

- Urbana

  The Urbana IX model [56] is based on the Av18 potential and has been developed by the Urbana-Argonne collaboration to describe the properties of nuclear matter and light nuclei. The long-range component is the contribution of the 2π-exchange due to intermediate Δ excitation, while the short-range interaction is obtained phenomenologically based on the ^3H binding

energy and nuclear energy density. Illinois 3NF models [57] include parametrizations of three-pion (3π) exchange terms due to ring diagram (with one Δ), simultaneously containing the short-range phenomenological part. This model reproduces the binding energy of light nuclei to the mass A=12 with a satisfactory result [58]. Recently, a good description of the ^{16}O nucleus and problems to reproduce experimental data for the charge radius and the charge form factor for ^{40}Ca have been reported [59].

- Coupled-channel potential with Δ-isobar excitation

The two-baryon coupled channel potential (CCP) is developed and used in calculations by the Lisbon-Hanover group [60, 61]. It is based on the CD-Bonn potential with the exchange of $\pi, \rho, \omega,$ and σ mesons, which additionally considers the excitation of a single nucleon to the Δ-isobar. The Δ-isobar, apart from nucleons, is treated as an extra degree of freedom with a real mass of 1232 MeV. In this approach, the NN interaction is extended by including contributions between the NN and NΔ states, from the NΔ exchange - the ΔN potential and the direct interaction of the NΔ states (Fig. 2.5). Within this model, 3NF emerges naturally via the virtual excitation of the Δ-isobar in the 3N system. Moreover, it also contains the so-called two-nucleon dispersion (Fig. 2.6) when pions are exchanged between two nucleons only. Since those two contributions may compete with each other, the net effect is usually smaller than for other approaches including 3NF.
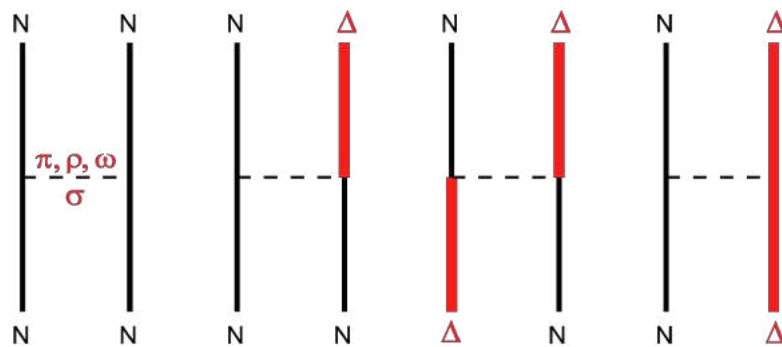
Fig. 2.5: Four channels considered in the construction of the CCP potential, which additionally, the excitation of a single nucleon to the Δ isobar is taken into account.
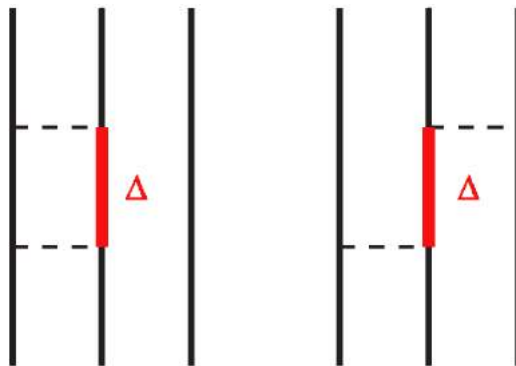
Fig. 2.6: Three-baryon effect arising within the CC approach: two-baryon dispersion (left) and the effective three-body force (right).

2.2.3 Chiral Effective Field Theory

The chiral Effective Field Theory, the ChEFT, is the newest approach to describing the interaction between nucleons at intermediate energies [62, 63]. It is based on the general effective Lagrangian for goldstone bosons (pions) and matter fields (nucleons and perhaps Δ's). The ChEFT is consistent with the (approximate) chiral symmetry of QCD and the other symmetries like parity and charge conjugation. In the ChEFT framework, the meson exchange is the long-range component, while the short-range part is described by the contact interaction between nucleons combined with low-energy constants (LEC's), the so-called hard core. By applying the ChEFT to the nucleon-nucleon scattering, one obtains an infinite number of Feynman diagrams. Weinberg first noted that ChEFT could be used to define a nuclear potential and summed to all orders using numerical techniques [64, 65]. Such constructed nuclear potential expands into a series as a function of the variable $(\frac{Q}{\Lambda})^v$, where Q is the nucleon momentum, and the constant Λ refers to the chiral symmetry breaking scale ($\sim$1 GeV). The v value indicates the next order of expansion that contains contributions from increasingly complex interactions. The most meaningful advantage of ChEFT over other methods is that the 3NF effect naturally appears in the next-to-next-to-leading order (NNLO, $v = 3$) consistently. The hierarchy of nuclear forces in ChEFT is schematically presented as a Feynman diagrams form in Fig. 2.7. This approach allows estimating the uncertainty of theoretical calculations, which is impossible in other methods.

In recent years, there has been significant progress in theoretical methods in ChEFT developed by LENPIC [66] (Low Energy Nuclear Physics International Collaboration). A new approach has been introduced by using an appropriate regularization in coordinate space, which maintains the analytic structure of the amplitude. It significantly reduces the cutoff parameters and better controls the uncertainties [67]. Currently, the so-called semi-local momentum-space regularized potentials (SMS) are the most precise NN forces [4]. The calculated observables based on SMS interactions up to N^{4}LO
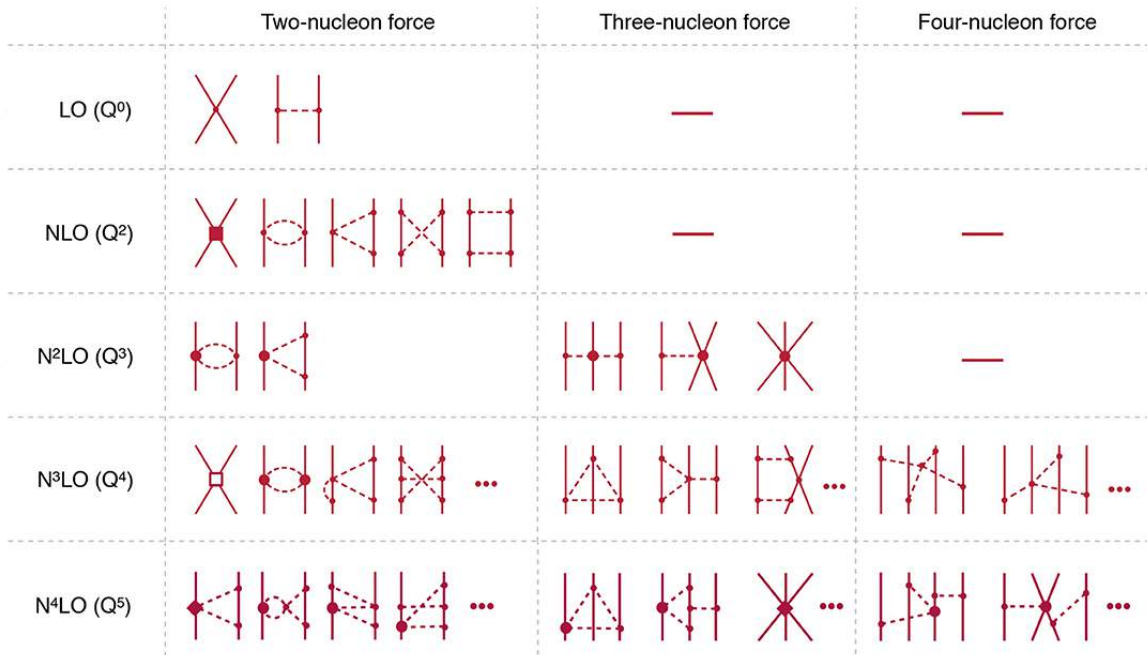
Fig. 2.7: The schematic presentation of the hierarchy of nuclear forces in chiral EFT shows as Feynman diagrams form. Solid and dashed lines denote nucleons and pions, respectively. Solid dots, filled circles, filled squares, filled diamonds, and open squares refer to the vertices of chiral dimensions equal to 0, 1, 2, 3, and 4, respectively. The first order when the 3NF appears naturally is an N^2LO. Figure adopted from [5].

described the np and pp data with a precision comparable to the phenomenological NN realistic potentials, while the number of adjustable parameters is, at the same time, reduced by about 40%. Contrary to the NN interactions, the contributions from 3NF have been calculated up to N^2LO [6]. The LECs appearing in 3NF have been determined from the binding energy of ^{3}H and pd cross section data [68]. The predicted Nd scattering observables are consistent with experimental data within errors. However, the results presented in Ref. [5] suggest that the high-precision description should require the chiral expansion of the 3NF up to N^4LO.

2.2.4 Coulomb interaction

The Coulomb phenomenon is very well understood, theoretically and experimentally, contrary to the interactions between three or even two nucleons. In the pd breakup reaction, we have three particles in the final state - two protons and one neutron, and taking into account the Coulomb interaction between charged particles is necessary. However, an infinite range of Coulomb interaction imposed a problem for the proton-deuteron theoretical calculation, which resulted in not considering it for many years. The Lisbon-Hanover group solved this problem by the idea of screening the Coulomb potential and correcting them with a renormalization technique to match the unscreened limit [19]. For the first time, Coulomb interactions were included in the pure CD-Bonn potential, then into its

CDB+Δ extension [18, 19], and later in calculations with the Av18 potential combined with the 3NF model - Urbana IX [20]. According to the theoretical prediction, the Coulomb effects barely depend on beam energy, and they are very significant for the pp pair, with a small relative azimuthal angle φ_{12}.

2.2.5   Relativistic effects

Until recently, all theoretical calculations of the observables were conducted non-relativistic. The first precise calculations considering the relativistic effect's contribution have been performed by a group of theoreticians led by H. Witała from the Jagiellonian University [12, 13]. The relativistic approach to 3N systems was developed using NN potentials, but what is more, it was extended by implementing a correction for calculations containing 3NF [14]. From the theoretical point of view, considering the relativistic effects requires including Lorentz's correction in the calculations of the NN potential and the relativistic form of the Lippmann-Schwinger equations. It is also necessary to include the kinematic effects coming from the relativistic factor of the phase space, as well as to properly treat the boost and rotation effects of Wigner spin states.

The magnitude of the relativistic effects on the cross section strongly depends on the region of the phase space increasing with the beam energy. At 200 MeV, the differential cross section for specific configurations is modified by a factor of 40% and even more. The role of relativistic effects, predicted to be significant even below 200 MeV/nucleon, is still under study [13].

Chapter 3

Experimental setup

The experiment was carried out at the Cyclotron Center of Bronowice (CCB) IFJ PAN in Cracow, Poland. The proton beam was provided by Proteus C-235 cyclotron at the kinetic energy of 108 MeV and was impinging on the liquid deuterium (LD_2) target. The reaction products were measured using the BINA (**B**ig **I**nstrument for **N**uclear Polarization **A**nalysis) detection system, designed to study the few-nucleon reactions at intermediate energies.

This chapter describes the main components of the experimental apparatus and the applied techniques.

3.1   Proton beam from Proteus C-235 Cyclotron

Proteus C-235 is an isochronous cyclotron with an energy selector which delivers an unpolarized proton beam of energy up to 230 MeV. The energy dispersion is $\Delta E/E < 0.7\%$, and the beam emittance is 11π mm rad and 12π mm mrad for horizontal and vertical direction, respectively. An integral part of this installation is an energy degrader and selector, allowing the beam energy to be downgraded continuously to 70 MeV, with intensities up to 600 nA. The beam energy is changed with a graphite absorber, and the energy switching time is ~ 1 second. The schematic view of the cyclotron facility located in CCB is visible in the *left panel* of Fig. 3.1.

For the purpose of the described experiment, the Proteus cyclotron delivered a proton beam with an energy of 108 MeV/nucleon. The beam spot was observed on the ZnS target and could be cut to the desired size by setting slits. The beam was positioned in the center of ZnS by changing the parameters of two quadrupole magnets, TDA01 (horizontally), and SGB01 (vertically), shown in Fig. 3.1, *right panel*. Since the beam has a significant halo, thus further optimization is required. It is based on

a slight modification of the magnets setting by observing the minimal rate in the scalers with an empty target cell. More information about cyclotron can be found in [69].
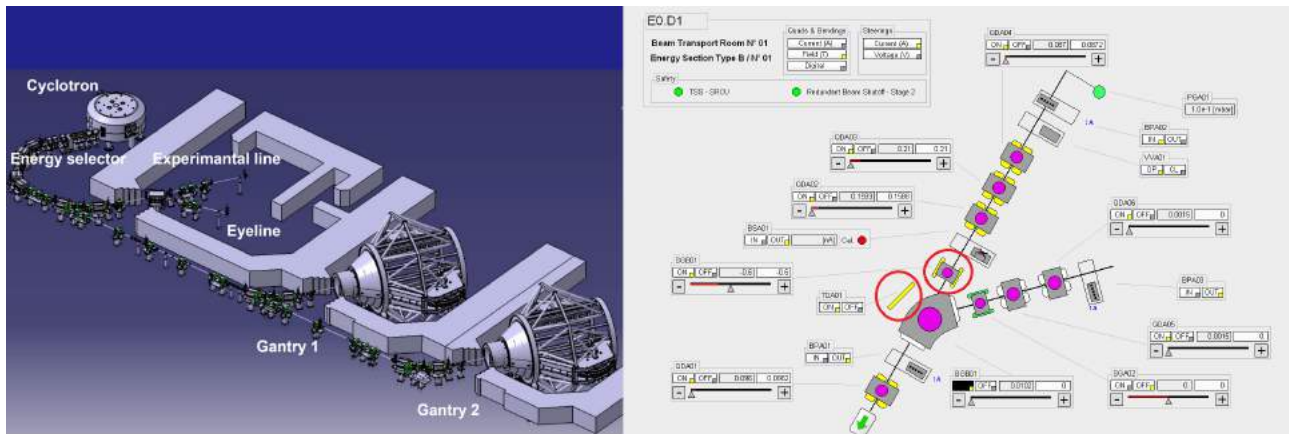
Fig. 3.1: *Left panel:* The schematic view of the cyclotron facility located in CCB. The beam delivered to the experimental hall is described as an experimental line in the picture. *Right panel:* Localization of the magnets mentioned in the text on the experimental beamline is marked by the red circles.
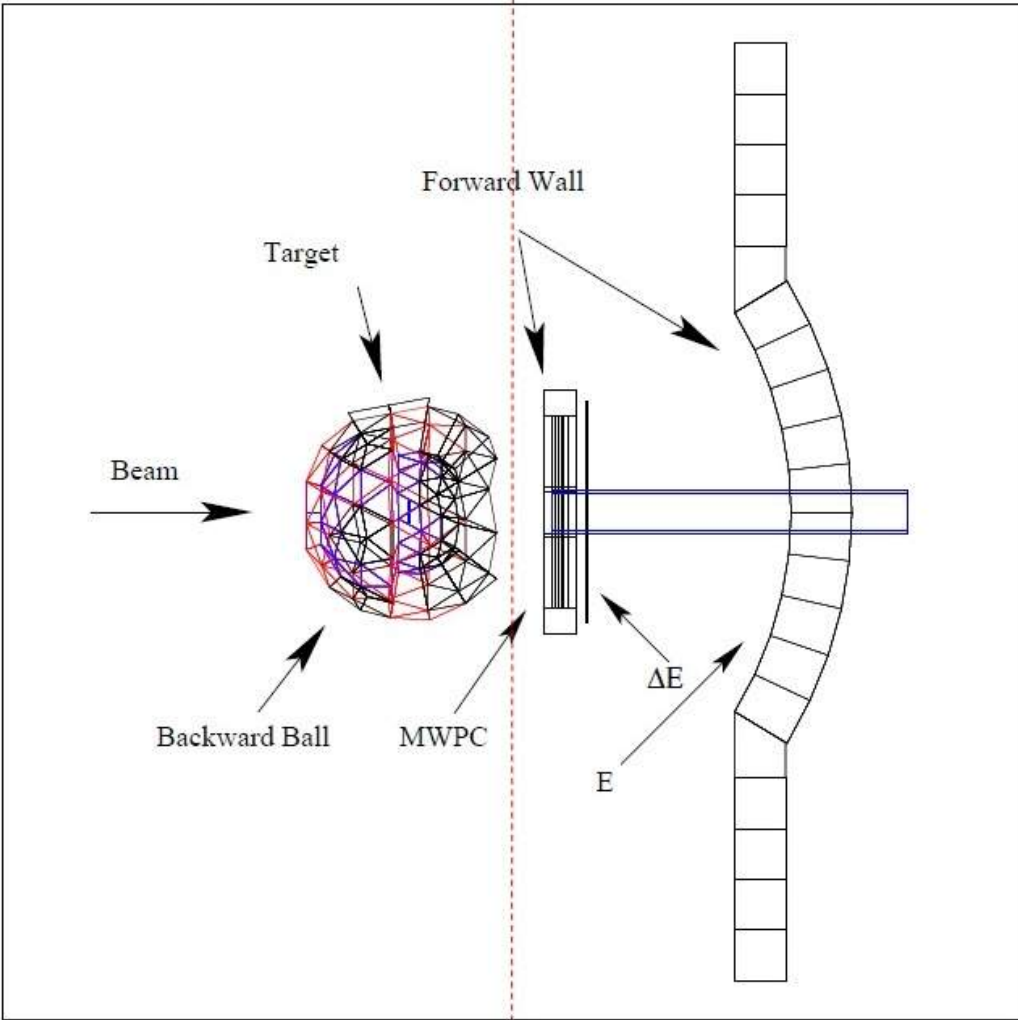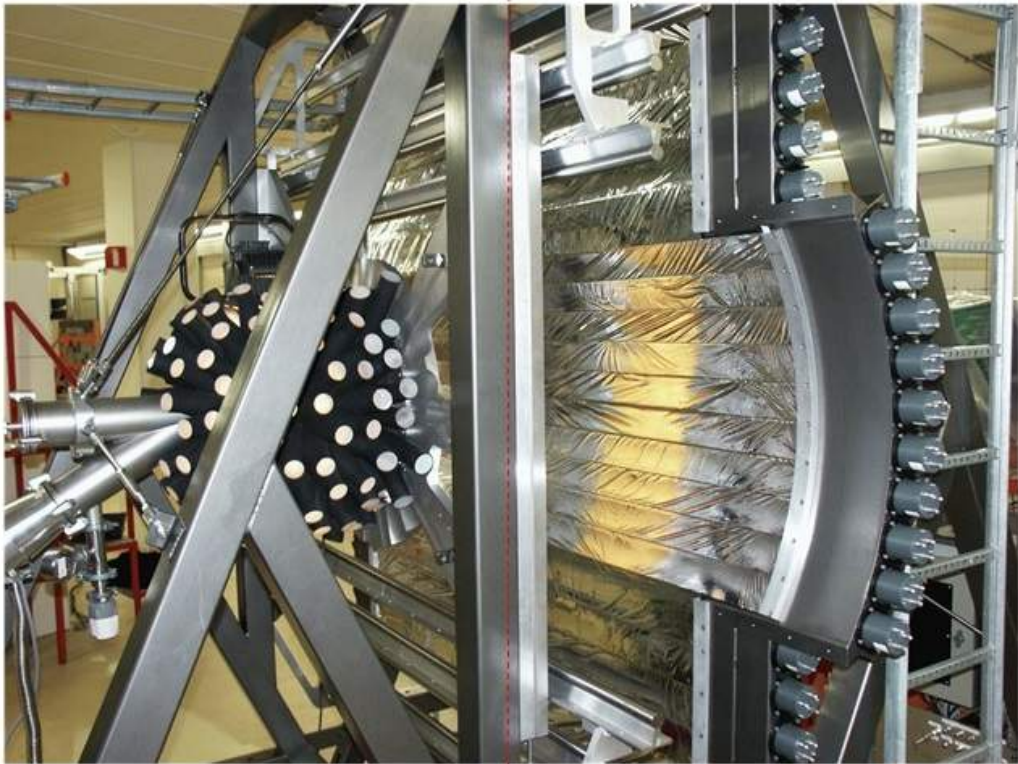
3.2   The BINA detector

The BINA detector was constructed at KVI (Netherlands) in 2004. During its operation at KVI, it provided rich sets of experimental data due to Polish-Dutch physicists collaboration. In 2012 the BINA setup was disassembled and transported from KVI to CCB, where it was successfully installed. Moreover, several tests and repairs have been made to improve the detector's operation. The made to the various parts of the BINA detector will be described in the following subsections.

The detection setup was designed to study elastic and breakup reactions at intermediate energies (between $\sim$ 25 - 180 MeV). It allows measuring the type of charged particle and its momentum. Furthermore, the BINA detector allows registration coincidences of two charged particles at nearly 4π solid angle. Study of an almost full phase-space of few-body scattering reaction is possible because of two parts of the detector: the forward Wall, covering the laboratory angles between $12° - 35°$ and the backward part - Ball - detecting particles with the angles $40° - 160°$. A brief description of each of them is in the subsection below, whereas more information and precise specification can be found in the Refs. [38, 41, 70, 71]. Unfortunately, during the first experimental run in CCB, only the forward part of the detector worked correctly. Because of this reason, the following thesis uses only data scattered into the Wall detector.

The side view of the whole detection system is presented in Fig. 3.2.

Fig. 3.2: The BINA Detection System. The upper panel presents a picture of the BINA detector, whereas the lower panel shows a schematic view from the same perspective. The figure is adopted from [71].

3.2.1 Forward Wall

The forward part of the detector Wall consists of a three-plane Multi-Wire Proportional Chamber (MWPC) and an array of almost square $\Delta E - E$ telescopes formed by two layers of scintillators (Fig. 3.3). Particles scattered in the forward direction can be measured with the polar angles θ between $13° - 29°$ in a whole azimuthal angle φ. Additionally, the polar angle can be extended up to $35°$ at the corners of a square-shaped MWPC region with only limited coverage of the azimuthal angles[1]. In Fig. 3.4, the corners are represented by the hatched orange area.
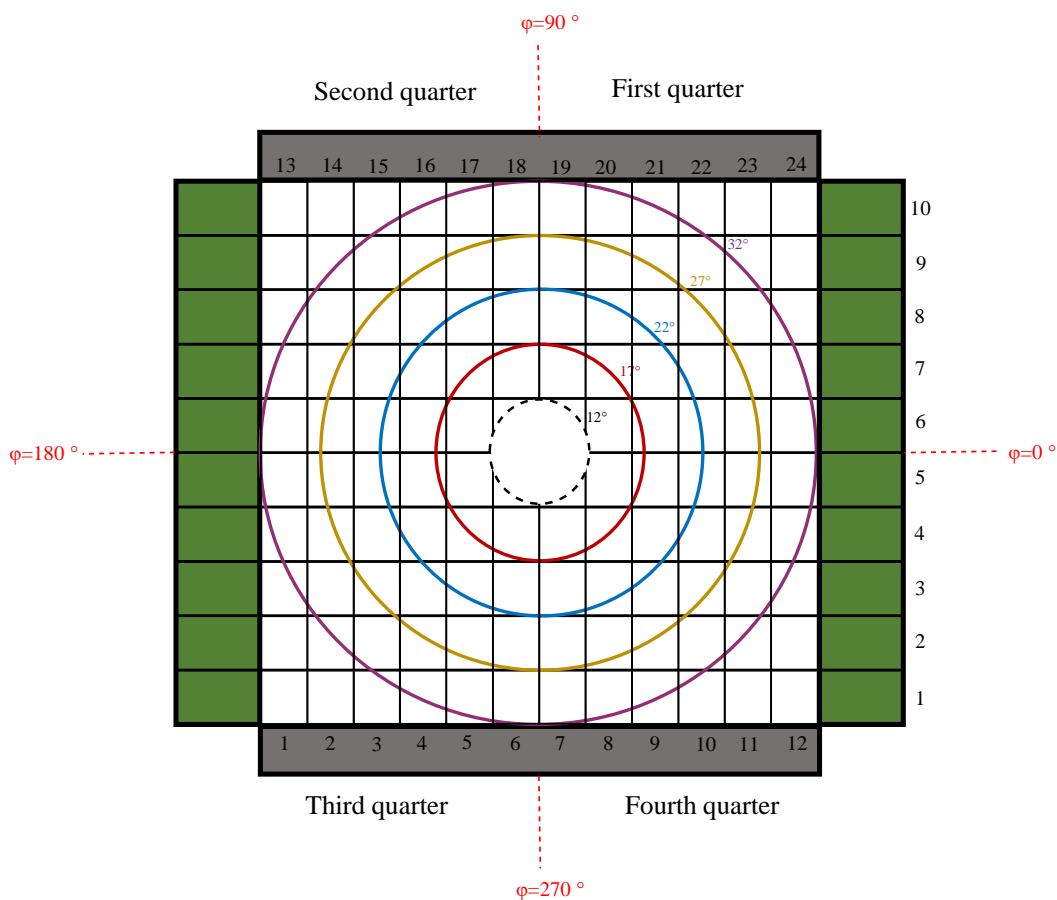

Fig. 3.3: Projection of 24 vertical ΔE strips and 10 horizontal E bars arranged perpendicularly with the polar angles (θ) of the registered particle represented by circles. A dashed-line circle is correlated with the beam pipe placed in the center of the detection system. The numbering and the different sections of the detector visible in the schematic picture will be used in the next part of this work.

---

[1]Due to the certain freedom of relative setting of the Wall-Ball system, the exact range of angular acceptance can vary between the different experimental runs.

Multi-Wire Proportional Chamber (MWPC):

After successful installing the BINA detector at CCB, the MWPC chamber channels were carefully checked, and its operation was improved compared to the last experiments at KVI. The MWPC detector [72] reconstructs the exact information about the emission angle of the outgoing charged particles. It is located about 30 cm from the target position (in the direction of the beamline). To resolve reconstruction ambiguities for multi-hit events, the MWPC consists of three anode wire planes with wires placed vertically (X), horizontally (Y), and diagonally (U), which is schematically shown in Fig. 3.4. Both the X and Y planes contain 236 wires, while the U plane consists of 296 wires mounted at $45°$. Anode wires are spaced every 2 mm, sandwiched between two cathode frames, and coupled to one electronic channel in pairs. The planes cover an area of 38 cm^2 (excluding the central hole for the beamline of 97.2 mm in diameter), and they are spaced 12 mm apart from each other, see Fig. 3.4 and Table 3.1. Because of the beamline, the wires passing through the chamber's center must have been divided into two parts treated independently in the acquisition system.
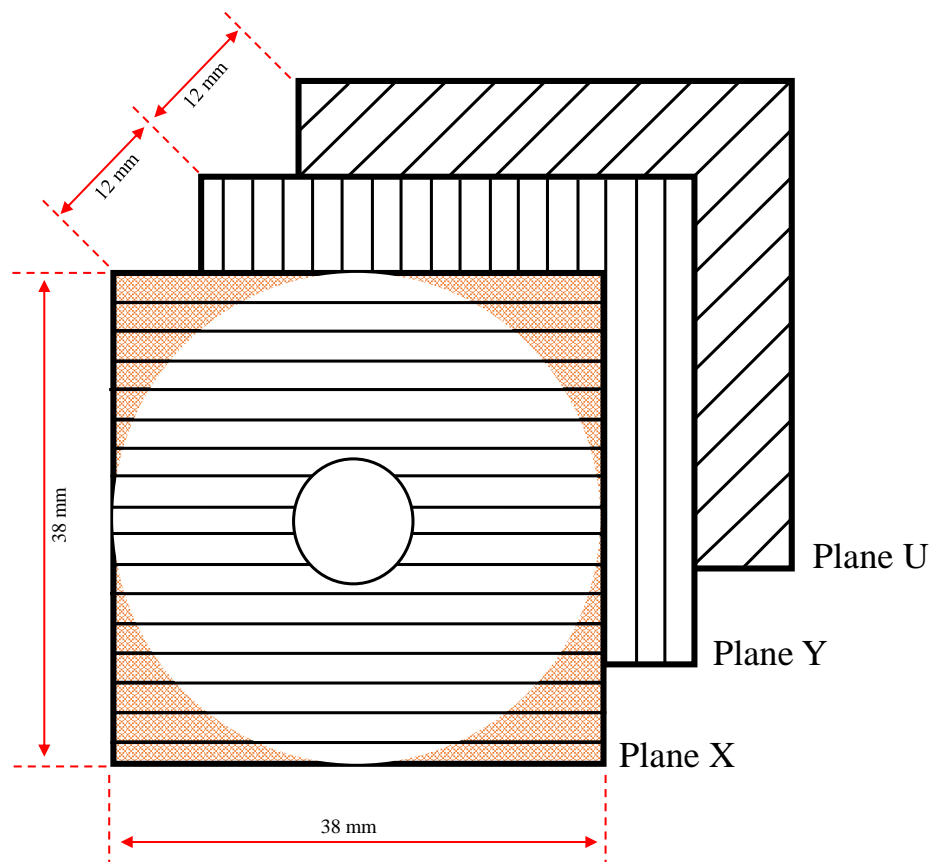
Fig. 3.4: Schematic picture showing three planes of MWPC - plane X (vertical wires), plane Y (horizontal wires), and plane U (diagonal wires); the orange parts visible in the X plane symbolize the corners.

The chamber is filled with an electro-negative gas mixture (80% of CF4 and 20% of isobutane) which is an active volume of the detector and provides excellent drift to the electrons. Each plane was powered separately with a high voltage of about 3000 V.

The details of track reconstruction are discussed in Sec. 4.1.2.

$\Delta E - E$ **hodoscopes**:

Two layers of scintillators form the $\Delta E - E$ hodoscope, schematically shown in Fig. 3.3. The first layer consists of 24 vertically-placed thin transmission-ΔE strips. Half of those cover the upper part of the detector, and the second half the lower part. The four central scintillators of the ΔE detector were trimmed in such a way as to leave space for the beam pipe passing through the middle of the detection setup. The light from ΔE strips were read out only from one side by photomultipliers connected via a prismatic lightguides. The dimensions of the ΔE and their lightguides were optimized with the 90-Sr radiation source. A charged particle passing through the ΔE detector loses part of energy, while the rest of it is deposited in the E detector.

The E detector is composed of ten horizontally-placed thick stopping-E bars. Their thickness was adjusted in such a way to allow us to stop protons with an energy up to 140 MeV. The cross section of each E detector has a trapezoidal shape and forms a part of a cylinder whose center coincides with the geometrical center of the target. The cylindrical shape of the E elements (forming an arch) reduces the contribution of so-called "cross-over" events - particles producing a detectable signal simultaneously in two adjacent bars. Two photomultiplier tubes registered the signal on both ends of the E detector bar. Only two central scintillators were cut in half and are shorter to make possible passage of the beam pipe.

The ΔE and E detectors bars are made of BICRON BC-408 plastic scintillator. Two layers of scintillators are placed perpendicularly to each other, forming a two-dimensional array for particle identification and setting the trigger conditions as described in Sec. 4.1.3. Basic parameters of construction and dimension of Wall detector are given in Table 3.1. The schematic view of $\Delta E - E$ hodoscope is presented in Fig. 3.3.

Construction details of BINA					
	orientation of scintillator	thickness	width	length	material
Δ E hodoscope	vertical	1 mm	31.66 mm	434 mm	BC-408
E hodoscope	horizontal	120 mm	90-100 mm	2200 mm	BC-408
MWPC	380 x 380 mm^2 central hole (diameter 97.2 mm) 3 active planes: X, Y, U				

Table 3.1: Construction details of the forward part of the BINA detector.

3.2.2 Backward Ball

The second part of BINA, Ball (see Fig. 3.5), is built of 149 detectors (polyhedrons of triangular cross-section) made of two kinds of scintillating polymers with different light emission times. Those polymers are brought into contact, resulting in a phoswich structure that allows for applying the identification method based on the $\Delta E - E$ technique using a common photomultiplier. The BINA Ball covers the angles $40° - 160°$. Ball and Wall together lead to the almost 4π acceptance (except for the position of the target system and beamline). The Ball also forms a scattering vacuum chamber where the target system is located. The BINA Ball is characterized by a worse (compared to BINA Wall) angular resolution defined by its granularity. Unfortunately, the Ball did not work correctly; only part of the Ball detectors was functioning.
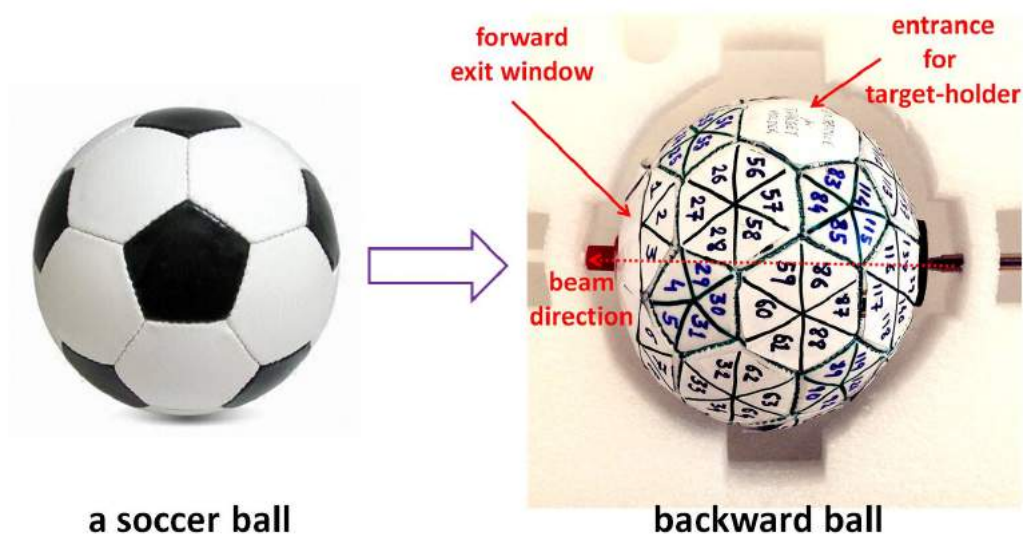
Fig. 3.5: The model of the backward Ball (in analogy to the soccer ball) where the hexagons and pentagons structure is visible. The target-holder entrance, forward exit window, and beam pipe are shown in the picture. The figure is adopted from [71].

3.3 Target system

The backward part of the detector is also a vacuum chamber where the target system is located. During the experiment, we used different kinds of targets. The first one, an aluminum target (Al) with a thin zink sulfide (ZnS) layer, was prepared to optimize the beam position and was used during the calibration runs for several beam energies (see Sec. 4.4). The second, the most important target was the liquid deuterium target (LD_2) which was the basis for studying the reactions of interest. The target system is equipped with temperature and pressure sensors, cryogenic, vacuum, and gas flow systems (see Fig. 3.6). After the installation of BINA at CCB, a new control system for the liquid target

was introduced. It is based on modules in the PXI (PCI eXtensions for Instrumentation) standard of National Instruments. With the use of the LabVIEW program [73], we can manipulate the valves and hence processes responsible for the proper system operation. More details about the liquid target can be found in Ref. [74].

In the first step, the air was removed during several flushing cycles using deuterium gas to prevent it from freezing in the further process of cooling. Using a compressor, we carry out the cooling process of the deuterium gas to obtain the liquid deuterium target. This process requires the maintenance of the proper value of temperature T $\approx$ 18K, vacuum in the scattering chamber of $p_1 \approx 10^{-5}$ mbar, and deuteron gas pressure $p_2 \approx 256$ mbar. Having all the parameters under control, we can start the filling process. The target cell was made of pure aluminum and a chambers' window of 4.5 μm Aramid foil. After filling, due to the bulging of the cell under pressure, the targets' thickness can change about $\pm$ 0.6 mm. Consequently, we can not precisely measure the targets' thickness and directly determine the luminosity (more details in Sec. 4.9). The target was installed vertically on the holder, which could be moved remotely by a pneumatic system attached to the upper part of the backward Ball. The mechanism allows quickly switching between all types of targets to place the selected target on the beam axis. The target system is presented in Fig. 3.7.

3.4 Electronics

The BINA electronic system was designed to detect two kinds of processes: the elastic scattering registered as a single charged particle and the breakup reaction - coincidences of two protons. The rate of registered events is different because of various values of the cross section for the elastic and breakup reactions. With the help of the Trigger Box (TB), we applied the individual prescaling factor to obtain representative and similar samples of each event type. The electronic readout is divided into a few components collecting information from MWPC, each ΔE, both sides of the E bars, and Ball detectors. The following subsections discuss the electronic readout with the data acquisition system and the triggers condition.

3.4.1 Electronic readout and data acquisition

The electronic readout structures reflected functional elements of the detector, consisting of parts dedicated to readout of Ball, MWPC, ΔE, and E detectors, see Fig. 3.8. The analog signals from scintillator detectors (Ball, ΔE, E) are splitted into two branches in the splitter. The first branch is routed to the constant-fraction discriminator (CFD). The CFD module generates the output logic
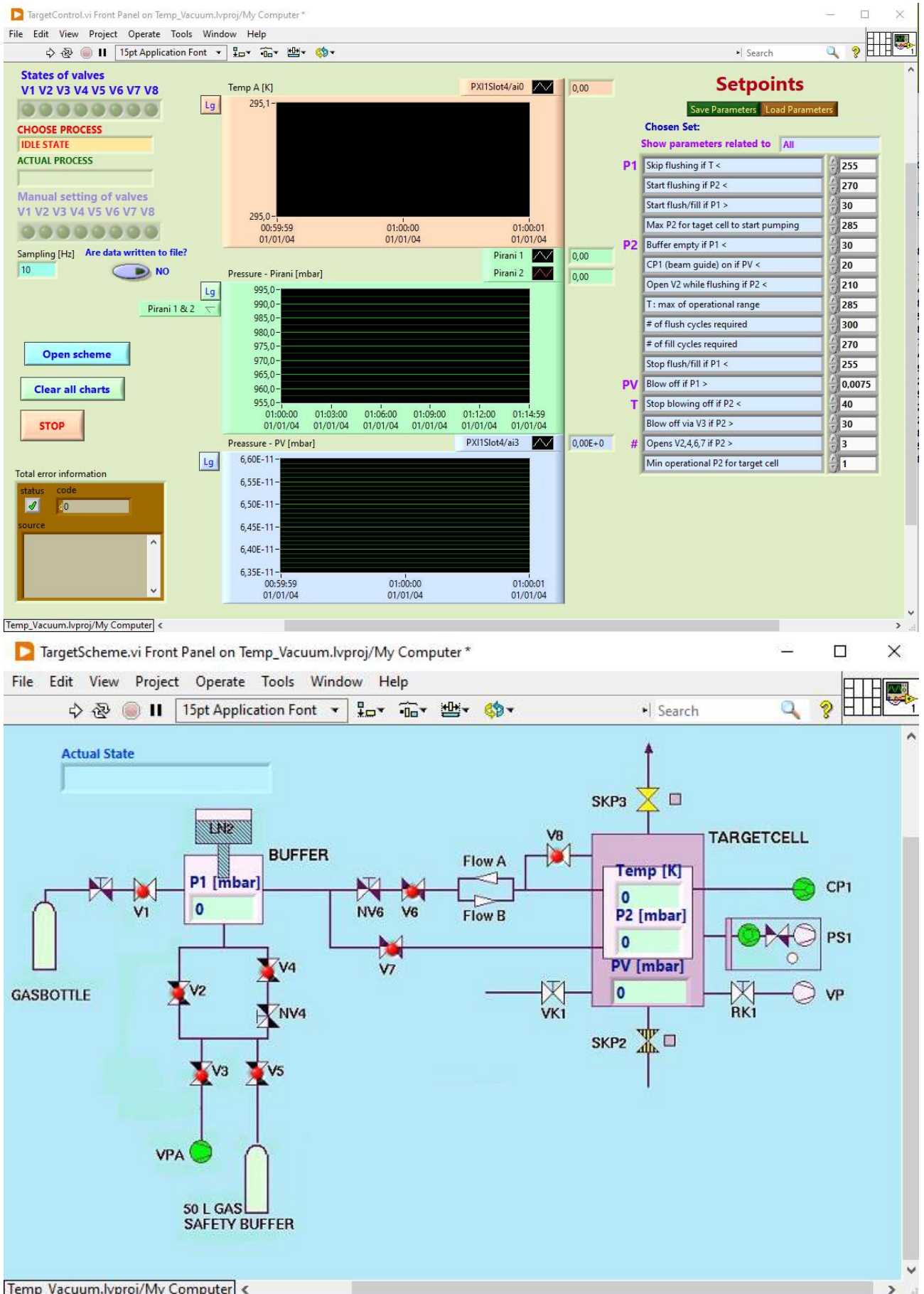
Fig. 3.6: *Upper panel*: The graphic shows the target system's most critical parameters controlled using the LabVIEW program [73]. *Lower panel*: The scheme of the target control system presented in the LabVIEW with the status (open/close) of all the valves.
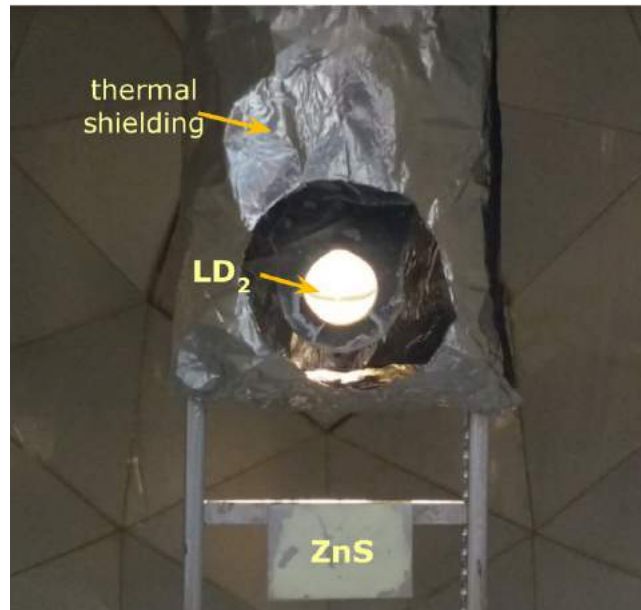
Fig. 3.7: The picture of the liquid deuterium target half-filled placed inside the backward Ball, which is also a vacuum chamber.

signal when the signal amplitude is higher than the defined threshold. Moreover, depending on the number of output channels fired, the CFD generates global OR and Multiplicity (MULT) signals. The global signal from CFD is are sent to the trigger logic (see Sec. 3.4.2), and individual outputs are fed to scalers, where they are counted and sent to the RIO III module, exercising control of the data acquisition system. Moreover, the CFD module also served to obtain the signals after time-walk correction for precise time information for a time-to-digital converter (TDC).

The second branch of signals from the splitter went to the analog-to-digital converter (ADC) with a 250 ns delay. The conversion was realized using the ADC module LeCroy 4300B within the time gate created in the trigger logic.

A separate PCOS-III system (Proportional Chamber Operation System from LeCroy) was dedicated to readout of the MWPC signals. This system consisted of amplifying-discriminating cards placed directly on the chamber and 32-channel modules registering signals from wires during the time gate associated with the trigger. These modules, equipped with the zero-suppression function, allowed for the clustering of signals from 2 or more adjacent wires, keeping the amount of readable information to an absolute minimum. Working in clustering mode also improved the resolution of the MWPC detector; for a given hit, the values coming from its centroid were transferred (half-wire bit).

Finally, all information from ADC, TDC, and PCOS-III modules was transferred, via the FERA bus, to the LeCroy 1190 buffer memory modules located in the VME crate, which were read out alternately. When the external counting system of the transmitted data had given the signal about almost a complete fulfillment, the switching and reading of memory occurred.
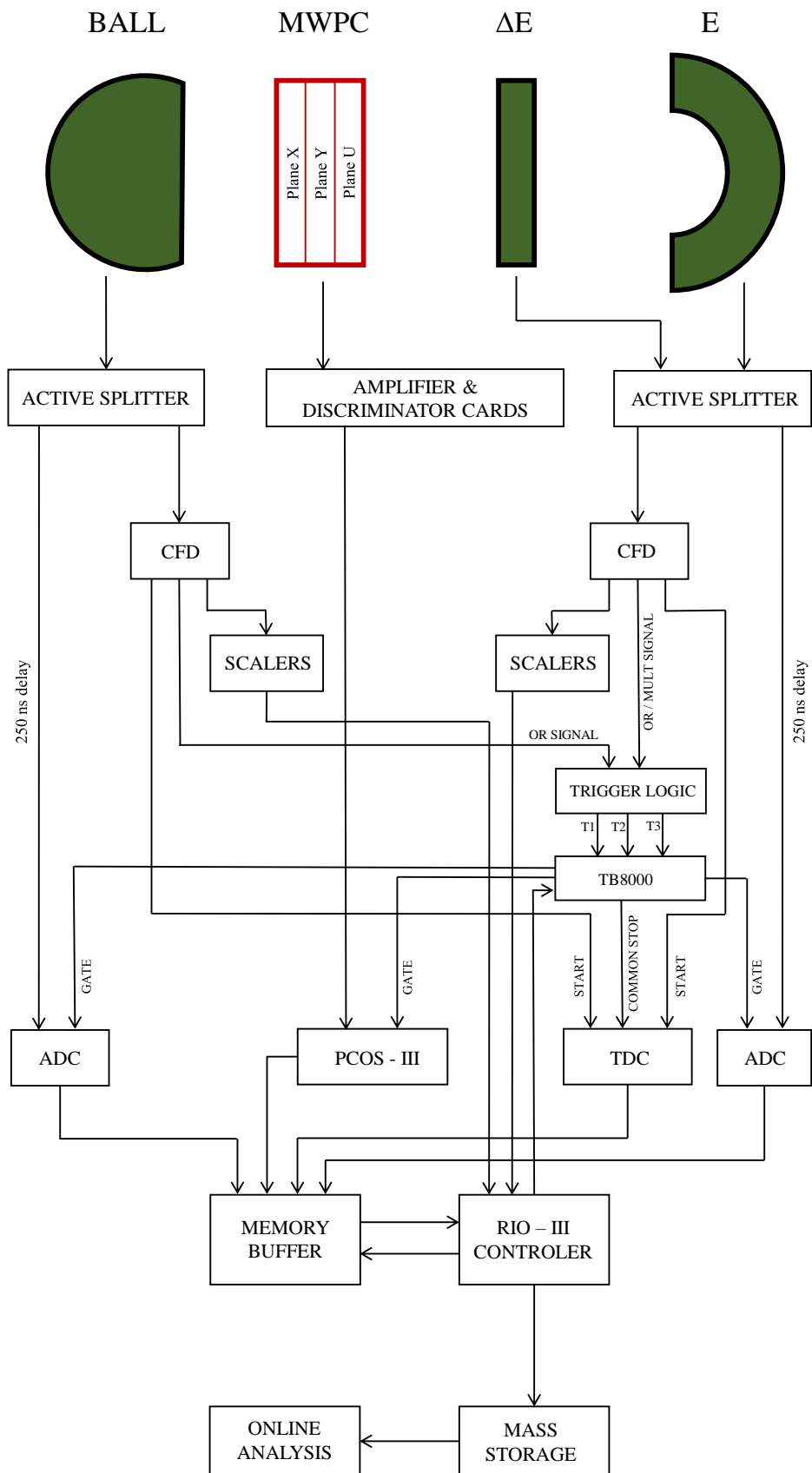
Fig. 3.8: The simplified flowchart of the electronic readout used for the BINA experimental setup.

3.4.2 Trigger conditions

If we had 100% efficient detectors and the angular acceptance would be 4π, and there was no energy threshold, we would be able to measure the coincidence of two charged particles consistently. It could be two protons coming from the breakup reaction or proton - deuteron from the elastic scattering. Unfortunately, the backward part of our detector system did not work correctly, such that, in reality, our setup did not cover all phase space, and very often, we detected only one particle. The trigger logic must correctly recognize these situations and identify the essential event - single and multi hits. According to the pd elastic scattering kinematic relation, while the proton is registered in the forward part of the detector, its coincidental deuteron is scattered to the backward, and vice versa. Because the Ball detector only partially worked, the protons and deuterons from the elastic process registered as a single event are the most frequent. Breakup events were also very often registered as a single proton in Wall. Hence, these events should be downscaled to avoid overloading the data acquisition system and keep the proportional rate to other events. The scaling process was carried out in the Trigger Box, whose output signal was used to construct a time gate on the ADC modules (only the signal in the gate is integrated) and PCOS modules (see Sec. 3.4.1). Trigger Box also served as a *common stop* signal for TDC modules. The definition of the trigger logic was based on the two possible outputs from the discriminator - multiplicity (MULT) and single hit (OR). The OR signal appeared for any charged particle signal input. Creating a MULT output required setting an additional threshold on the discriminator to choose the multiplicity of the signal; in our case, MULT of 2 was chosen. Triggers were built based on: signals from ΔE detectors, left PMT's of E detector (E_L), right PMT's of E detector (E_R), and Ball detectors. Because the central detectors $n_E = 5$ and $n_E = 6$ are cut in the middle, the multiplicity signal was required only on one side: right or left. Due to the above considerations, three different trigger conditions have been implemented. The logic condition of the triggers is presented in Table 3.2. Trigger T1 is a minimum bias trigger, with at least one charged particle in the whole detection setup (single particle). The T2 trigger is based on the multiplicity hits, and it is a coincidence of two particles registered in the Wall detector (Wall-Wall coincidence). The last one, the T3 trigger, requires at least one particle registered in Wall and at least one particle registered in the Ball detector (Wall-Ball coincidence). This class of events is not used in the analysis presented here.

Symbol	Logic notation	Downscaling factor
T1	(OR E_L) OR (OR E_R) OR (OR ΔE) OR (OR $Ball$)	2^4
T2	(MULT $E_L \geq 2$) OR (MULT $E_R \geq 2$)	2^0
T3	((OR E_L) OR (OR E_R) OR (OR ΔE)) AND (OR $Ball$)	2^0

Table 3.2: The logic condition of the triggers. More details in the text.

Chapter 4

Data Analysis

This chapter presents a detailed description of the procedures taken to determine the differential cross-section for the *pd* breakup reaction at the beam energy of 108 MeV. The data analyzed in this thesis involve six files (about 6 GB), sorted by the dedicated program FBRun based on the C++ programming language and utilizing the ROOT packages [75]. The fundamental classes of FBRun serve to sort raw data, interpret the basic electronic information and convert it into physical quantities. FBRun stores the data in the root trees for further analysis. Additionally, the software enables a selection of single and coincidence events registered with a dedicated trigger. There are FBRun classes dedicated to detector efficiency and energy calibration. The most important steps and methods of the data analysis are discussed in the following sections.

4.1 Event selection

The event selection was performed in several steps: setting the time cuts (TDC signals), the track reconstruction, the particle identification, and the selection of the reaction channel of interest. All these steps are described in the subsections below.

4.1.1 Time information

The first step of pre-sorting raw data is to reject events accidentally coincident with the trigger. This procedure is based on the TDC spectra from E and ΔE scintillators. They consist of several equidistant peaks, which reproduce the beam pulse repetition interval. The time gates for selection registered events with the corresponding triggers have been set on the highest peaks consisting of both - true

and accidental coincidences within the same beam pulse, which triggered the data readout. The other peaks are lower because they contain particles originating entirely from random coincidences with a trigger. Due to the low beam current of several pA, the contribution of random coincidences is very small. Setting a gate on TDC causes a reduction of the total number of events by 2%. The remaining accidental coincidence background is subtracted in the procedure described in Secs. 4.9.1 and 5.1.

4.1.2 Track reconstruction

The forward-scattered charged particles pass through the detector setup producing a signal in MWPC, ΔE, and E. The track reconstruction is based on the logic signals in the MWPC detector consisting of 3 wire planes - X, Y, and U (more detail in Chapter 3). When the signal is high enough (above the threshold), particles are accepted, registered, and marked as a "hit". A single particle gives the signal in one wire per plane, or we observe a cluster of two or more wires. We could precisely find the proper position if we had information about a signal amplitude. Due to its lack, we determine the hit position as the cluster's center. The analysis presented in this work use only so-called full tracks with all the three responding MWPC planes. Based on the signal from all planes, we can determine the intersection place of the charged particle. The first step of the track reconstruction procedure is to project the X and U planes onto a central Y plane (along the rays starting at the target's geometric center). The active wires form a right-angled triangle (see Fig. 4.1). The hits are treated as correlated (produced by the same particle) when the distance d between the XY intersection and the active wire U is less than 7 mm.

The next step of this procedure is to inscribe the circle into such a triangle. Knowing the center of the created circle and the distance between the target and the Y plane, assuming the reaction point in the target center, we can calculate the polar (θ) and azimuthal (φ) scattering angles in the laboratory frame given by the equation (4.1):

$$
\begin{aligned}
\theta &= \frac{180°}{\pi} \arctan\left(\frac{\sqrt{x^2 + y^2}}{z_0}\right), \\
\varphi &= \frac{180°}{\pi} \operatorname{atan2}\left(\frac{y}{x}\right),
\end{aligned}
\tag{4.1}
$$

where:

- x - horizontal position of the circle,
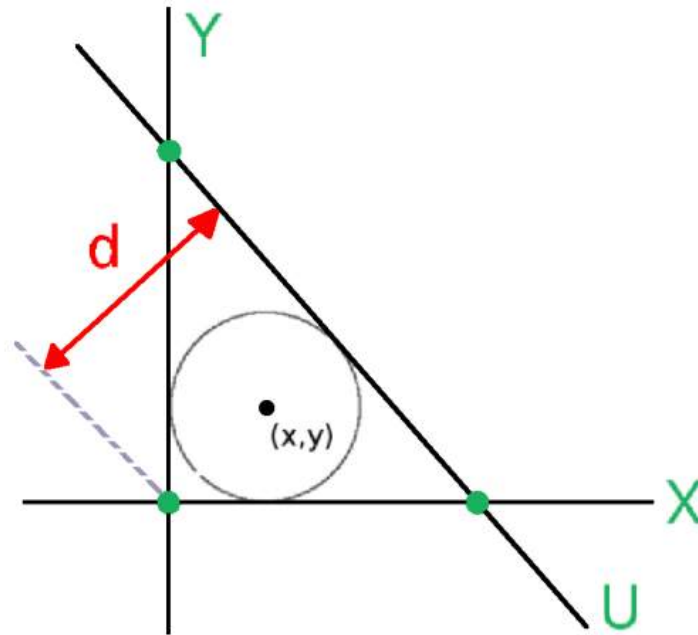
Fig. 4.1: A graphic represents three hit wires X, Y, and U, which are the basis of the particle's reconstruction procedure. The circle's center inscribed in the XYU triangle represents the reconstructed particle's track.

- y - vertical position of the circle,

- z_0 - distance between the target and the Y plane'

- atan2 - the function calculates the principal value of the arc tangent of $\frac{y}{x}$, using the two arguments' signs to determine the quadrant of the result; the return value is in the range $[-\pi, \pi]$.

The presented analysis focuses only on tracks with MWPC hits matched with ΔE and E hodoscopes signals, i.e., the calculated particle trajectory must intersect with the hit segments of the $\Delta E - E$ detectors with a specified margin. Besides, if some tracks were missing MWPC or ΔE hits but still had a signal in the E detector, they were used to calculate detector efficiencies.

4.1.3 Particle identification

Our analysis is focused on proton pairs coming from the breakup reaction. On the other hand, we need to select elastically scattered deuterons to normalize the breakup cross section. Therefore, the particle identification (PID) of both particle types is required, based on the $\Delta E - E$ technique.
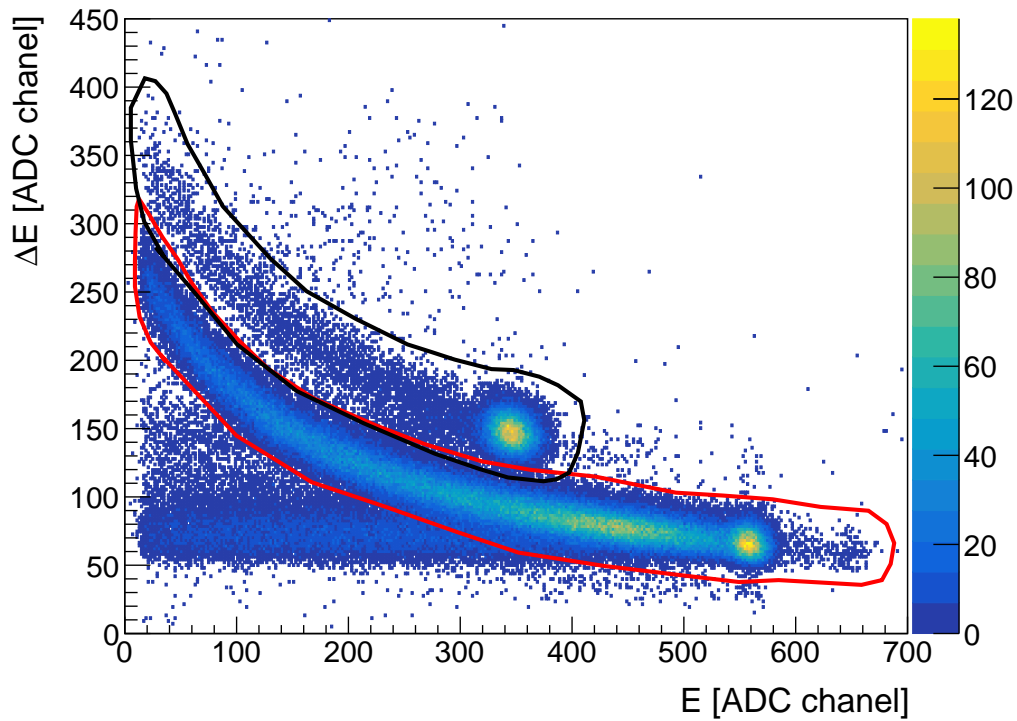
Fig. 4.2: Two-dimensional spectrum built for a chosen $\Delta E - E$ telescope ($\Delta E = 2$, $E = 0$); good separation of protons (lower band; red gate) and deuterons (upper spot, black gate) is visible.

This method is based on the different energy losses of protons and deuterons passing through the detector setup. Particles lose partial energy in the ΔE detector, while the remaining energy is deposited in the E scintillator. The $\Delta E - E$ hodoscopes were arranged perpendicularly, which allowed us to build two-dimensional spectra for an individual telescope corresponding to their overlap. The example of such a particle identification spectrum is presented in Fig. 4.2. We observe three groups of events: a long branch of protons coming from the breakup reaction (the red gate), the spot of elastically scattered protons located in the place of the highest energy deposited in the E detector (the red gate), and the spot of deuterons from the elastic scattering (the black gate). According to kinematic relation and detector gains, the spot's size, place, and energy depend on the selected telescope. Due to hadronic interactions, the deuteron spot is extended and forms a branch. As shown in the Fig. 4.2, proton and deuteron distributions can be well distinguished on a $\Delta E - E$ scatter plot. Thus, simple graphical cuts (red and black contours in Fig. 4.2) for different particle types are sufficient to separate them and implement a PID cut in further analysis. The gates are wide enough to avoid a significant loss of particles, and a slight overlap of them is allowed, see Fig. 4.2. In this way, we accept particles that may be of the correct type, and in the next steps of the analysis, we can make an additional cut or background subtraction.

# 4.2 Reconstruction of beam and setup geometry

Detector geometry links information between different detector elements and applies the experimental conditions in the data analysis routines. The data analysis allows us to control the accuracy of the geometry setting mainly in two ways:

1) by monitoring the number of reconstructed events when small variations of the detector positions are allowed; the parameters corresponding to maximal reconstruction efficiency are used;

2) by analysis of the edge events.

In the following subsection, we focus on the analysis related to the edge events, i.e., events that generate a signal in MWPC and simultaneously in two adjacent elements of the E detector. They are used to optimize the geometry settings of the E detector. We can observe the position of these events in the MWPC detector under the condition a selected pair of adjacent E detectors were hit. Analyzing the edge events of the chosen E detector, we expect to obtain on the MWPC plane one group of events correlated with the edge between the selected detector and the adjacent upper detector. Such events related to the edge between the 7th and 8th detectors located in the upper part of the detection system are shown in Fig. 4.3, *left panel*. Those two groups of events correlate with two different positions on the MWPC middle plane. After projecting events onto the Y-axis, see the *right panel* in Fig. 4.3, we can determine their exact Y-coordinates.

Fig. 4.3, the *right panel* shows two peaks. The first one, represented by the green line, located between the 60-70 mm in the Y plane, is split due to the discrete information from MWPC. Wires are spaced by 2 mm, coupled in pairs to one electronic channel, which increases their separation to 4 mm. The smearing of peaks is due to clusters. The second peak, illustrated as a red line at 80 mm, is much lower. We can find the origin of the lines in the X-Z plane by determining the signal Y-coordinates in MWPC and connecting these points with the corresponding edge of the E detectors. In the LibreCAD graphics program, the exact geometry of the detection system was mapped and shown in Fig. 4.4.

Due to the defined distances of the MWPC and E detector relative to the target position, we can draw the straight lines in the Y-Z plane through the two particles' registration points - at the MWPC and the edge of the E detector and check the origin of this line at the target position. The black lines connect the edges of the detector with the target's center. As a result of this procedure applied to all detector edges, we have two different intersections. The first one corresponds to the main peaks (green lines) and is located below the target's center. Since such a shift of the beam position is unrealistic, we conclude that MWPC and E detectors are not placed on the common axis. The E detector can be either shifted in Y or "tilted" or both. To obtain the exact E position, we need to draw the lines from
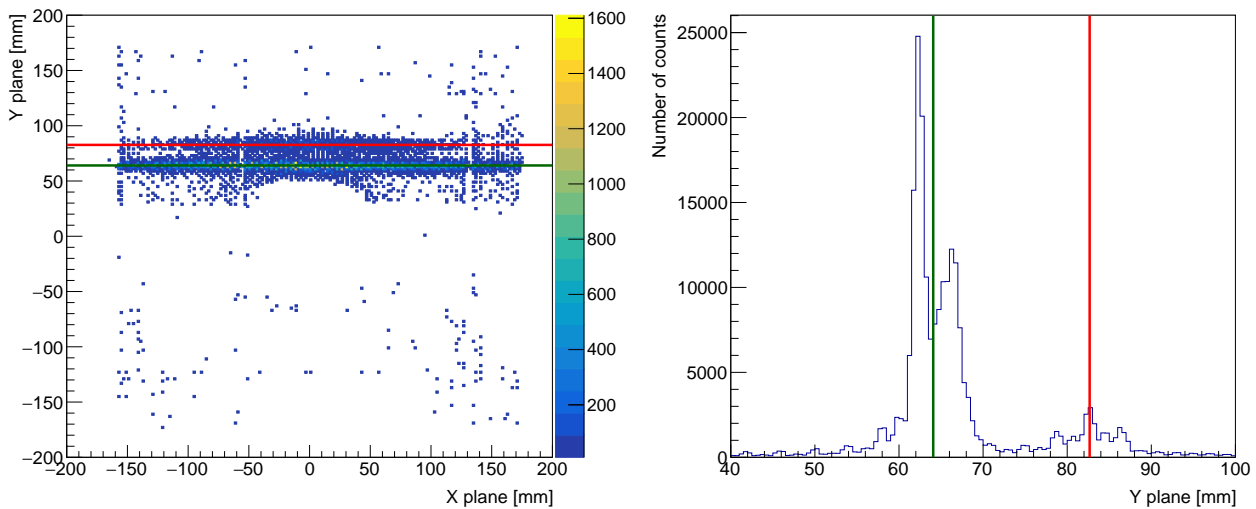
Fig. 4.3: *Left panel:* Events from the edge between the 7th and 8th detector located in the upper part of the detection system correlated with the position in the MWPC detector. The green and the red lines represent two different places on the MWPC middle plane, which correspond with the edge of the chosen E detector. *Right panel:* Projecting events presented in the left panel onto the Y-axis to determine the average Y-coordinates, presented as vertical color lines.

the target center passing through the previously designated Y-coordinate on MWPC. These lines show us where the edges of the E detector should be. The intersection of red lines, well above the target, is correlated with a different group of events appearing only in the upper part of the detection setup. Analysis of the energy of the protons indicates that they are coming directly from the beam degraded and scattered on the thick targets' frame or holder. The possible impact of this additional peak will be discussed in Secs. 4.9 and 5.1.

4.3 Simulation framework

All simulations applied in this work were written in C++ language, based on the Geant4 framework [76], using the Monte Carlo methods. The simulation code (user routines) was developed over the last few years. At first, it was prepared for the experiment with the SALAD detection setup, written in FORTRAN language, based on the Geant3 version. Later, it was adapted to the upgraded version of the SALAD detector - the BINA setup and rewritten to Geant4 [77, 78]. Geant4 is a toolkit that provides full support for detector simulation: geometry, particle tracking and detection, event management and visualization of these processes in a user-friendly interface.

The simulation reflects the BINA detector geometry according to the description in Chapter 3, with small exceptions. The target holder and the target cooling system, which is partially located in the
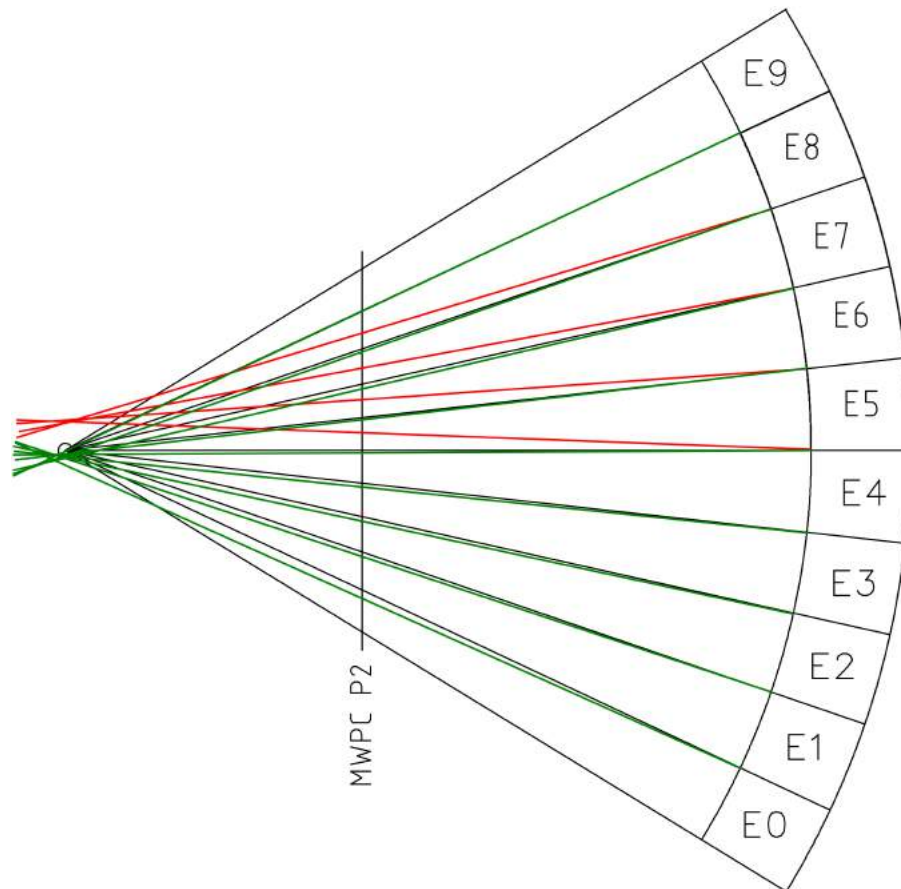
Fig. 4.4: The graphics presenting the geometry of the MWPC and E detectors and reconstruction of the edge events in the Y-Z plane when Z represents the beam direction with 0 at the nominal target center. The perpendicular black line labeled as MWPC P2 represents the MWPC middle plane. The lines start from each edge of the E detector and pass through the reconstructed position in the MWPC. The intersections correspond with two sources matching two peaks in the MWPC (see, Fig. 4.3, *right panel*).

upper part of the Ball detector, were not implemented in the simulation. Some details, such as Kevlar fibers supporting the foil covering the scattering window, are also not reproduced.

The multidisciplinary package Geant4 provides a broad set of physical methods to handle a variety of interactions between particles and matter over a wide energy range. The following physical processes were included in the simulation:

- multiple scattering,

- ionization,

- bremsstrahlung,

- e^+e^- pair production,

- Coulomb scattering,

- hadronic interactions.

The simulation was used to determine the energy calibration described in Sec. 4.4, the particle losses due to the hadronic interaction (Sec. 4.7), and the edge events (Sec. 4.8) or configurational efficiency described in Sec. 4.10.

4.4   Energy Calibration

The differential cross section of the pd breakup reaction can be presented as a function of proton energy or, equivalently, as a function of an arc length, S, along the kinematical curve (for the definition, see Sec. 2.1.2). Therefore, knowledge about accurate energy is necessary for further analysis. Charged particles passing through the detector lose their kinetic energy by excitation, and, in consequence, during the de-excitation process, light is produced, known as the fluorescence phenomenon. The amount of light produced is converted into an electronic signal and amplified in a photomultiplier. Due to the exact correlation between the emission angle and energy in the elastic scattering process, protons coming from this reaction are the best choice for the energy calibration procedure. However, the protons elastically scattered off the liquid deuterium target overlap with the protons coming from the breakup reaction. Therefore, the Al target was used in the special calibration runs to avoid difficulties separating the reaction channels and obtaining proton energies practically independent of the scattering angle.

Moreover, the Monte Carlo simulations were performed to determine energy losses in our detection setup. The experimental data measured on the Al target and data calculated in the simulation were the basis for the calibration method. This procedure aims to obtain a relation between the ADC signal and energy deposited in the E detector (in the first step) and transform deposited energy to initial particle energy (in the second step).

4.4.1   Transformation of pulse height to energy deposited in E detector

In order to perform an energy calibration, dedicated runs were carried out with proton beams at energies of *70-, 83-, 97-, 108-* and *120* MeV impinging on the aluminum target. The registered particles are sorted by the side *s* (*s = right / left*), the detector number *n* (*n = 1, 2, ..., 10*), and polar angle θ binned by 2 degrees. The signals c_1 and c_2 registered by photomultiplier tubes on both ends of each E detector are combined in the geometrical average ($C = \sqrt{c_1 \cdot c_2}$) in order to suppress the

effects of light attenuation along the bar. Due to the cut of the two central scintillators (for the beam pipe), in these cases, the geometrical average was replaced by a signal of one side ($C = c_1$ or $C = c_2$).

The spectra of protons scattered on the Al target, for a chosen set of energies, s, n, θ, are presented in Fig. 4.5, *left panel*. The corresponding results of the Monte Carlo simulation performed in Geant4 are shown in Fig. 4.5, *right panel*. The distribution of elastically scattered protons for the chosen detector, side and emission angle in experimental data and simulation was analyzed by fitting a Gaussian function. Using deposited energy obtained by the simulation, the relation between the C and the actual energy deposited by protons was obtained. An example of the calibration curves obtained for the chosen s, n, θ is presented in Fig. 4.6.

It shows the relation between measured energies of elastically scattered protons expressed in ADC channels (a horizontal axis) and values of relevant energies simulated using GEANT4 (a vertical axis). The calibration curve becomes linear above approximately 50 MeV (see Fig. 4.6, *left panel*). Below this value, the light quenching effect is expected due to the large stopping power [79, 80]. The calibration curve fitted to the entire range of signal C is described by the non-linear equation (4.2) (see, Fig. 4.6, *right panel*):

$$E_{dep}\left(s, n, \theta\right) = a\left(s, n, \theta\right) \cdot C + b\left(s, n, \theta\right) \cdot \sqrt{C}; \tag{4.2}$$

where:

- $E_{dep}\left(s, n, \theta\right)$ is simulated energy deposited in the E detector with parameters denoting the detector's side, number, and polar angle, respectively;

- $a\left(s, n, \theta\right)$ and $b\left(s, n, \theta\right)$ denote the fit parameters.

## 4.4.2 Transformation of deposited energy to initial energy

Knowing the relation between the C-signal and energy deposited in the E detector and having reconstructed particle trajectory, we are able to determine the particle's energy at the point of reaction. To achieve it, we carried out a series of simulations using the initial proton energies between 19-25 MeV with step 1 MeV and from 25 to 100 MeV with the step of 5 MeV for each polar θ angle. The spectra obtained from the simulation were analyzed, as before, by fitting the Gaussian functions, see Fig. 4.7, *left panel*. Finally, we obtained the initial ($E_{initial}$) versus deposited energy (E_{dep}) spectra for each angular bin, and then the 5th-degree polynomial was fitted. The function which transforms
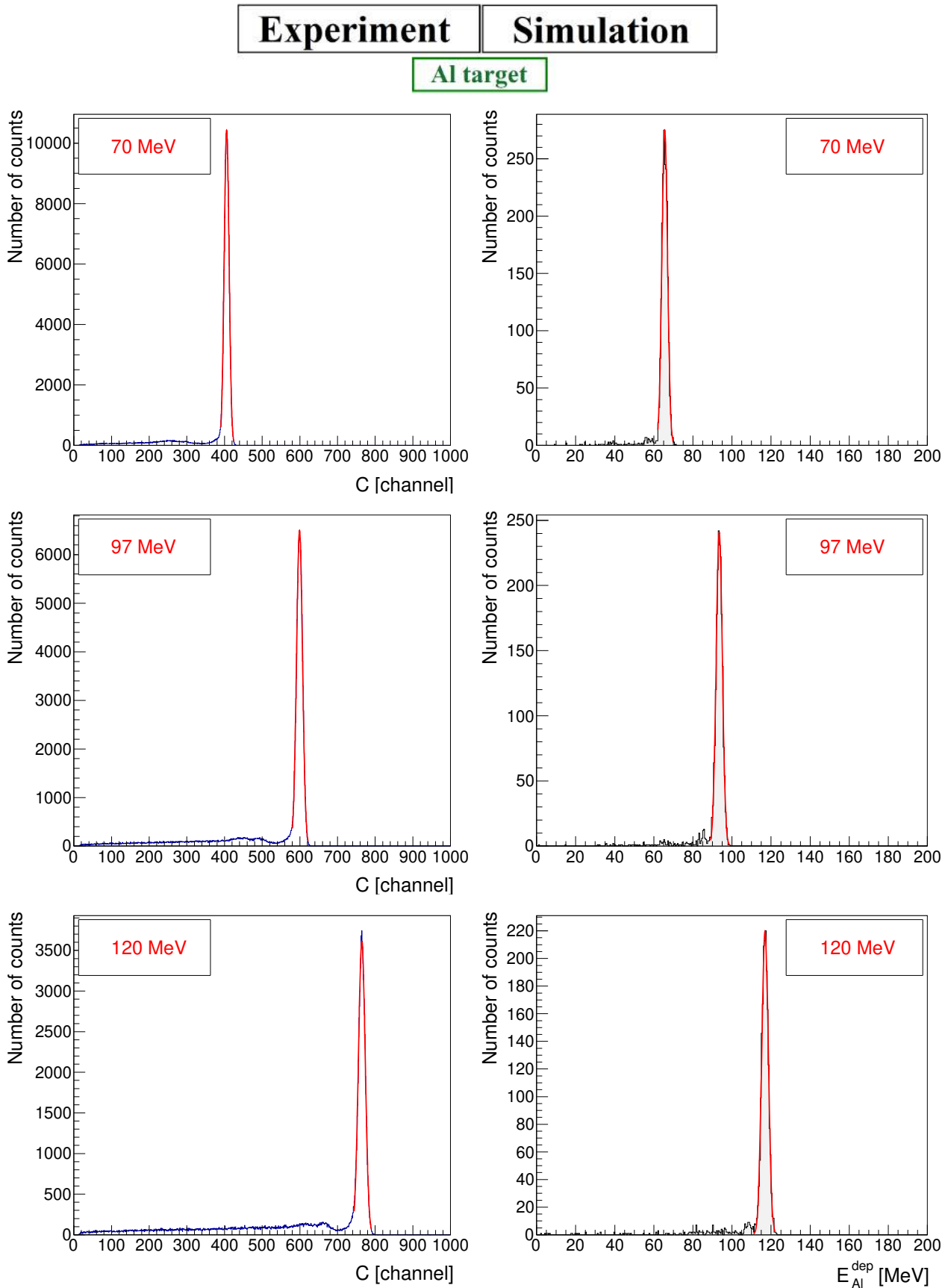
Fig. 4.5: Examples of experimental (*left panel*) and simulated (*right panel*) energy spectra of elastically scattered protons for the left side of the detection setup ($s = left$), detector number $n = 3$, and polar angle $\theta = 16°$ for three beam energies: 70 (top), 97 (middle) and 120 MeV (bottom panel). The peak positions are determined by fitting Gaussian functions (red curves).
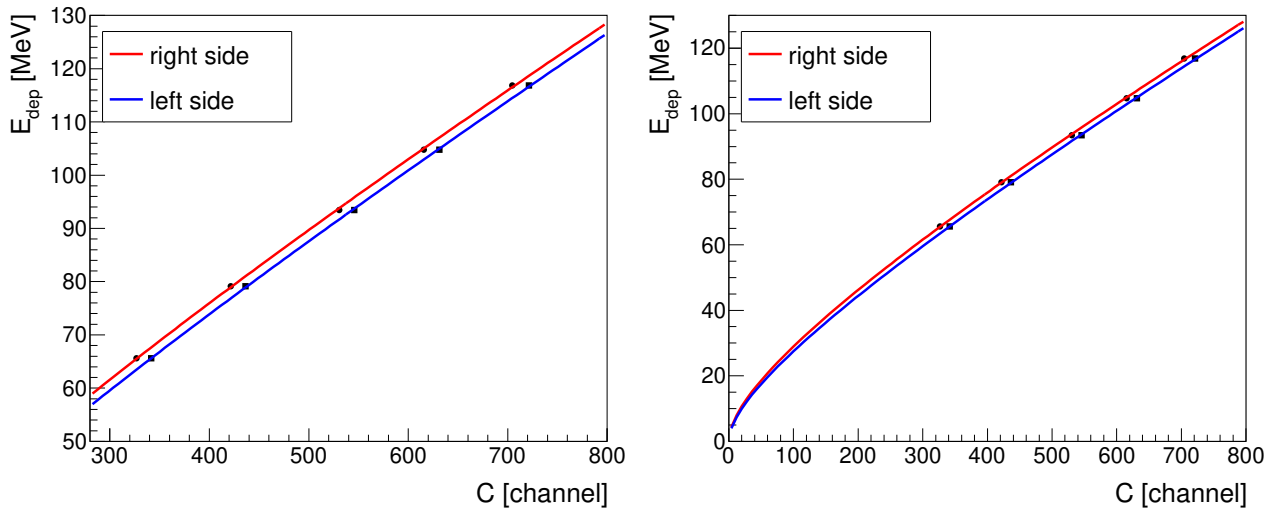
Fig. 4.6: The calibration curve obtained for protons scattered at a polar angle $\theta = 16°$ on the left (blue line) and the right (red line) side of the detector ($n = 3$). The *left panel* shows the linear character of the curve corresponding to the range above 50 MeV. Below this value, the non-linear function is assumed, visible in the *right panel*. Statistical uncertainties are smaller than the size of the points.
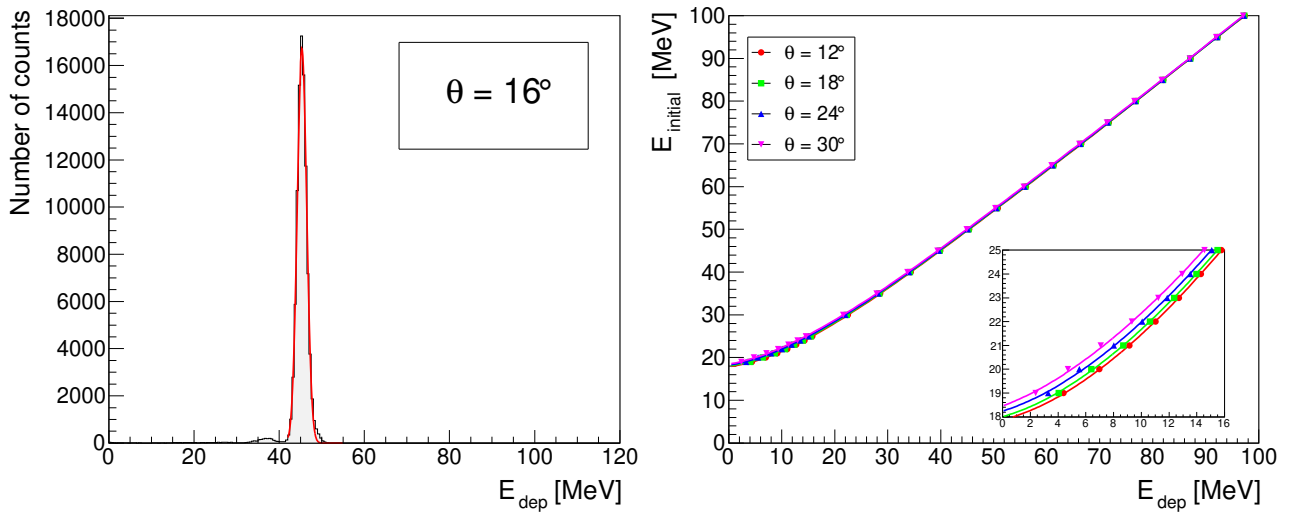
Fig. 4.7: *Left panel:* The simulated energy spectrum $N(E_{dep})$ obtained for the $E_{initial} = 50$ MeV and polar angle $\theta = 16°$ with the Gaussian fit. *Right panel:* The relation between the deposited versus initial energy obtained for chosen polar angles θ. The 5th-degree polynomial function was fitted to the points.

the deposited energy into the point reaction's energy for a set of angles is shown in Fig. 4.7, *right panel*.

After selecting the proton-proton coincidences and performing the energy calibration, any kinematical configuration of the breakup reaction (within the angular acceptance of the detection system) can be analyzed. Protons momenta determine the breakup reaction kinematics. The emission angles of these outgoing protons (polar angles θ_1, θ_2) and their relative azimuthal angle (φ_{12}) define the configuration.

Examples of the kinematical spectra for two selected angular configurations are shown in Fig. 4.8. As observed, the center of the experimental band lies on the theoretical kinematics represented by the black line, which confirms the correctness of the applied calibration method.
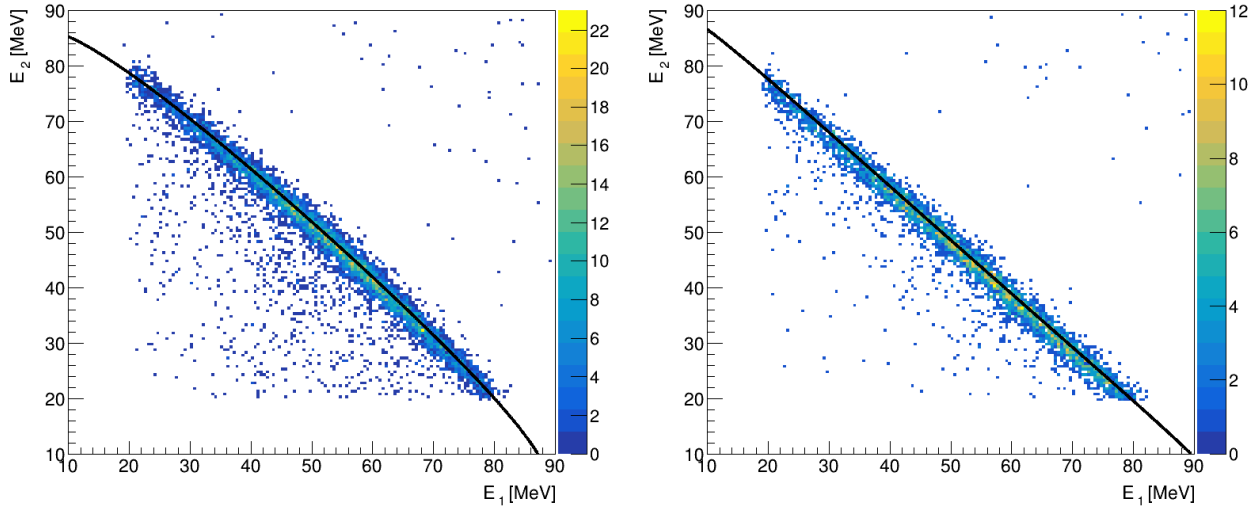

Fig. 4.8: Kinematical spectra (correlation of proton energies) obtained for breakup events collected at a beam energy of 108 MeV for two selected angular configurations $\theta_1 = 28°, \theta_2 = 30°, \phi_{12} = 180°$ (*left panel*), and $\theta_1 = 20°, \theta_2 = 24°, \phi_{12} = 160°$ (*right panel*). The relativistic kinematics represented by a black line is superimposed.

4.5   Correction of the unstable E detector

By analyzing the calibrated spectra, we observe a certain level of ADC - instability in detector number five ($n = 5$) for all analysed θ angles (see Fig. 4.9, *left bottom panel*). However, this detector was stable for some time intervals, as seen in Fig. 4.9, in the *left upper panel* on the left side of the red line. Firstly, we want to check if the data from the stable range are consistent with the data from neighboring scintillators ($n = 4$ and $n = 6$). Although properly calibrated during another period of stability, the detector might have changed its amplification level. This effect does not change the overall energy calibration coefficients, but the change have to be carefully taken into account before applying the standard calibration procedure. Thus, we created one-dimensional energy spectra from those detectors and compared them with each other. Even though the detector $n = 5$ was stable - working during the compared time period, the energy spectrum is still different to the adjacent detectors; thus, finding the difference in amplification between the calibration runs ($p + Al$) and the production runs ($p + d$) is also necessary.

The calibration correction was based on the autocorrelation method described in more detail in Ref. [81]. To recalibrate the detector ($n = 5$) within the stable regime, we rescale the raw ADC signal (C) by
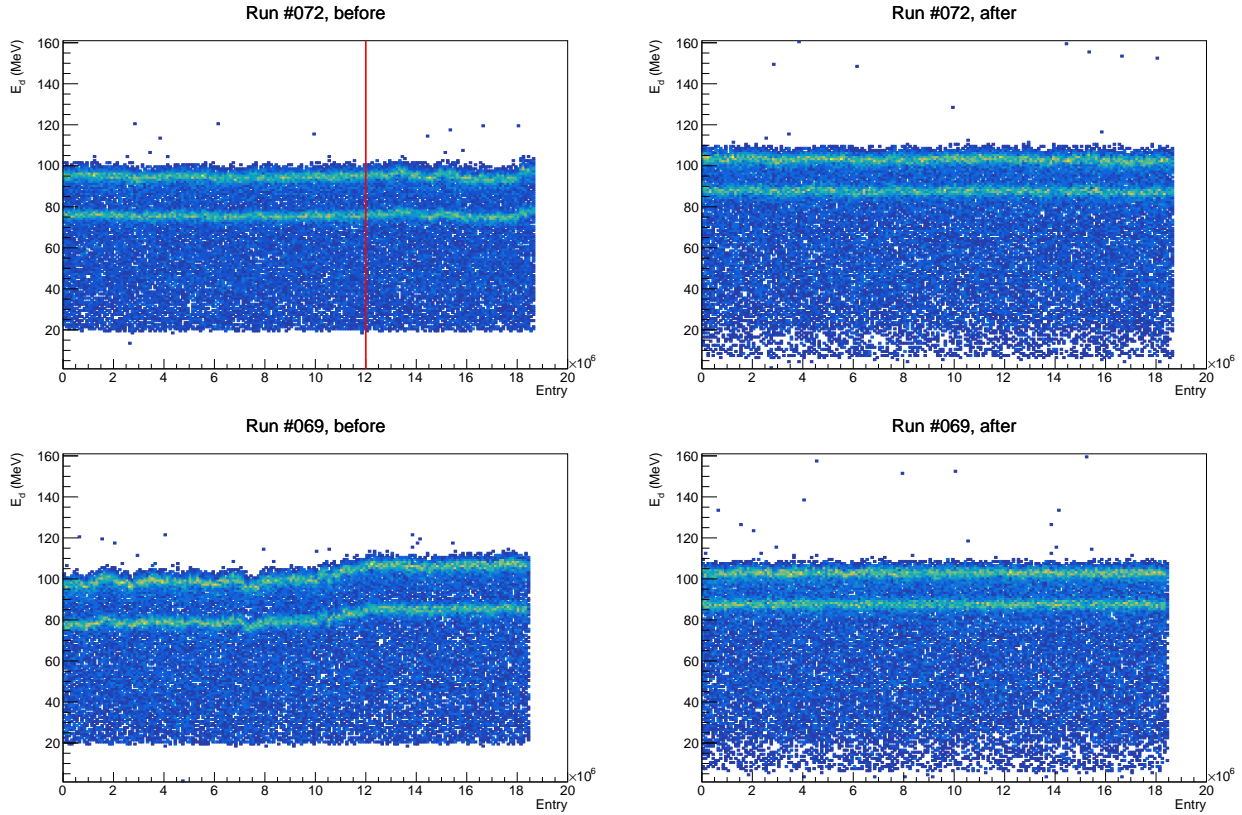
Fig. 4.9: *Left panel:* The initial data (before correction) observed in the $N = 5$ detector registered during the different runs (#069 and #072). The data in the top-left figure includes a stable regime of the detector operation visible on the left of the red line. *Right panel:* The corrected spectra obtained via autocorrelation method described in the main text.

a factor A and obtain a new energy spectrum $N(E_d(C'))$ (where $C' = AC$). Next, we calculate the correlation function between the energy spectrum of the detector $N(E_d(C'))$ with the referential spectrum of neighbor scintillator $N_{ref,1}(E_d(C))$, where C is binned in the same way in both histograms:

$$f_{cor,1} = \sum_C N_{ref,1}\left(E_d(C)\right) \cdot N(E_d(AC)). \tag{4.3}$$

Finally, we optimize over parameter A to maximize the correlation function. The best matching was found for a value A=1.116.

After that, we are ready to reconstruct the data from the unstable period of the detector operation. Now, the previously recalibrated area will serve as a reference spectrum. In a similar manner, we want to use the autocorrelation method to find the proper scaling of the ADC signal. However, due to the unstable character of the detector, we split the data into small slices (with a width of 10^5 events), within which the measurement points behave regularly. Then, we perform the regularization for each of them separately. As previously, we calculate the correlation function between the reference ADC

spectrum from a stable area $N_{ref,2}(C')$ and the projected ADC spectrum from the i-th slice $N(A_iC)$, i.e.,

$$f_{cor,2} = \sum_C N_{ref,2}(AC) \cdot N_i(A_iC))$$ (4.4)

where A_i is the scaling parameter that should maximize the function.

The corrected spectra obtained by coefficients A_i are presented in Fig. 4.9, *right panel*). Additionally, we independently solve the rescaling problem by the Kolmogorov-Smirnov method [82], which gives us the same results.

4.6 Forward detector efficiency

To determine the proper number of events of a specific type, we need to know the efficiency of the whole detection setup. The detection efficiency depends on many factors, such as non-functioning or noisy chamber wires or gaps between the scintillator stripes. Since each detector works independently, the total efficiency is defined as a product of the efficiency components:

$$\varepsilon_{WALL} = \varepsilon_{MWPC} \cdot \varepsilon_{\Delta E} \cdot \varepsilon_E,$$ (4.5)

where:

ε_{MWPC}, $\varepsilon_{\Delta E}$, ε_E are the efficiencies of the Multiwire Proportional Chamber, ΔE and E detectors, respectively.

The total efficiency is a scaling factor for the number of registered events for two reactions: elastic scattering and breakup. In the case of elastic scattering, a single particle is recorded in Wall. The efficiency depends on the polar angle (θ) because the rate is integrated over the azimuthal angle (φ). Therefore, 1-dimensional efficiency as a function of θ angle will be used for elastic scattering events. For the breakup reaction we have coincidences of two protons depending on θ_1, θ_2, and φ_1, φ_2, and the variables cannot be separated. Consequently, we require a 2-dimensional (θ, φ) efficiency map in case of breakup events.

4.6.1 MWPC efficiency

The MWPC consists of three planes of wires: X, Y, and U, as described more widely in Sec. 3.2.1. The total efficiency of the proportional chamber is determined by the multiplication of the efficiency

products of all its three planes:

$$\varepsilon_{MWPC}\left(\psi\right) = \varepsilon_x\left(\psi\right) \cdot \varepsilon_y\left(\psi\right) \cdot \varepsilon_u\left(\psi\right), \tag{4.6}$$

where ψ is a relevant set of kinematic variables:

- $\psi \equiv \theta$ for elastic scattering process,

- $\psi \equiv (\theta, \varphi)$ for the breakup reaction.

To construct the map of MWPC efficiency, only events marked as a single particle registered in the $\Delta E - E$ hodoscope were taken into account. The efficiency of the given plane can be calculated as the ratio of the number of registered events with hits in all three planes to the number of events with at least the other two planes hit in a selected angular segment of (θ) and azimuthal angle (φ). For example, the efficiency of X plane is given by the following relation:

$$\varepsilon_x\left(\psi\right) = \frac{N_{xyu}\left(\psi\right)}{N_{yu}\left(\psi\right)} \tag{4.7}$$

where:

- $N_{xyu}\left(\psi\right)$ is a number of counts registered in the selected angular segment (ψ), satisfying the condition of one hit (or cluster) per the X, Y, and U planes;

- $N_{yu}\left(\psi\right)$ is a number of counts registered in the same angular segment with at least one hit (or cluster) per the Y and U planes.

The efficiency of the two other planes is calculated using a similar method.

We use elastically scattered deuterons for determining the integrated luminosity (see Sec. 4.9.2). We decided to correct these events with the one-dimensional efficiency based on particles assigned as deuterons because of the significant impact of PID on the results (see, Fig. 4.10, *left panel*). Since we analyze deuterons in each quarter of Wall individually (Sec. 4.9), the one-dimensional efficiency of the MWPC chamber was also determined for each quarter separately, presented in Fig. 4.10, *right panel*.

In contrast, the two-dimensional map of the efficiency used for the breakup reaction is determined for the single particles regardless it is a proton or a deuteron (without PID), although protons are
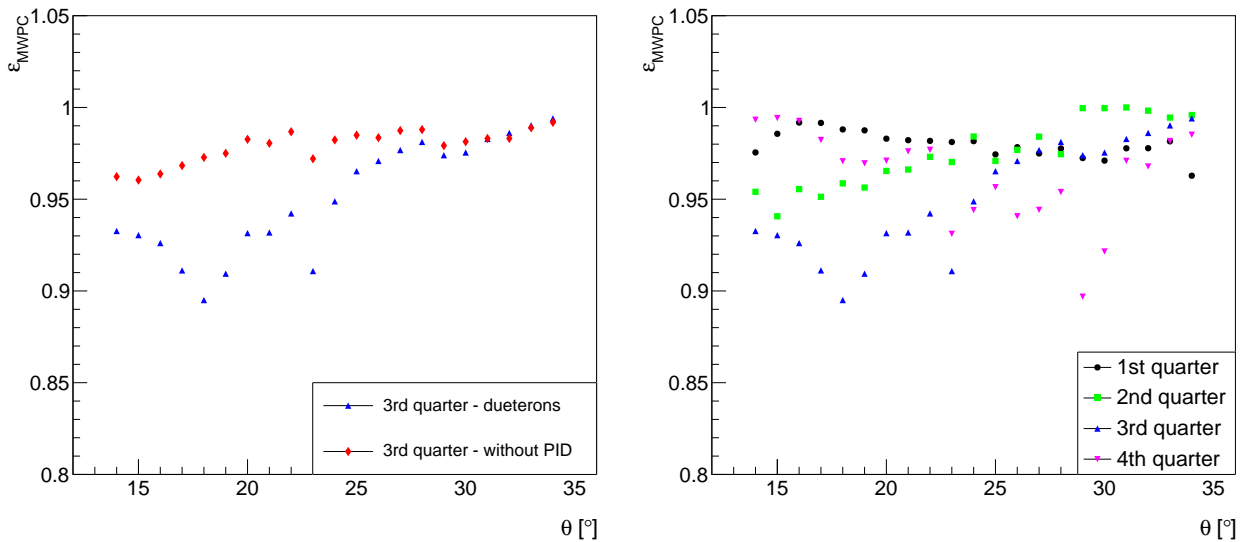
Fig. 4.10: *Left panel:* One-dimensional MWPC efficiency obtained for the particles identified as a deuteron (blue symbols) and for all single tracks (red symbols) in a chosen quarter. *Right panel:* The one-dimensional MWPC efficiency for registering deuteron determined for each quarter separately, presented in the θ angle function.

statistically dominating. The efficiency for the individual planes and the total MWPC efficiency are shown in Fig. 4.11. The one-dimensional efficiency (see Fig. 4.10, *right panel*) fluctuates between 0.89% and 0.98%, depending on the quarter. The major part of the two-dimensional map for all planes (Fig. 4.11) has an efficiency of 0.98% or above. There are also areas of slightly lower efficiency in the X plane (for polar angle $\theta < 18°$ correlated with an azimuthal angle $\varphi > |120°|$); locally, the efficiency is strongly reduced in the regions corresponding to not working channels. The blank areas above the polar angle $30°$ are due to the geometrical limits of the MWPC chamber.

As shown in Fig. 4.10, *left panel*, the MWPC efficiency depends on the particle type. Moreover, two-dimensional maps (Fig. 4.11) indicate that the efficiency also depends on the particle's energy. In our analysis, we treated the detector efficiency as an averaged value over the particles' energy. We also neglected possible efficiency fluctuations over time, different particle types, or energy ranges. The question arises whether we should not analyze the detector efficiency depending on the particle's energy, especially its stopping power in the MWPC. Such an estimation was made in a paper [23], where the impact of stopping power on the MWPC efficiency was shown. Since the MWPC efficiency in our experiment was high, the simplified approach was used, yet the more elaborated one will be considered in the future.
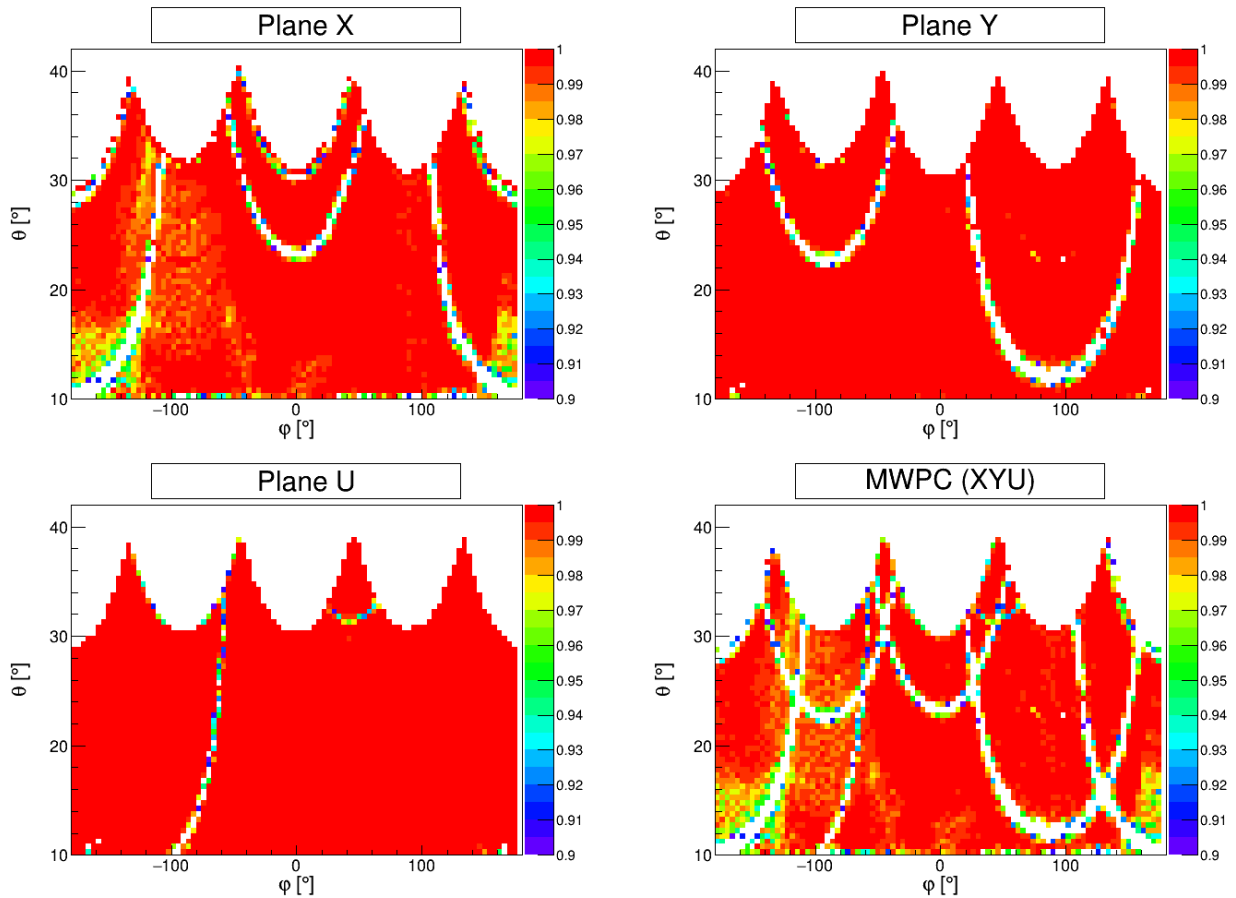
Fig. 4.11: The 2-dimensional efficiency maps determined for a single particle for all three planes and total MWPC efficiency.

4.6.2 ΔE **efficiency**

The ΔE efficiency was calculated similarly to the one described in the subsection above. It was determined by counting the ratio of the number of particles reconstructed based on signals from MWPC, ΔE, and E ($N_{\Delta E}$) to those registered regardless of the appearance of information from ΔE (N_{ALL}):

$$\varepsilon_{\Delta E}\left(\psi\right) = \frac{N_{\Delta E}\left(\psi\right)}{N_{ALL}\left(\psi\right)} \tag{4.8}$$

where: ψ has the same meaning as in Eq. (4.6).

Analogically, only events marked as a single particle were taken into account. The ΔE efficiency map is presented in Fig. 4.12, as 1-dimensional efficiency (*left panel*) and a 2-dimensional (*right panel*). It is clearly visible that the ΔE detector has an excellent efficiency, over 99%, and the local decrease of
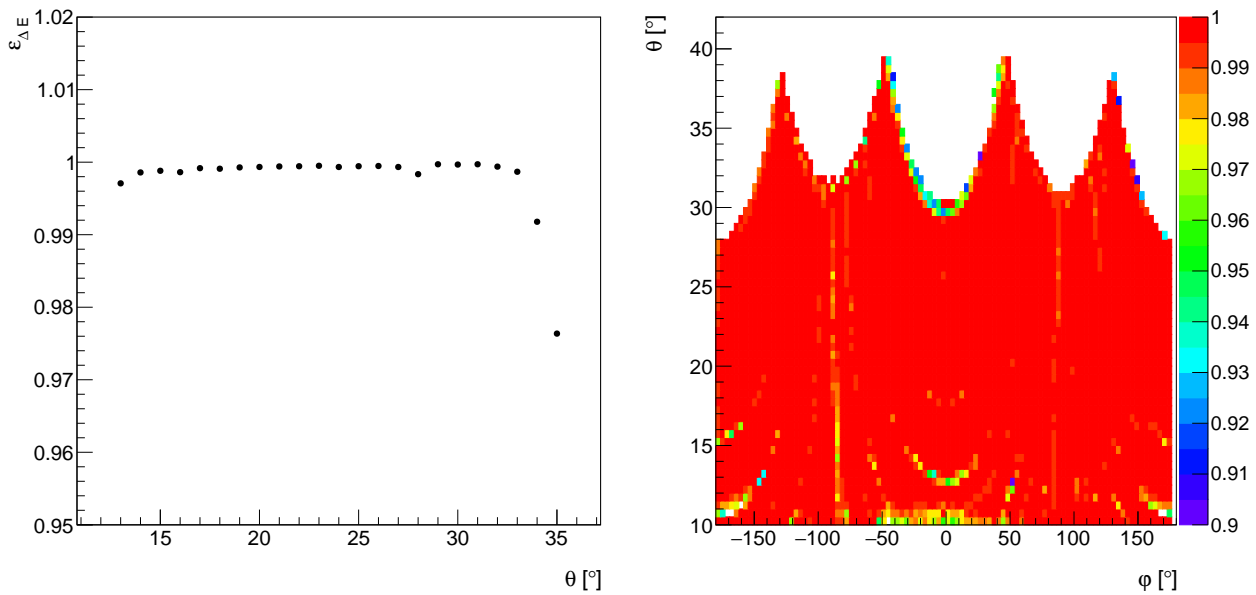
Fig. 4.12: The 1-dimensional ΔE efficiency as a function of θ angle (*left panel*) and 2-dimensional map of $\varepsilon_{\Delta E}\left(\theta, \varphi\right)$ (*right panel*).

efficiency due to gaps between the detector strips is practically negligible. Still, the correction for the ΔE efficiency has been applied to the analysis.

4.6.3 E detector efficiency

The last detector on the particle's trajectory, the E detector, consists of 10 scintillator blocks adjacent to each other (more detail in Sec. 3.2.1). Scintillator elements are thick enough to stop all the charged particles emitted at the beam energy of 108 MeV. The gaps between the scintillator blocks have the thickness of the foil wrapped around the detectors. Even when the particle hits such a gap, it will most likely stop in one of the E detector slabs, producing a signal. Therefore, we can assume that the efficiency of the E detector is 100%. However, we need to apply the correction for the hadronic interactions, cross-over events, and configuration efficiency described later.

4.7 Hadronic interaction

Another aspect to be considered in the analysis is the correction of the losses due to the hadronic interactions. This phenomenon is mainly relevant to the E detector because of its large thickness. When the registered particle undergoes a hadronic reaction, part of its energy is lost, and eventually, less light is produced. As a result, the particle's energy is underestimated, and such an event is rejected
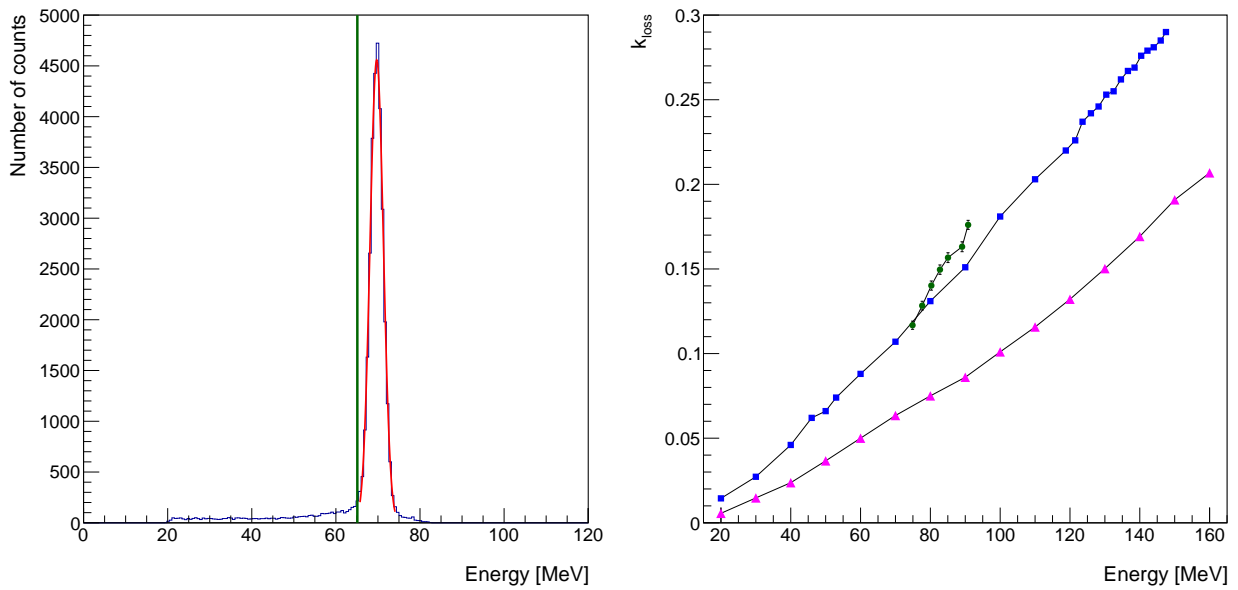
Fig. 4.13: *Left panel:* The experimental deuteron energy distribution spectrum at the selected polar angle $\theta = 20°$ with the fit of Gaussian function. The green line corresponds with the value of the -3σ from the peak position. The events summed up below this line constitute the N_{tail} value. *Right panel:* The simulated and experimental results of energy loss (k_{loss}) due to hadronic interaction in the E detector presented as an initial energy function. The blue squares and the magenta triangles represent simulated deuterons and protons, respectively. The experimental results are presented as green points with corresponding statistical errors.

from the analysis at the identification or background subtraction procedure. A set of simulations should be carried out to calculate the number of particles undergoing hadronic interaction. For the purpose of this work, the simulations presented in paper [83] were used. The simulations have been performed for a set of proton energies ranging from 20 to 160 MeV. Moreover, elastically scattered deuterons from the experiment were also used to estimate the losses associated with the hadronic interaction. The Gaussian function was fitted to the deuteron energy spectrum at the selected θ angle, which is presented in Fig. 4.13, *left panel*. The number of particles lost due to the hadronic interaction was estimated by the ratio of particles' count in the tail (N_{tail}) to all particles (N_{all}) for given energy distribution for experimental data and simulations. The N_{tail} value has been determined as the sum up of the events' number below the green line corresponding with the value of the -3σ from the peak position. The N_{all} is defined as the number of all particles counted in the whole histogram. The ratio between the N_{tail} and N_{all} is calculated:

$$k_{loss} = \frac{N_{tail}}{N_{all}}. \tag{4.9}$$

In Fig. 4.13, *right panel*, we present the results of simulations for deuterons and protons and data analysis for deuterons. The difference between the measured and simulated correction is around 12%, corresponding to a 2% error of the integrated luminosity, see Sec. 4.9.2. The final correction applied

in the further analysis is:

$$\varepsilon_{hadr} = 1 - k_{loss},\tag{4.10}$$

based on simulations. The impact of hadronic interactions on the systematic error is described in Sec. 5.2.2.

4.8 Edge events

In Sec. 4.2, we introduced the so-called edge events, when the particle deposited its energy in two adjacent E scintillators. This type of events is important for control of the setup geometry but introduces certain calibration problems when used in the regular analysis. Due to different calibrations of these detectors, energy losses in the foil separating them, and threshold effects in the case of a small energy deposit in one of these detectors, it is practically impossible to reconstruct the energy of such a particle with the required accuracy. Therefore, we reject such events and then correct them for their loss. The correction was based on the simulation and cross-checked with the data analysis. We obtain the following correction:

- 1% for deuterons. The correction was used to determine the number of elastically scattered deuterons (Sec. 4.9.1) and then the luminosity value (Sec. 4.9.2).

- 1.2% for protons. The correction was used for determining the differential cross-section as described in Sec. 5.1.

4.9 Normalization of Cross Section

Determination of the breakup cross section requires knowledge about integrated over time luminosity expressed as a formula:

$$L = (1 - \tau)\, I_0\, t\, \varrho\, \Delta x,\tag{4.11}$$

calculated as a product of beam current (I_0), measurement time (t), electronic dead time (τ), the density of interaction centers in the target (ϱ), and the target thickness (Δx). Unfortunately, it was impossible to measure the beam current due to technical problems. Moreover, since we use a liquid deuterium target, its pressure makes the thickness fluctuate and is non-uniform across the target area. As a consequence, we can not determine the target thickness with satisfactory accuracy. While the elastic scattering events are measured simultaneously with breakup reaction products, the luminosity

value is identical for both cases. The differential cross section for the elastic scattering is given by the Eq. (4.12):

$$\frac{d\sigma\,(\theta)}{d\Omega} = \frac{N^{el}\,(\theta)}{\Delta\Omega} \cdot \frac{1}{L} \cdot \frac{1}{\varepsilon(\theta)};$$

$$(4.12)$$

where:

- $N^{el}\,(\theta)$ - number of elastically scattered particles registered at the polar angle (θ_d);

- $\Delta\Omega = \Delta\theta\,\Delta\varphi\,sin(\theta)$ - the particle's solid angle; $\Delta\theta = 1°$, $\Delta\varphi = 2\pi$;

- $\varepsilon(\theta)$ - the total efficiency for particle registration. In case the elastic process the one-dimensional efficiency presented in the θ function will used (see, Sec. 4.6);

We can calculate the luminosity as a normalization factor based on the number of the elastically scattered particle (deuterons in this case) for the known elastic cross section $\sigma\,^{el}_{LAB}\,(\theta)$ (from Ref. [43]) at the studied energy and then normalize the breakup reaction. The integrated luminosity is given by the formula:

$$L\,(\theta) = \frac{N^{el}\,(\theta)}{\sigma\,^{el}_{LAB}\,(\theta)} \cdot \frac{1}{\Delta\Omega} \cdot \frac{1}{\varepsilon(\theta)}$$

$$(4.13)$$

4.9.1 Selection of elastic scattering events

In order to determine the normalizing factor, an essential quantity is a number of elastically scattered particles, protons, or deuterons. They are registered in Wall as single tracks since the coincident particle is emitted towards Ball. The energy spectra collected at polar angle $\theta = 20°$ are presented in Fig. 4.14 (protons - *left panel*, and deuterons - *right panel*).

In the *left panel* of the Fig. 4.14, we see that protons from the breakup reaction overlap with elastically scattered protons. Moreover, above the peak of elastic protons, we observe an additional peak around 108 MeV. The relevant peak has almost the same energy as the beam and is produced by the beam scattered from the target frame, see Sec. 4.2. Therefore, we decided to analyze deuterons characterized by much lower background contribution.

For this purpose, several conditions were applied. The selection of events of interest was based on the $\Delta E - E$ technique (details in Sec. 4.1.3). The particle identification procedure was implemented in
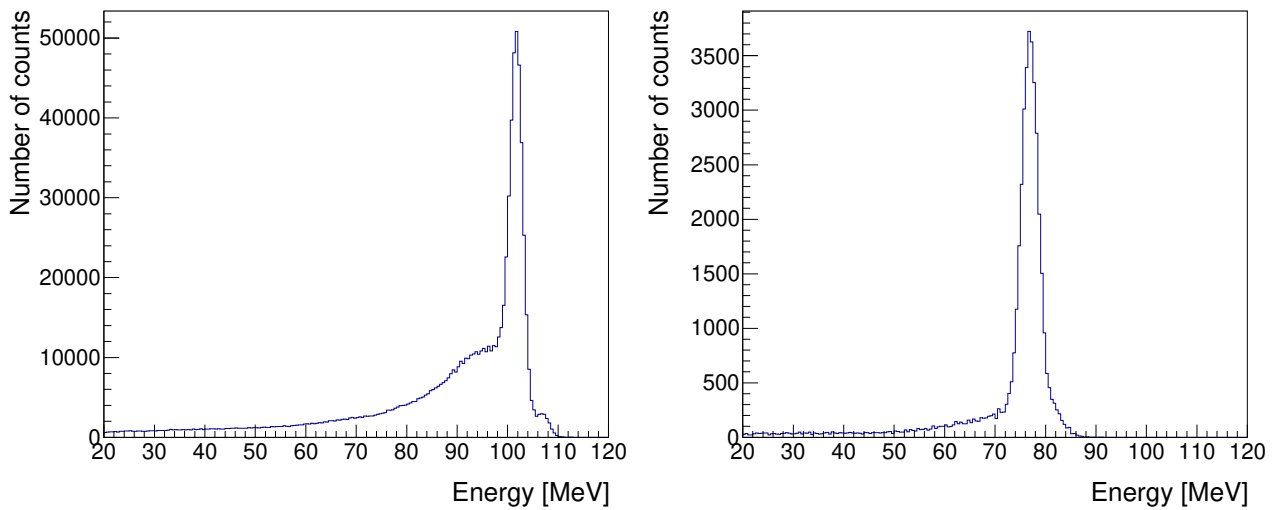
Fig. 4.14: Energy spectra of elastically scattered protons (*left panel*) and deuterons (*right panel*) registered as the single track events at a polar angle $\theta = 20°$.

such a way as to make it possible to separate the so-called "pure" deuterons from the ones overlapping in the $\Delta E - E$ spectrum with protons. We select broad deuteron cuts to avoid uncontrolled event loss in the elastic scattering analysis.

Due to the variations of the count rates in the different quarters of the detector, we analyzed the elastic scattering events quarter by quarter. In each quarter, a particle identified as a deuteron was selected as a single track at chosen polar angle ($\theta = 14°, 15°, 16°, ..., 32° \pm 0.5°$) regardless of the coincidences with a proton in Ball. Due to the square shape of our detection setup, elastically scattered deuterons above polar angle $\theta = 29°$ can only be registered in the corners. Thus, we apply limits on the azimuthal angle: $\varphi = 45° \pm 10°, \varphi = 135° \pm 10°, \varphi = 225° \pm 10°, \varphi = 315° \pm 10°$, depending on the quarter. The counts were then scaled to the quarter azimuthal angle.

The energy spectrum of elastically scattered deuterons for selected $\theta = 20°$ is presented in Fig. 4.15 in the *left panel*. Studies of the impact of the PID gate on this spectrum have shown that breakup protons had the main contribution to the background. Events affected by hadronic interactions and accidental coincidences can also contribute.

The deuteron energy is unreliable since it was reconstructed according to the proton calibration; however, its absolute value is not significant in our analysis, relying on the scattering angle, which defines the elastic scattering kinematics. In the following step, the Gaussian function was fitted to the spectrum as a basis for the background subtraction. This procedure is estimated by a linear function between limits of integration E_a, E_b related to distance of $-5\sigma, +3\sigma$ on the left, and right from the peak position E_0, respectively (cf. Fig. 4.15, *left panel*). A straight line passing through 2 points is defined by the limits of summation and the corresponding values. Events below the linear function were
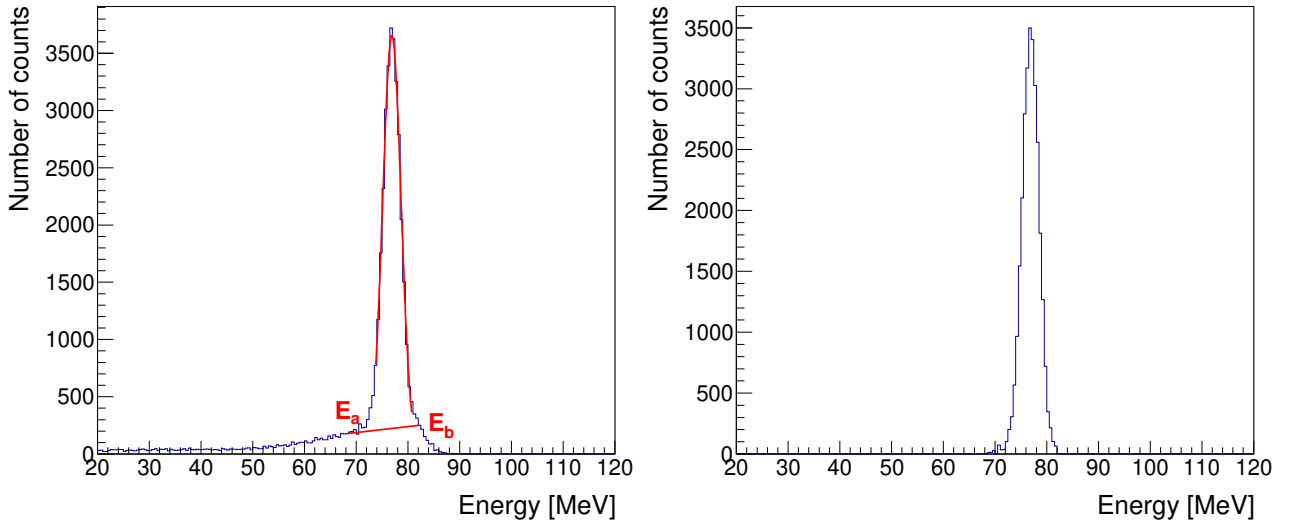
Fig. 4.15: *Left panel:* Energy spectrum of elastically scattered deuterons for a chosen polar angle $\theta = 20°$ with fitted Gaussian function. The linear function between two limits of integration (E_a, E_b) corresponds to the distance of -5σ and $+3\sigma$ on the left, and right from the peak position E_0, respectively. *Right panel:* Distribution of elastically scattered deuterons at the same polar angle after background subtraction procedure.

subtracted (Fig. 4.15, *right panel*). After subtraction, we obtained the number of elastically scattered deuterons in each quarter for a set of θ angles. The example of elastically scattered deuterons for the first quarter is presented in Fig. 4.16, *left panel*. The number of events is multiplied by 4 to normalize the results to a full range of azimuthal angles. The observed scatter of the data points is both due to efficiency variations and discrete position information from MWPC. After applying efficiency correction for each point (see Sec. 4.6.1 in Fig. 4.10), we fit a 3rd-degree polynomial for the first quarter and 5th-degree polynomials for the others. The average value of all fitting curves was calculated, and this value was taken as the correct number of counts. The polynomials denoting the number of counts in individual quarters and the average value from all of them are presented in Fig. 4.16, *right panel*.

To determine the total number of elastically scattered deuterons at a chosen θ angle, we must multiply the obtained number of counts by a factor of 2^4 due to the prescaling applied to a single trigger T1.

4.9.2   Determination of the luminosity

We need to normalize our result to a known cross section to calculate the luminosity according to Eq. (4.13). For this purpose, we use the *pd* elastic scattering differential cross section at 108 MeV measured at KVI with the use of the Big Bite Spectrometer [43]. The systematic errors have two main sources. Firstly, the total cross-section error is given in Ref. [43] and it fluctuates between 4.4% for the highest θ angles to 6.5% for the lower ones. The second source is related to our measurement and analysis. As a measure of it, we take the significant asymmetry of the count's number in the different
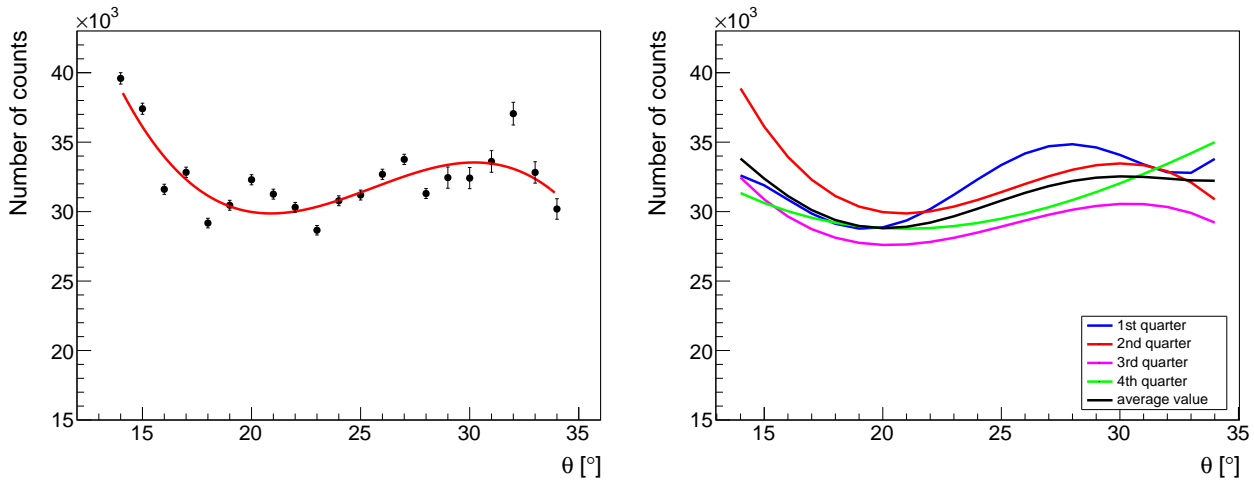
Fig. 4.16: *Left panel:* The number of the elastically scattered deuterons after background subtraction in the first quarter presented in θ angle with the fitted polynomial. *Right panel:* The 3rd and 5th-degree polynomials fitting deuterons' distribution in particular quarters and their average.

quarters of the detector. The error estimation is based on calculating the highest differences between the polynomial fitting and the average value (see Fig. 4.16, *right panel*). The systematic uncertainty varies between 5.8% for the highest θ angles and 17.9% for the lower ones. The statistical errors are minor and range between $0.07 - 0.08\%$. Fig. 4.17 shows the resulting luminosity values with their systematic uncertainties.

The final value of the integrated luminosity obtained for the set of polar angles is presented in Fig. 4.17 and is equal to $L = 8.687 * 10^6 \pm 0.265 * 10^6$. The luminosity value was calculated as a mean weighted by a systematic error according to the equation [84]:

$$\bar{L} = \frac{\sum_i (L_i - \alpha_i) w_i}{\sum_i w_i} \qquad (4.14)$$

where the sum is over experimental points measured for different polar θ angles with asymmetric uncertainties (σ_i^+ for the upper and σ_i^- for the lower error). The weights are equal to $w_i = 1/\sigma_i^2$, where $\sigma_i = (\sigma_i^+ + \sigma_i^-)/2$ and $\alpha_i = (\sigma_i^+ - \sigma_i^-)/2$, that are the parameters introduced for the unbiased estimators [84].

The average luminosity is shown in Fig. 4.17 as a red horizontal line. The points in the θ range between $14° - 29°$ are consistent within the systematic uncertainty represented by the black dashed lines, while the last point corresponding to $\theta = 32°$ is distant from the others. It is on the limit of the geometrical acceptance of the Wall detector, but the acceptance losses have been taken into account, so we do not know the reason for this shape difference between our results and the KVI data [43]. Rejecting this point from the average would not significantly change the result.
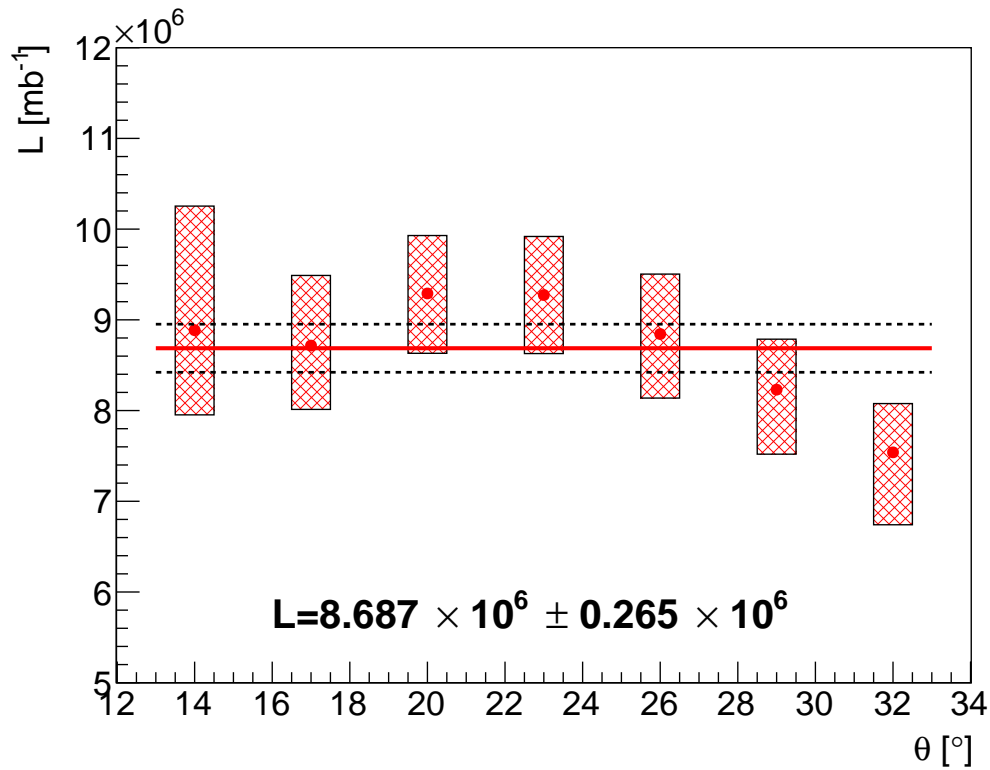
Fig. 4.17: The luminosity value obtained for the set of θ angles, calculated as a mean weighted by a systematic error represented by the hatched boxes (more details in text). The statistical errors are smaller than the point's size.

4.10 Configuration efficiency

The configuration efficiency is related to the geometrical acceptance of two coincident protons registered in the hodoscopes. The proper registration of two charged particles in the BINA Wall requires two reconstructed hits in all the MWPC planes and signals from two various elements of ΔE detector and two separate elements of the E detector. On the contrary, when two charged particles are recorded in the same ΔE or E detector, the energy or PID information is invalid. Such events are rejected from the analysis on the track reconstruction level, and we need to apply the correction for them. The probability of described situation strongly depends on the angular configuration, i.e., on the breakup kinematics.

Another aspect to consider is related to the efficiency of the coincidence trigger. The coincidence trigger condition described in Sec. 3.4.2 requires the MULT signals from the E detector's left or right side. Since the central detectors ($n = 5$ and $n = 6$) are cut in the middle, the PMT's signal from those detectors is always registered from one side (left or right). As a consequence, breakup events are omitted when the protons are detected on the opposite sides in $n = 5$ and $n = 6$ scintillators. In

this case, the protons from the breakup reaction are only classified as a single event (registered with the prescaling factor of 2^4), and the coincident trigger condition cannot be fulfilled. Therefore, we must also take into account such events in our correction.

The total configuration efficiency was calculated for each analyzed breakup configuration as a ratio of the events with complete information from all the detectors (N_g) to the total number of simulated events (N_{all}):

$$\varepsilon_{conf}(\theta_1, \theta_2, \varphi_{12}) = \frac{N_g(\Delta E, E)}{N_{all}(\Delta E, E)}. \tag{4.15}$$

The calculations were based on simulated events using the Geant4. Three sets of results obtained for several combinations of polar angles θ_1 and θ_2 are presented in function of φ_{12} in Fig. 4.18. The first and the second sets correspond to the E and ΔE efficiencies, which were analyzed separately. The third group is the total correction, including losses due to the double hits in E, ΔE detectors, and trigger efficiencies.
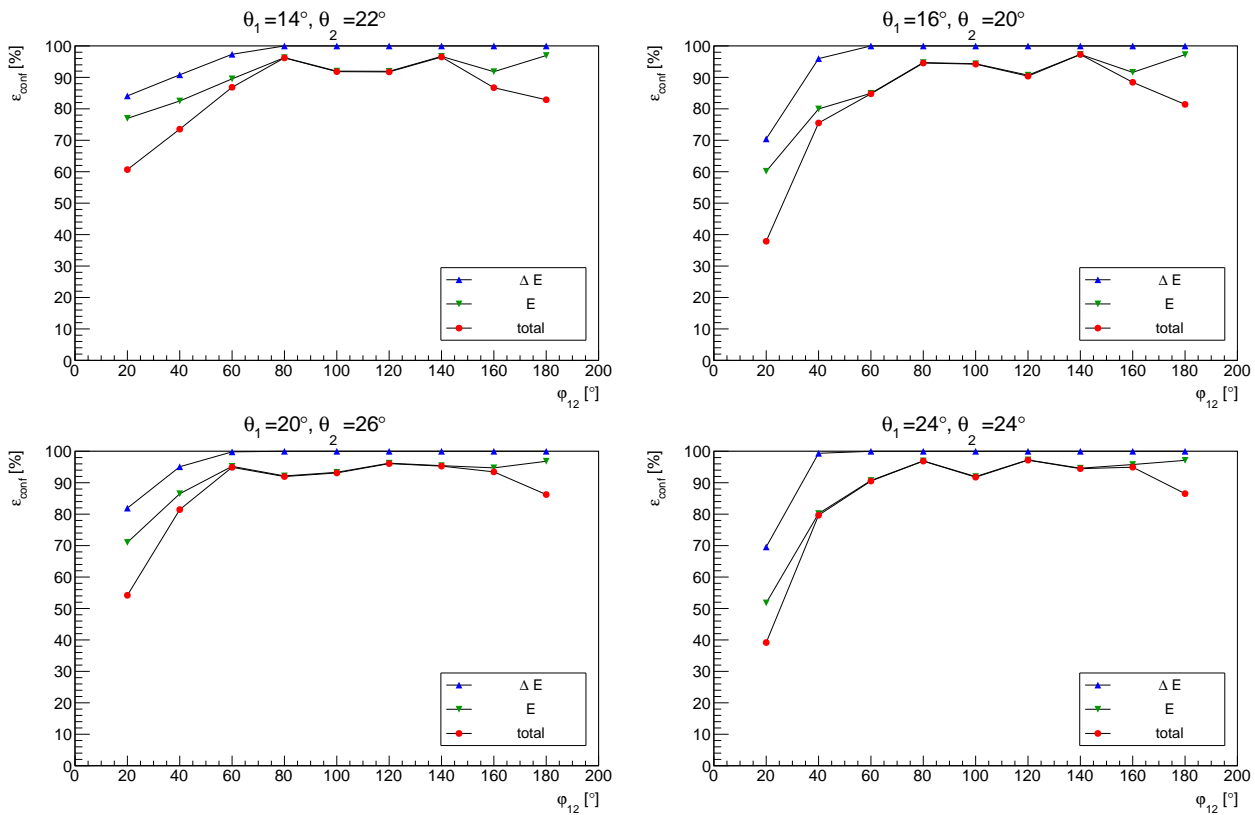
Fig. 4.18: Configuration efficiency simulation obtained for four selected θ_1, θ_2 combinations presented in a φ_{12} function. The black and green points refer to the efficiency calculated for E and ΔE, respectively. The red points represent the total configuration efficiency for the BINA detection setup.

The configurational efficiency of the E detector strongly depends on the relative azimuthal angle φ_{12}. We can observe local minima reflecting the geometrical structure of our detection setup. Inefficiencies for the smallest azimuthal angles correspond with the highest probability of detecting particles in the same E detector. For coplanar events (with the azimuthal angle φ_{12} very close to $180°$), relatively only a few events will have a chance to hit the same detector E. On the other hand, we observe the local minima for the highest φ_{12} angles connected to the efficiency of the coincidence trigger. Since the ΔE detector has more components than the E detector (24 against 10, see Sec. 3.2.1), and the particular segments cover only half of the vertical acceptance of Wall, we observe a negligible effect of configurational efficiency except in the range of the lowest φ_{12}.

Chapter 5

Breakup reaction analysis

5.1   Determination of experimental differential cross section

The main goal of this analysis is to determine the differential cross section for the ^{2}H(p,pp)n reaction at the beam energy of 108 MeV. In the following, we analyze the breakup cross section for a set of kinematical configurations within the angular acceptance of our detection system. The breakup reaction kinematics is determined by the momenta of protons $\vec{p_1}$ and $\vec{p_2}$. The geometrical configuration is defined by polar angles θ_1, θ_2 of the momentum vectors and their relative azimuthal angle φ_{12}.

The events identified as proton-proton coincidences are analyzed event-by-event and sorted according to angular configuration $(\theta_1, \theta_2, \varphi_{12})$. Due to the fact that the efficiencies of registering both protons are related to one another, the corrections for the detection efficiency were also implemented event-by-event. The following effects were taken into account for each analyzed event:

- ε_{WALL} - the Wall efficiency described in Sec.4.6,

- ε_{hadr} - the efficiency connected with the hadronic interactions, see Sec. 4.7,

- ε_{edge} - the correction for the edge events, see Sec. 4.8,

- ε_{conf} - the configurational efficiency described in Sec. 4.10.

The order of protons in the case of symmetrical configurations is random, otherwise, the proton with a lower polar angle (θ) is chosen as the first one. The range of the polar angles θ_1 and θ_2 from $13°$ to

29° has been divided into 2-degree wide bins, and the azimuthal angle φ_{12} was analyzed between $10°$ to $190°$ with the step of 20 degrees. The centers and widths of the bins are as follows:

$$\theta_1, \theta_2 = 14° \pm 1°, 16° \pm 1°, ..., 26° \pm 1°, 28° \pm 1° \tag{5.1}$$

$$\varphi_{12} = 20° \pm 10°, 40° \pm 10°, ..., 180° \pm 10°. \tag{5.2}$$

The mirror configurations, i.e., with the azimuthal angle φ and $360° - \varphi$, were analyzed together due to their cross section values. We identified the acceptance problem for the largest polar angles (see Sec. 4.9.1) thus, we limited the range of θ_1, θ_2 to $13° - 27°$, eventually obtaining the data sorted into 252 angular configurations.

Data correctly classified to the angular configuration should group around the central line of the kinematical curve in the E_2 vs. E_1 plane of proton energies (see, Fig. 5.1, *left panel*). In this spectrum, another group of events is visible in the area of the highest energies. The analysis described in Sec. 4.2 shows that these events are random coincidences of particles from the beam, degraded and scattered on the thick target frame or holder. Since these protons are located far from the kinematics, we can reject those events (without the risk of losing the good ones) by imposing an upper energy limit. The energy condition we impose ($E_1, E_2 = 90$ MeV) is graphically shown on the spectrum as bronze dashed lines (see, Fig. 5.1, *left panel*).

Such a spectrum can be transformed into two other kinematical variables. The S variable denotes the arc length value measured along the kinematic curve (see, Fig. 5.1, *left panel*) with the starting point $S = 0$ chosen arbitrarily at the point where the energy of the second proton reaches the minimum. In this analysis, the kinematical curve was sliced along its length into the segments of $\Delta S = 8$ MeV. The D variable is the distance of each data point from the theoretical kinematic curve in the $E_2 - E_1$ plane. The events inside the theoretical kinematics have a negative distance, whereas those outside have a positive D value. The example of the E_2 vs. E_1 histogram transformed into the S vs. D spectrum is presented in Fig. 5.1, *right panel*.

For each ΔS slice, the events are projected into the D axis to perform the background subtraction. We expect the distribution should reach a maximum around $D = 0$, corresponding to events grouping on the kinematical curve. In the example shown in Fig. 5.2, the *left panel*, the distribution is slightly shifted towards negative D values, which indicates that most of events are slightly below the kinematic curve. The influence of such a calibration flaw on the cross section value is described in Sec. 5.2.2.

The background is estimated by a linear function between limits of integration (E_a, E_b) corresponding to a distance of $\pm 3\sigma$ from the peak position. Events below the linear function are subtracted, as shown in Fig. 5.2, *right panel*. The D-projected distribution after the background subtraction has a Gaussian
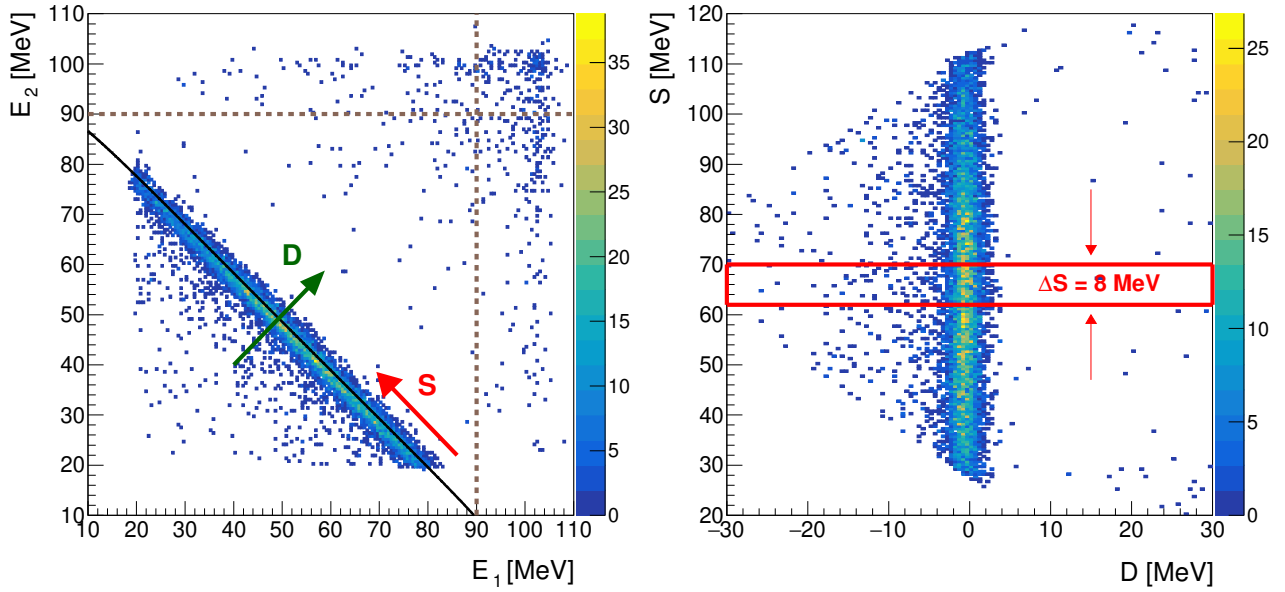
Fig. 5.1: *Left Panel*: E_2 vs. E_1 spectrum of the proton-proton coincidences obtained for a chosen angular configuration $\theta_1 = 20°, \theta_2 = 24°, \varphi_{12} = 160°$. The kinematical curve is presented as a solid, black line. The arrows show the calculated value's direction: distance (D) and arc length (S) described in the text. The bronze dashed lines graphically show the energy limit imposed on the protons (see the text). *Right Panel*: The E_2 vs. E_1 spectrum transformed into S vs. D variables. The red box represents one slice of S equal to $\Delta S = 8$ MeV, projected onto the D axis in the next step.
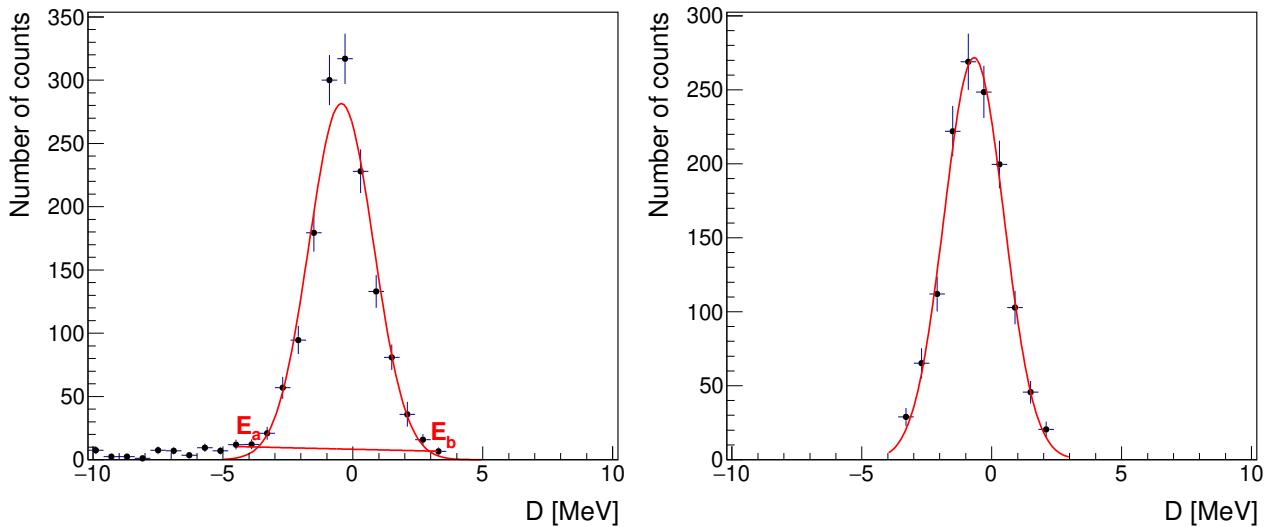
Fig. 5.2: *Left panel:* The projection of events belonging to one ΔS bin (corresponding to the red box presented in Fig. 5.1, *right panel*) onto a D axis. The background is approximated by a linear function between limits of integration (E_a, E_b). Events below the linear function were subtracted. *Right panel:* The number of events obtained after the background subtraction.
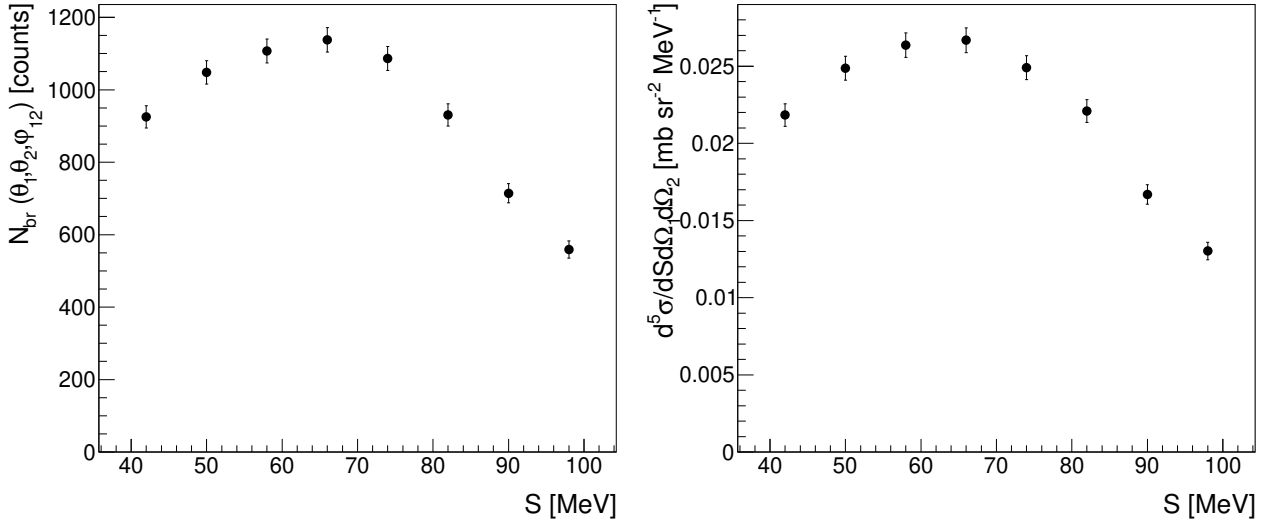
Fig. 5.3: *Left panel:* The number of events integrated for each ΔS slice presented as a function of arclength S for one selected angular configuration $\theta_1 = 20°, \theta_2 = 24°, \varphi_{12} = 160°$. Experimental points are shown with statistical uncertainties. *Right panel:* An example of the differential cross-section distribution for one selected configuration (the same one as in the *left panel*) obtained after applying the normalization procedure.

shape. The background is mainly due to hadronic interactions, and the corresponding loss of events is corrected for. The number of events, $N_{br}(\theta_1, \theta_2, \varphi_{12}, S)$ integrated for each ΔS slice is presented as a function of arclength S; see Fig. 5.3, *left panel*.

The differential cross-section of the breakup reaction for a particular angular configuration is given by the expression:

$$\frac{d^5\sigma}{d\Omega_1 \, d\Omega_2 \, dS} (\theta_1, \theta_2, \varphi_{12}, \ S) \ = \ \frac{N_{br} (\theta_1, \theta_2, \varphi_{12}, \ S)}{\Delta\Omega_1 \, \Delta\Omega_2 \, \Delta S} \ \cdot \ \frac{1}{L} \tag{5.3}$$

where:

- N_{br} - the number of proton-proton coincidences registered in a particular region of phase space after the correction for all the efficiencies: ε_{WALL}, ε_{hadr}, ε_{edge}, ε_{conf};

- $\Delta\Omega_i = \Delta\theta_i \, \Delta\varphi_i \, sin(\theta_i)$ - the solid angle for the i-th particle;

- L - integrated luminosity (more details in Sec. 4.9.2).

The differential cross-section distribution for one selected configuration after the normalization is presented in Fig. 5.3, *right panel*.

5.2   Experimental uncertainties and data consistency check

In this section, we analyze the potential sources of experimental uncertainties which affect the measured differential cross section. Table 5.1 summarizes the estimated errors - statistical and systematic ones. The statistical uncertainties were calculated point-to-point. Except for the configurational efficiency effect, which is calculated for each angular configuration separately, all other systematic errors are estimated as global uncertainties, i.e., the same for all the experimental points.

Sources of errors	The impact on breakup cross section [%]
Statistical uncertainties	$6 - 24\%$
Total systematic error	$3.9 - 8.5\%$
· Normalization	3%
· Particle identification	1%
· Configurational efficiency	$0.01 - 7\%$
· Hadronic interaction	1%
· Energy calibration	
+ angle reconstruction	
+ detector efficiency	1%
· Trigger efficiency	3%

Table 5.1: Summary of the statistical and systematic uncertainties.

5.2.1   Statistical errors

Assuming that the number of proton-proton coincidences (N) is consistent with the Poisson distribution, we calculate the statistical uncertainties according to the formula:

$$\Delta N = \sqrt{N}. \tag{5.4}$$

Due to the limited statistics of the collected data in the first experiment at CCB, the statistical error is dominant (often more significant than the systematic one).

The total statistical uncertainty is influenced not only by the number of breakup events but also by the elastic scattering events, which were the basis for the normalization. The statistical uncertainties of the breakup cross section vary between 6% and 24%.

5.2.2 Systematic effects

The systematic errors arise from a limited ability to control all the aspects of the experimental methodology, such as details of the detection system geometry or uncontrollable losses in particle registration or data analysis. In particular, we consider impacts from particle identification procedure, normalization, angle reconstruction, detector efficiency, hadronic interactions, energy calibration, and configurational efficiency. The potential sources of the systematic uncertainties and estimation of their effect on the cross section value are briefly described below.

- Normalization

  The normalization procedure was based on elastically scattered deuterons as described in Sec. 4.9. Two main factors impact the systematic error of the obtained luminosity value. The first one is given by the author of Ref. [43], and the second one is related to the spread of the number of counts in the different quarters of the detector. The systematic error for luminosity value is 3%, which has been transferred to the systematic uncertainty of the cross section value.

- Particle identification

  The registered particles were identified by the $\Delta E - E$ method based on the graphical cuts created for each hodoscope separately. The identification gates are wide enough to avoid a significant loss of particles, and a slight overlap of them is allowed. The details of this technique were described in Sec. 4.1.3. During the breakup reaction analysis, we demand that the event should be a coincidence of two particles contained within the proton gate. To estimate the identification procedure's impact on the cross-section value, we analyzed the events similarly but without the condition for the particle type. The results show that the identification gate does not significantly affect the number of counts. The distribution of breakup events for both cases (with the presence (*left panel*) and absence (*right panel*) of an identification gate) for the same S-variable and kinematic configuration are presented in Fig. 5.4. The slight increase of the cross section value calculated without the identification gate is mainly caused by a higher number of random coincidences and the contribution of hadronic events. The statement is supported by the similar increase of counts in the tail of the distribution. The impact of the identification procedure on the total systematic error was estimated at 1%.
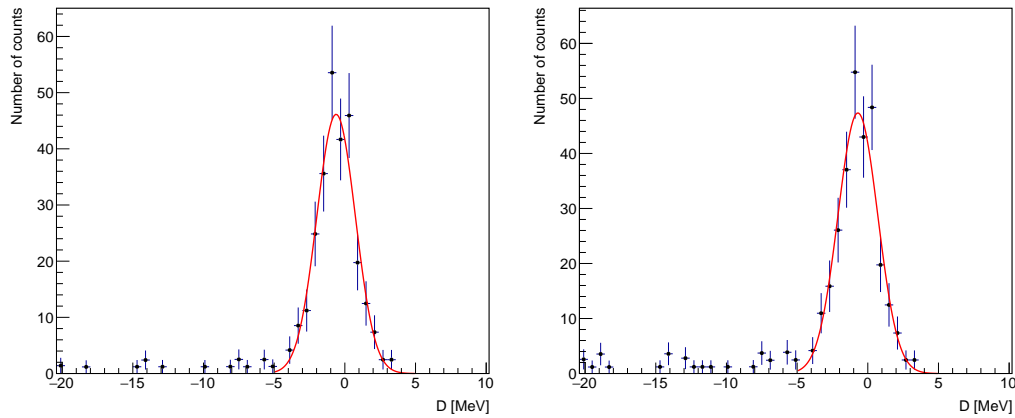
Fig. 5.4: Example of D distribution of proton pairs from the breakup reaction obtained with (*left panel*) and without (*right panel*) the PID cut; data correspond to one ΔS bin of the angular configuration $\theta_1 = 18°, \theta_2 = 20°, \varphi_{12} = 120°$.

- Configurational efficiency

  The effect coming from the configurational efficiency is closely related to the geometry of our detection system. The total configuration efficiency was calculated for each analyzed breakup configuration as a ratio of the events with complete information from all the detectors to the total number of simulated events, see Sec. 4.10. The impact of inaccuracies in the setup geometry on the configurational efficiency was estimated by moving the E detector 10 mm downwards, according to the results of the geometry checks in Sec. 4.2. The difference between results obtained in both approaches for one combination of $\theta_1 = 14°$ and $\theta_2 = 14°$ angles is presented in Fig. 5.5. The error from the geometrical effects varies between 0.01% and 7%, strongly depending on the relative azimuthal angle φ_{12}.

- Energy calibration

  The calibration procedure is described in Sec. 4.4. When the calibration is performed correctly, the breakup events should group around the central line of the kinematical curve. Some configurations barely differ from the theoretical kinematics and group slightly below the curve, which is visible in the *left panel* of Fig. 5.6. In order to analyze this effect, an artificial correction was applied based on multiplying the energy of both protons coming from the breakup reaction by a factor of 1.01. The events were analyzed in an extended range of polar ($\Delta\theta_1 = 4°, \Delta\theta_2 = 4°$) and azimuthal ($\Delta\varphi_{12} = 40°$) angles to obtain better data statistics. The *middle panel* in Fig. 5.6 shows the E_2 vs. E_1 spectrum after calibration correction. It is observed that events are grouped more centrally around the kinematical curves after the applied correction. The difference between the cross section obtained for regular calibration events and those with the correction is presented in the *right panel* of Fig. 5.6. The obtained results clearly show that the applied
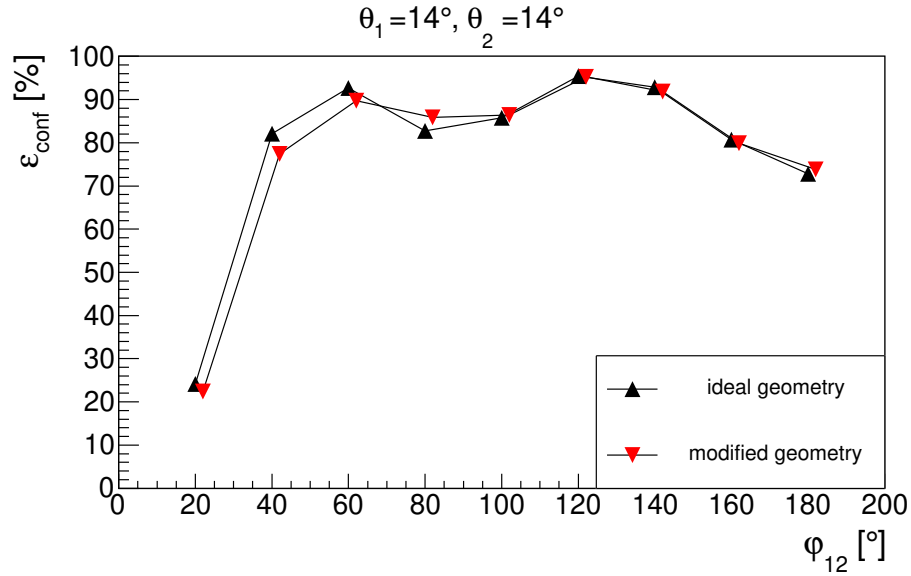
Fig. 5.5: The configurational efficiency simulated for an ideal geometry (black triangles) and the one determined after moving the E detector (red triangles). The tiny shift of red triangles has been artificially added for a better presentation of the results.
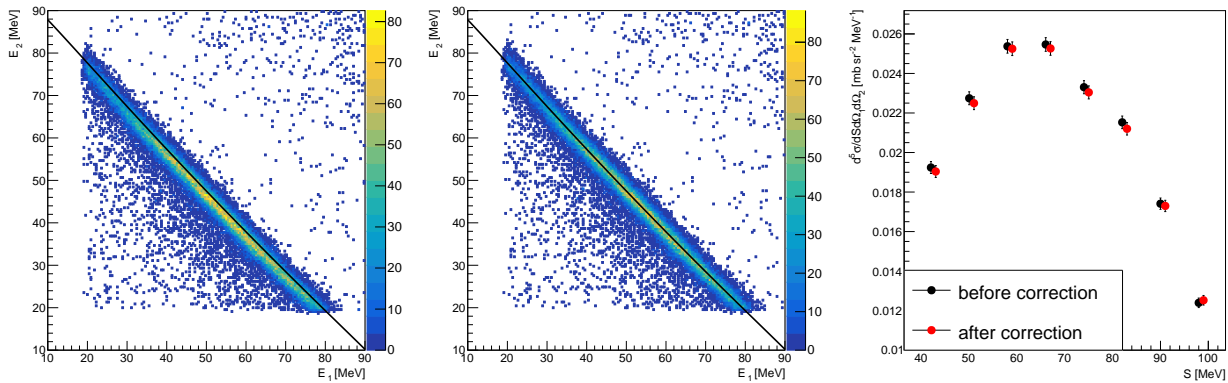
Fig. 5.6: The *left* and the *middle panel* present the E_2 vs. E_1 spectra of the proton-proton coincidences obtained for a chosen angular configuration $\theta_1 = 16° \pm 2°, \theta_2 = 20° \pm 2°, \varphi_{12} = 160° \pm 20°$ in two different ways. The *left panel* shows the data with standard calibration, while the *middle panel* presents them after the calibration correction. Kinematic curves are presented as solid, black lines. The comparison of the cross sections obtained for those situations is presented in the *right panel*. The red points are artificially shifted for a better presentation of the results.

correction does not cause any significant cross section modifications beyond the statistical limits. The total impact of energy calibration, angle reconstruction, and detector efficiency on systematic uncertainty was estimated at 1%.

- Trigger efficiency

  To correctly classify the event as a breakup, we need the information from the coincidence trigger, see Sec. 3.4.2. On the other hand, we normalize breakup to the elastic events collected with a single trigger. Trigger efficiency should not depend on trigger type or scaling. However,
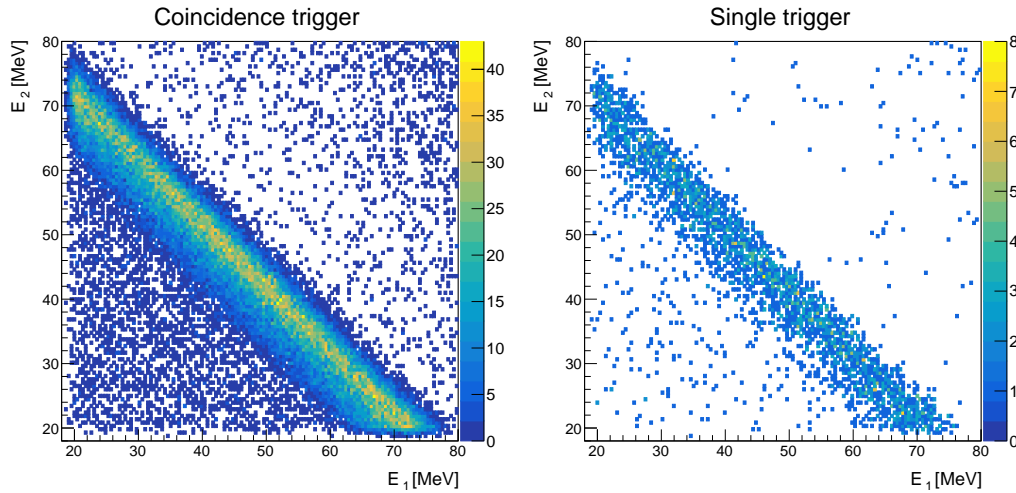
Fig. 5.7: The number of events analyzed with a coincidence (*left panel*) and single trigger (*right panel*) in the range of $\theta_1 \in (14°, 26°)$, $\theta_2 \in (14°, 26°)$, and $\varphi_{12} \in (60°, 120°)$. The total number of proton pairs for the coincidence trigger is 55593, while for the single trigger is 58576 after scaling up.

if any differences are present, they will not be canceled in the ratio. In order to study the influence of the trigger efficiency on the cross section value, the single trigger was selected in this part of the analysis. The number of proton pairs obtained for a wide angular range $\theta_1 \in (14°, 26°)$, $\theta_2 \in (14°, 26°)$, and $\varphi_{12} \in (60°, 120°)$ with a single trigger (see Fig. 5.7, *right panel*) has been adequately scaled ($T_1 = 2^4$) and compared with the number of events collected with the coincidence trigger (Fig. 5.7, *left panel*). The accuracy of this comparison is limited by the statistics, and the estimated effect is about 3%. Since the coincidence trigger provides a systematically lower number of counts, the uncertainty was implemented as an asymmetric error.

- Hadronic interactions

The correction of the losses due to hadronic interactions of protons and deuterons was calculated based on simulations, as described in Sec. 4.7. We check the simulation by comparing its results with the tail-to-peak ratio for registered elastically scattered particles (protons and deuterons). For deuterons, the difference between measured and simulated correction is around 12% (see, Fig. 4.13, *right panel*), corresponding to a 2% error of the integrated luminosity, see Sec. 4.9.2. For protons, due to the breakup contribution, we cannot perform such an analysis, hence, we relay on Ref. [23]. In this article, the difference obtained for protons fluctuates around 10-12%, resulting in 2% of the breakup cross section error. In both cases, the simulated correction is lower than the one determined from the experiment. Therefore, the error from hadronic interactions is partially canceled out in the ratio (Eq. (5.3)), and the final uncertainty was estimated at 1%.

5.2.3 Data consistency check

We also considered a systematic loss of events related to acceptance losses. Due to the square shape of our detection setup, a decrease in acceptance is observed from the polar angle $\theta \geq 29°$. For this reason, scattered particles can only be registered in the corners. We set safe limits of the azimuthal angle: $\varphi = 45° \pm 10°, \varphi = 135° \pm 10°, \varphi = 225° \pm 10°, \varphi = 315° \pm 10°$, depending on the quarter. With such a limited acceptance, the data statistics is further deteriorated. Since the polar angle bins cover the range $\theta \in (\theta - 1°, \theta + 1°)$, the detector acceptance problem can also affect the configuration with $\theta = 28°$. This was checked by comparing the cross section for the analysis without and with such a cut on the corners, as presented in the *left* and *right panels* in Fig. 5.8. As is observed in the *right panel* of Fig. 5.8, after applying the limitation on the φ_{12} angle, the cross section value changes significantly, which imposes the corner cuts are necessary. Moreover, the *right panel* in Fig. 5.8 shows a significant increase in the statistical error, unambiguously revealing a decrease in the number of registered coincidences in such detector limitation. The presented angular configuration is one of the best with respect to the collected statistics. For this reason, we decided not to include the cross section results for the configurations with central value $\theta = 28°$.
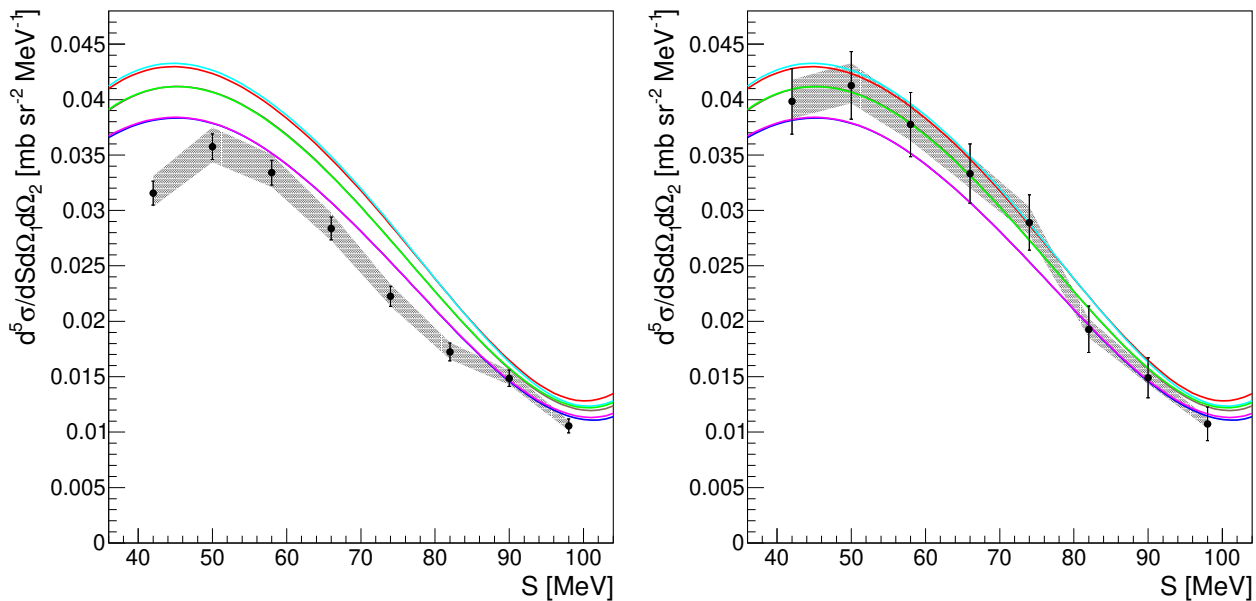
Fig. 5.8: The differential cross section determined for the same angular configuration $\theta_1 = 18°, \theta_2 = 28°, \varphi_{12} = 180°$ without (*left panel*) and with (*right panel*) the limitation on the azimuthal angle φ_{12}.

5.3   Averaging the theoretical cross-section

To compare the experimental data with available theories for the ^{2}H(p,pp)n breakup reaction, we need to consider the following aspects. Our data analysis defines the angular configuration of the breakup events with certain angular acceptance around the central configuration. The events have been sorted into 2-degrees and 20-degrees wide bins for the polar and azimuthal angles, respectively. The *right panel* of Fig. 5.9 presents theoretical calculations for one chosen angular bin in the same range as the experimental data were determined. Due to their significant differences, averaging the calculated cross section values over the same range is necessary. Therefore, the theoretical cross-sections have been calculated for the central configuration and all the combinations: $\theta_1 \pm 1°$, $\theta_2 \pm 1°$, and $\varphi_{12} \pm 10°$. Moreover, all the available theories were calculated non-relativistically, and a different kinematic curve characterizes each configuration. To solve this kinematic problem, we project all the theoretical distributions onto a common, central relativistic kinematic. Fig. 5.9, *left panel* shows an example of two selected non-relativistic kinematic curves (black lines) and a central relativistic kinematic curve (red line). Afterwards, we determine the average of the theoretical cross section values, weighted with the solid angle of a particular configuration for each step of the S-variable. Additionally, we also take into account the range of the S-variable, which in our work is $\Delta S = 8$ MeV, where the cross section values are averaged ($S\pm 4$ MeV). Finally, we obtain the one averaged theoretical distribution to be compared with the experimental results.
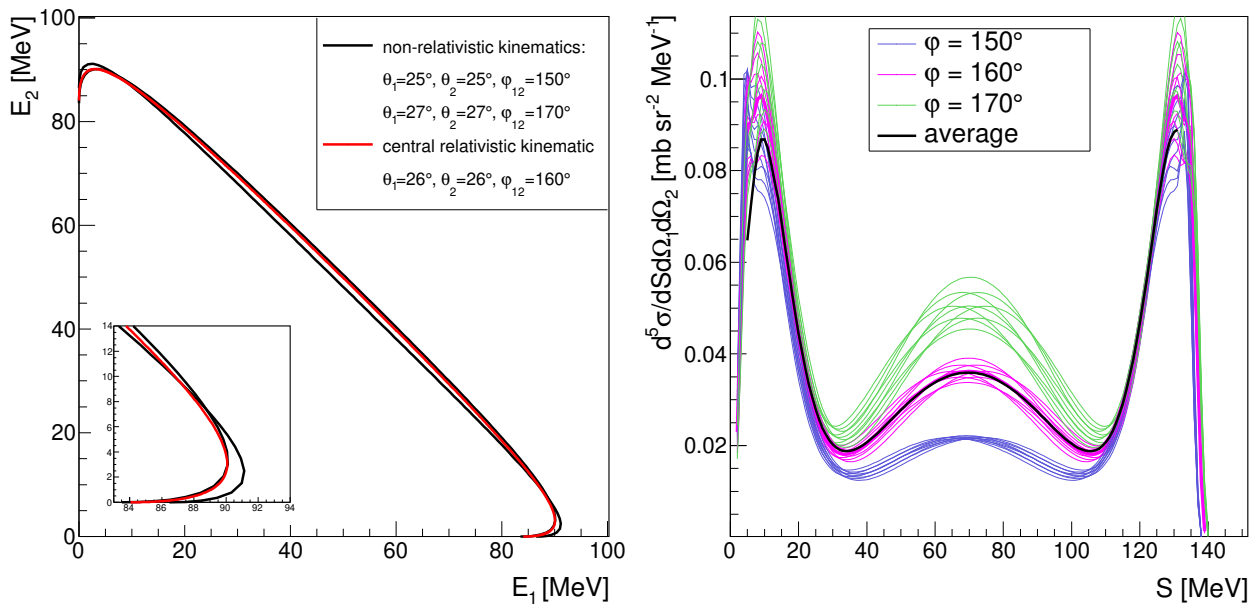
Fig. 5.9: *Left panel:* An example of two selected non-relativistic kinematic curves (black lines) belonging to the same set around the central values, which we project onto a central relativistic kinematic curve (red line). *Right panel:* Theoretical differential cross-section calculated with the CDB+Δ+C model. All theoretical curves are contained within the limits of averaging: $\theta_1 = 26° \pm 1°$, $\theta_2 = 26° \pm 1°$, and $\varphi_{12} = 160° \pm 10°$. The colors of the curves are related to various φ angles. The average theory is presented as a black line.

Chapter 6

Experimental results and comparison with theory

The differential cross section for proton pairs coming from the pd breakup reaction at 108 MeV was analyzed for the 252 angular configurations. It is presented in a function of the S-variable and compared with theoretical predictions obtained by two groups of theoreticians (more details about modeling interactions in Chapter 2). In all the calculations, the CD-Bonn potential was used for modeling the basic nucleon-nucleon (NN) interaction. Calculations of Witała et al. were performed with the Tucsone-Melbeurne 99 3NF model (later referred to as CDB+TM99) and with pure NN potential (CDB Witala). The calculations of A. Deltuva's are based on the approach developments of the Lisbon-Hanover-Vilnius group with the CD-Bonn potential (CDB Deltuva), where the 3NF model is implemented by adding the Δ-isobar excitation by using the Coupled-Channel approach (CDB+Δ). Moreover, the latter theories were extended by introducing the Coulomb interaction as an additional parameter (correspondingly CDB+C and CDB+Δ+C). All the theoretical cross sections have been averaged according to the method described in Sec. 5.3.

The examples of the differential cross section for the pd breakup reaction obtained for two different angular configurations are presented in Fig. 6.1. One configuration is asymmetrical (*left panel*), with the polar angles $\theta_1 = 16°$, $\theta_2 = 20°$, and coplanar, $\varphi_{12} = 180°$. The second one (*right panel*) is symmetrical and characterised by a low azimuthal angle: $\theta_1 = 14°$, $\theta_2 = 14°$, $\varphi_{12} = 20°$, where the Coulomb effect is strongly dominant. The available theoretical calculations are shown as a colored lines, as described in the legend, common for both panels. All the results for 252 configurations are presented similarly in Appendix A.

69
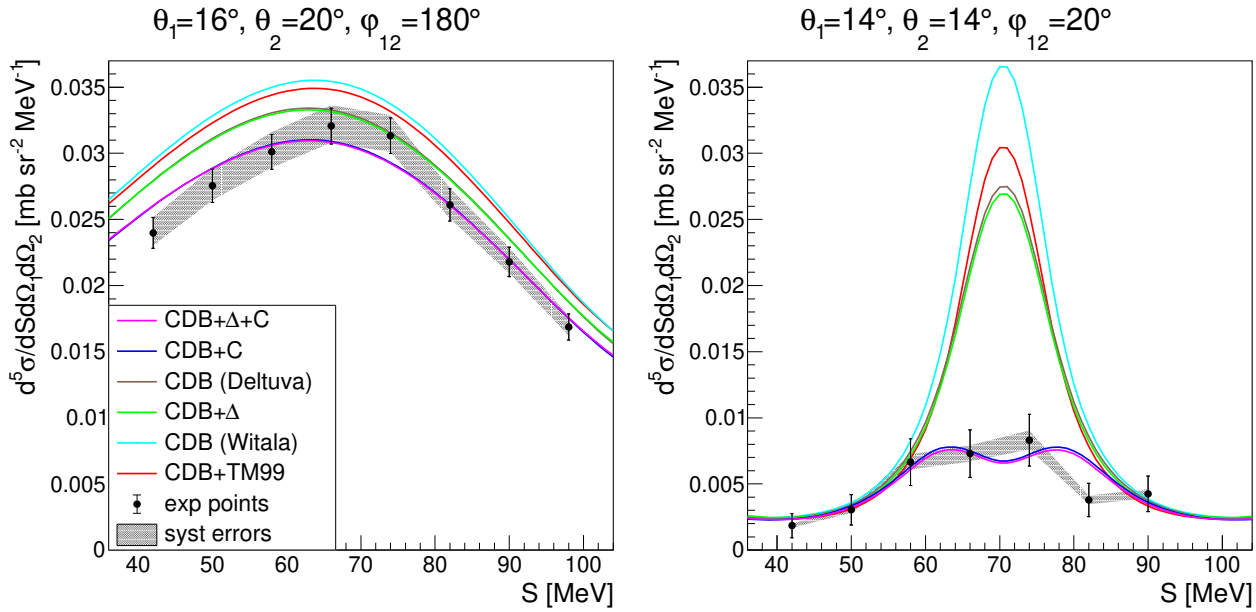
Fig. 6.1: Examples of the differential cross section for pd breakup reaction for two angular configurations - asymmetrical (*left panel*), $\theta_1 = 16°$, $\theta_2 = 20°$, and $\varphi_{12} = 180°$, and symmetrical one (*right panel*) $\theta_1 = 14°$, $\theta_2 = 14°$, and $\varphi_{12} = 20°$. Black points represent the experimental data with statistical errors, and gray bands illustrate the systematic uncertainties. The available theoretical calculations are shown as colored lines, as described in the legend, common for both panels.

6.1 Reduced chi-squared analysis

A quantitative comparison between the experimental data and theoretical predictions was performed on the basis of a reduced chi-squared. A reduced chi-squared (χ^2_{red}) is a chi-squared per degree of freedom, defined as follows:

$$\chi^2_{red} = \frac{1}{N} \sum_{i=10}^{N} \left(\frac{\sigma_i^{exp} - \sigma_i^{th}}{\Delta\sigma_i^{tot}} \right)^2, \tag{6.1}$$

where σ_i^{exp} and σ_i^{th} are the experimental and theoretical values of the cross section given for each $i-th$ point, respectively. The $\Delta\sigma_i^{tot}$ is the total uncertainty of each experimental point, calculated as $\Delta\sigma_i^{tot} = \sqrt{(\sigma_{stat}^2 + \sigma_{syst}^2)}$, where σ_{stat} is a statistical, and σ_{syst} - a systematic uncertainty. χ^2 per degree of freedom is determined for different cases of data sorting. In the first situation, χ^2_{red} has been computed as a global factor, and the N value corresponds to the total number of all data points over which we sum up. The second case applies to a situation where χ^2_{red} is calculated for each angular configuration separately, where the N value is the number of experimental points in a given configuration. Both cases of the χ^2_{red} were determined for all the theories used for comparison with the obtained experimental cross section. The global χ^2_{red} is shown in Fig. 6.2, while the values of χ^2_{red} obtained for individual configuration are presented as the 2-dimensional map in a logarithmic scale,
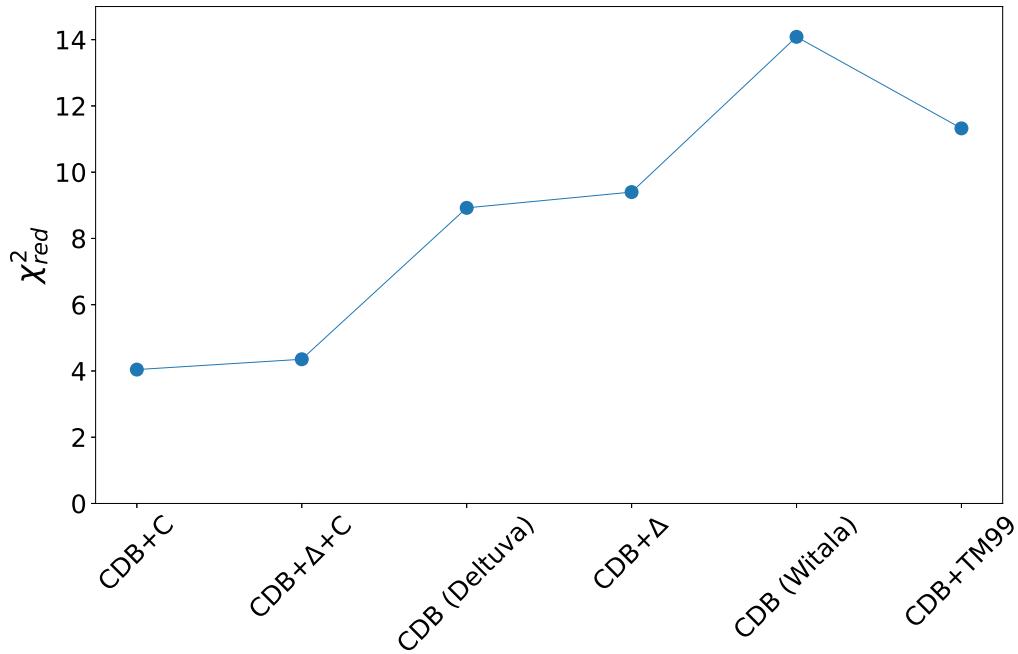
Fig. 6.2: The global χ^2_{red} obtained for all data points determined for each theoretical calculation individually.

see Fig. 6.3-6.5. Later, we present χ^2_{red} calculated for data points grouped with respect to the φ_{12} and average polar angle values.

Comparing the ^{2}H(p,pp)n breakup reactions data with the theoretical calculations, we can observe that the obtained results for the proton-proton coincidences strongly depend on the theoretical model, which reflects a global χ^2_{red} values varies from approximately 4 to 14 (Fig. 6.2). For calculations performed by Witala et al., both theoretical models have the worst agreement between the theory and data. Admittedly, adding a three-nucleon force improves the χ^2_{red} compared to the pure CD-Bonn potential, but still, its value shows a large discrepancy. Analysis of the χ^2_{red} for the theoretical calculations performed by Deltuva shows a little different picture. His calculations reveal that the impact on the global χ^2_{red} by adding the Δ-isobar is very low and even spoils the agreement between the data and theory. In the case of pure CD-Bonn potential with and without Δ-isobar, we observe better results than Witala models, however, there are still significant discrepancies between measurement and theory. The difference in results obtained with the same NN potential by the two groups is probably due to a different isospin structure assumed in both cases. The calculations of H. Witała et al. were performed with np interaction in the $1s_0$ wave, while calculations of A. Deltuva were performed using both pp and np interactions in all isospin triplet waves, including 1/2 and 3/2 total 3N isospin components.

The analysis of the global χ^2_{red} clearly shows significant improvement in the description when including the Coulomb force, in particular for the CDB+C model. Also, in this case, the impact from Δ-isobar does not improve the χ^2_{red}, we even obtain about 7% higher χ^2_{red}.
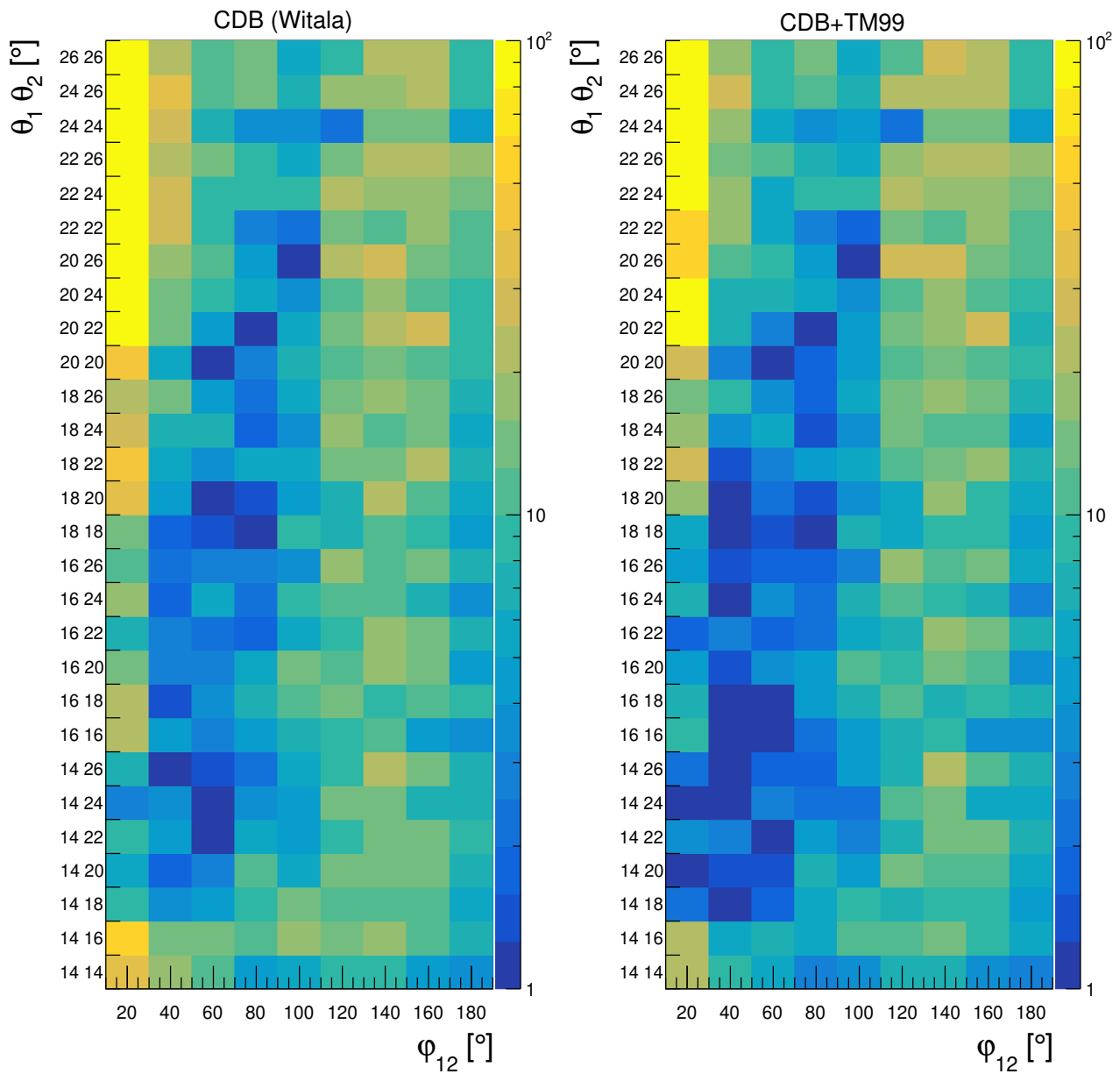
Fig. 6.3: The χ^2_{red} results obtained for all angular configurations separately, presented as the 2-dimensional map in a logarithmic scale for two selected theories: CDB (Witala) and CDB+TM99.

The χ^2_{red} calculated for each angular configuration for theories without Coulomb (Fig. 6.3, 6.4) demonstrates that some regions on maps have a giant disagreement between the data and theories.

These regions are located mainly for the smallest φ_{12} and in the upper part, corresponding to the higher polar angles θ_1 and θ_2. The more detailed analysis of the data sorted according to the azimuthal angle φ_{12} (Fig. 6.7) and polar angles θ_1 and θ_2 (Fig. 6.8) confirms this observation, showing simultaneously that the greatest discrepancy is for $\varphi_{12} = 20°$.

As we know from experiments at other beam energies, this region is particularly sensitive to Coulomb
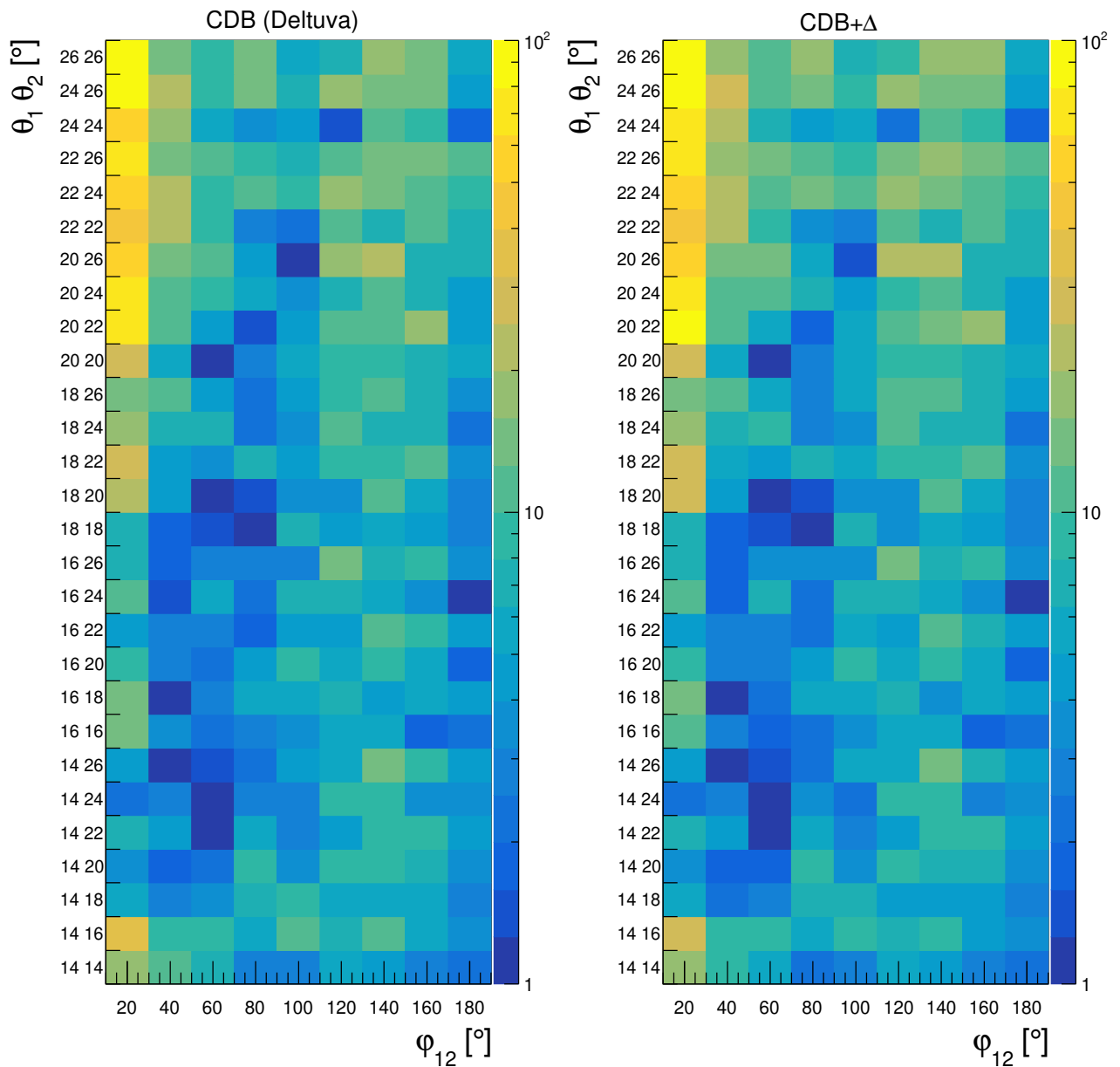
Fig. 6.4: Similar as in Fig. 6.3, but for different theoretical models: CDB (Deltuva) and CDB+Δ.

interactions, thus, the calculations neglecting the Coulomb repulsion between protons fail in describing the data. Indeed, adding the Coulomb interaction incredibly improves the situation, as shown in Fig. 6.5. In Fig. 6.6, we present the same results on a linear scale limited to 10 to observe the remaining discrepancies and possible differences between calculations with and without Δ. The data description is good except for the region combining relatively large polar angles and low φ_{12}.

Additionally, we observe that all the theories (including those with Coulomb) reach minimum of χ^2_{red} in a similar region (between $\varphi_{12} = 60°$ and $\varphi_{12} = 100°$ and for $\varphi_{12} = 180°$, see Fig. 6.7. Fig. 6.8 shows a minimum of χ^2_{red} between $(\theta_1 + \theta_2)/2 = 16°$ and $(\theta_1 + \theta_2)/2 = 19°$, observed for all theoretical calculations.
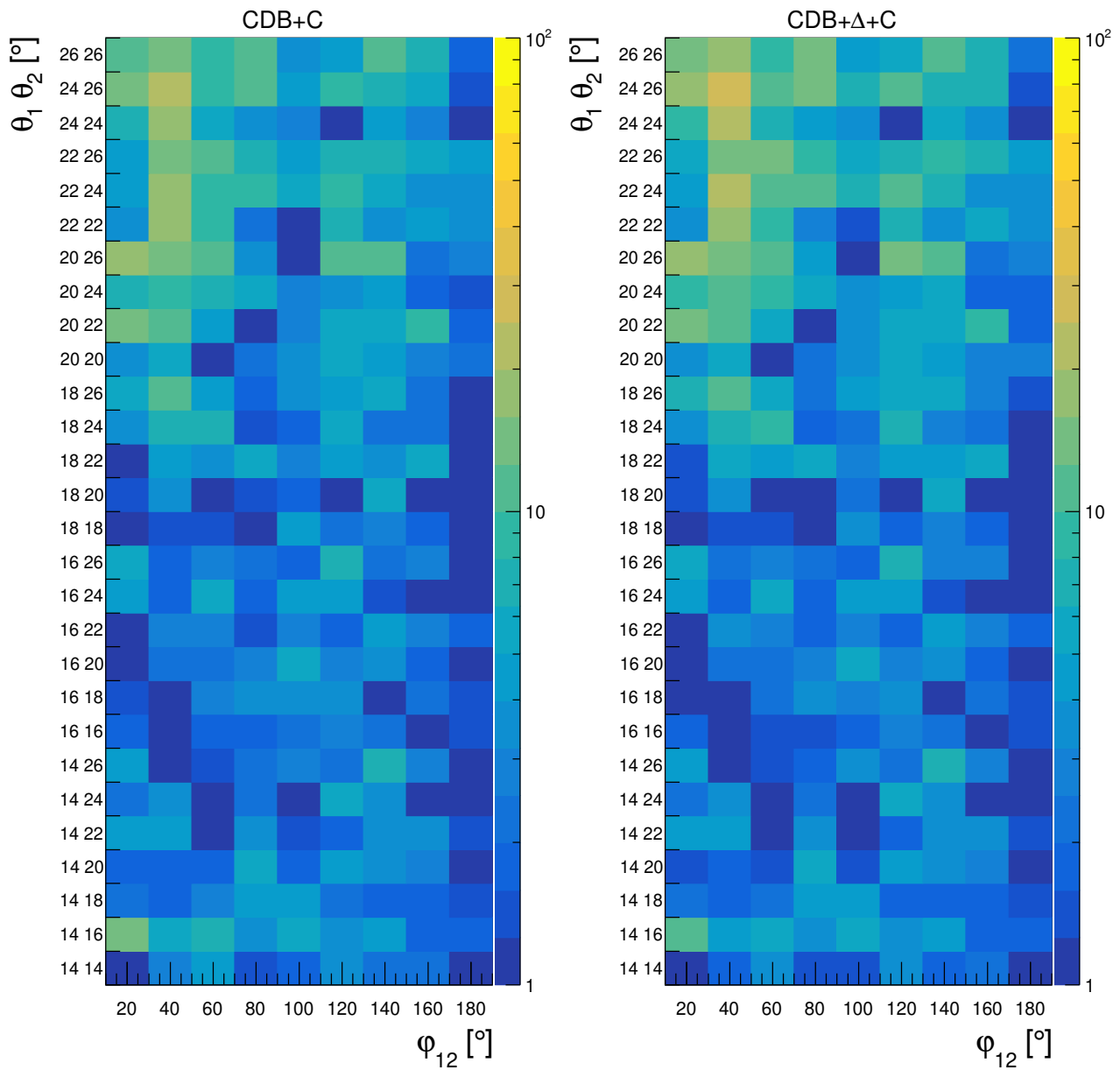
Fig. 6.5: Similar as in Fig. 6.3, but for different theoretical models: CDB+C and CDB+Δ+C.

Finally, we can conclude that the contribution of the Coulomb force in the analyzed range of protons energies and angular configurations is very significant, observed in χ^2_{red} differences for theories calculated with and without it. On the contrary, the effect of the three-nucleon force is negligible.
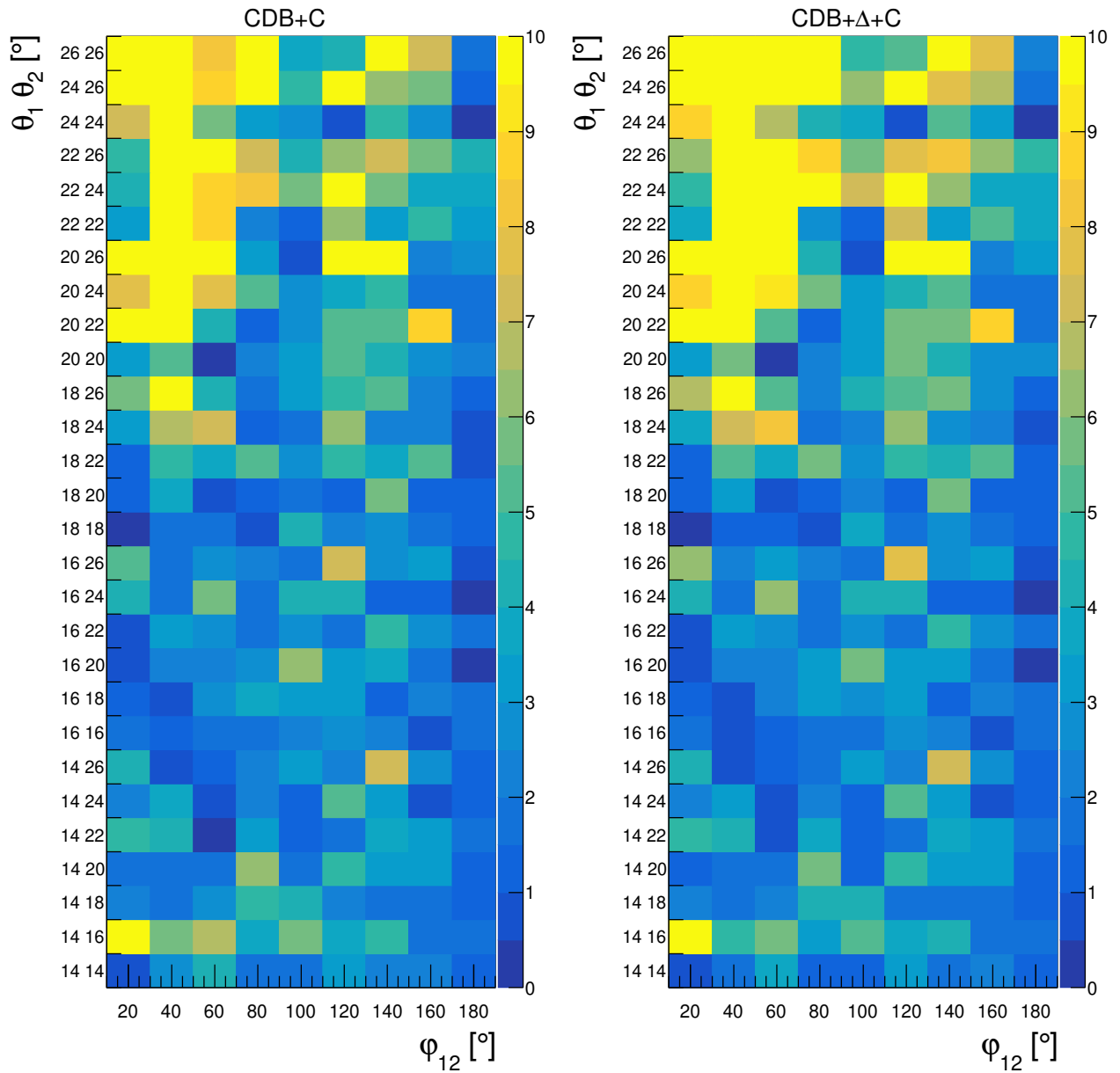
Fig. 6.6: The χ^2_{red} results obtained for all angular configurations separately, presented as 2-dimensional maps in linear scale for two selected theories: CDB+C and CDB+Δ+C.

6.2 Discussion of the experimental data results

As the χ^2_{red} analysis shows, the theories with Coulomb have the best agreement between measured data, but still, these values remain large. Analysing individual distributions presented in Appendix A one can observe that the data are usually overestimated, which may suggest the data normalization problem.

Therefore, we perform an additional test. The value of the cross section for each experimental point was multiplied by a factor ranging from 0.95 to 1.25. Then, χ^2_{red} was again determined for the two
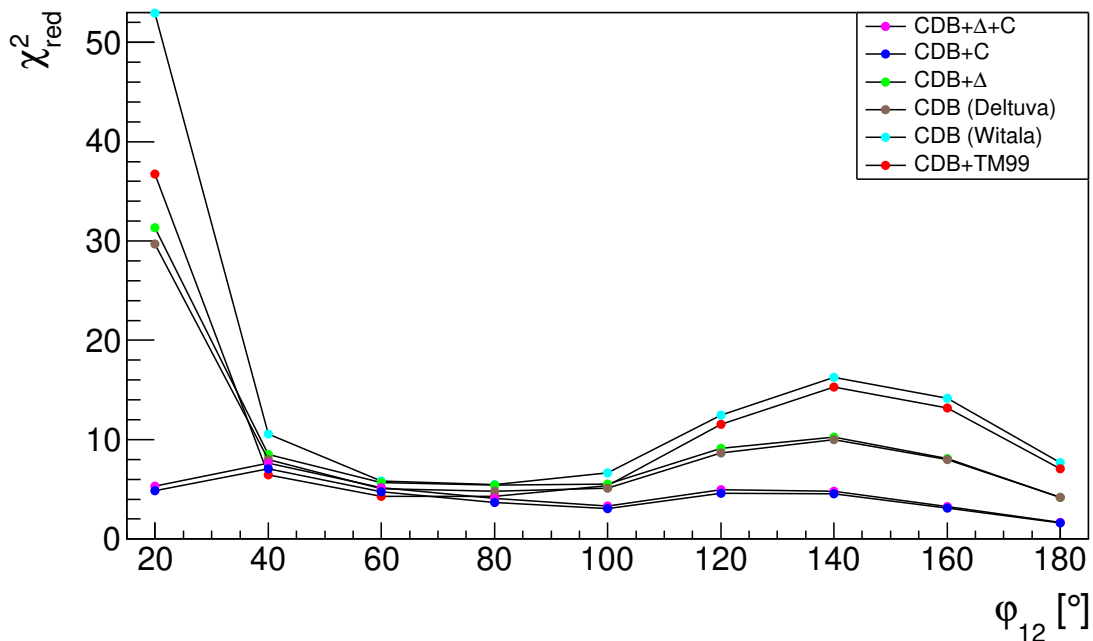
Fig. 6.7: The χ^2_{red} results presented as a function of the relative azimuthal angle $\Delta\varphi_{12}$.
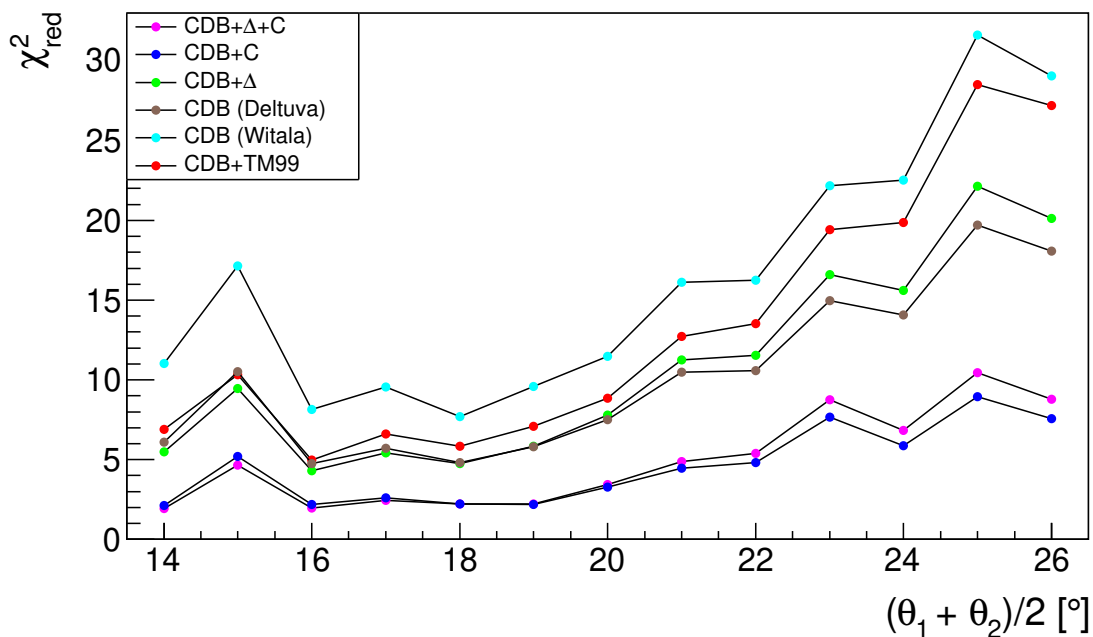
Fig. 6.8: The χ^2_{red} results presented with respect to the average of θ_1 and θ_2.
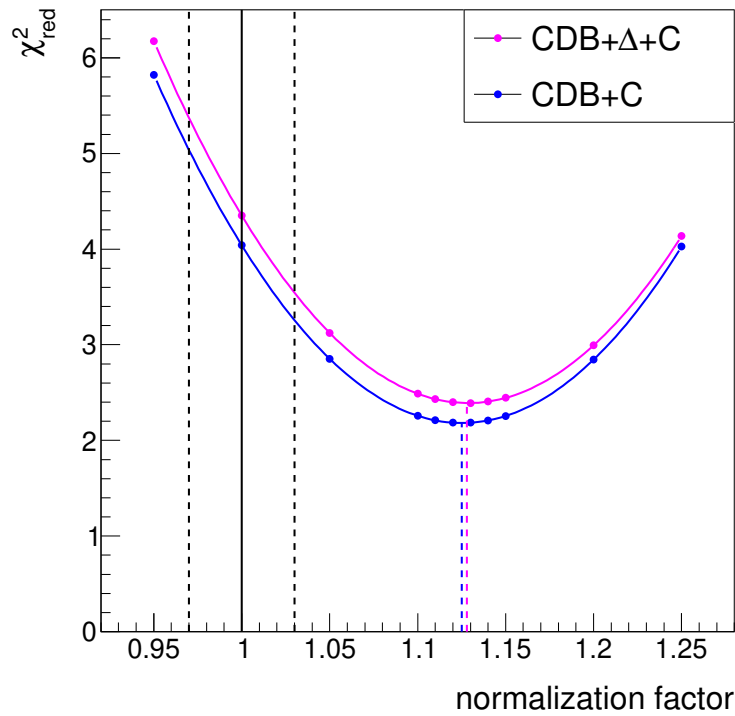
Fig. 6.9: The global χ^2_{red} obtained for two theoretical calculations with the Coulomb interaction: CDB+Δ+C (magenta color) and CDB+C (blue color) for a different normalizing factor (more detail in text). The black lines refer to our normalization (solid line) with the range of systematic errors (dashed lines).

theories with Coulomb interaction, presented in Fig. 6.9.

As shown in Fig. 6.9, for the CDB+Δ+C calculation (magenta color), after fitting the parabola, we can find the chi-squared minimum, $\chi^2_{red} = 2.395$ for a factor of 1.128. For the CDB+C theory (blue color), the minimum chi-square value equals $\chi^2_{red} = 2.185$ for a factor of 1.125. The black dashed line refers to our normalization with the range of systematic errors. Analysis of the global χ^2_{red} reveals that our normalization might be underestimated by about 12%. This problem will be further studied with the use of the new data. In this case, normalization to the elastic scattering measured absolutely with the CD_2 target will be performed. In addition, the selection of elastic scattering events will be improved due to the measurement of Wall-Ball (deuteron-proton) coincidences.

The result of this work is the differential cross sections for the pd breakup reaction determined for the energy of 108 MeV from the first BINA experiment in the CCB. So far, for the energy of 108 MeV, only the differential cross section for elastic scattering was determined in the measurement at KVI [43]. As shown in this paper, and in Fig. 1.1, theoretical calculations taking into account the three-body force (CDB+Δ) significantly improve the minimum of the pd cross section compared to the pure CDB potential. A comparison of the breakup cross sections obtained in this work with theoretical calculations shows that the effect of the 3NF force is negligible. However, we have studied only a part
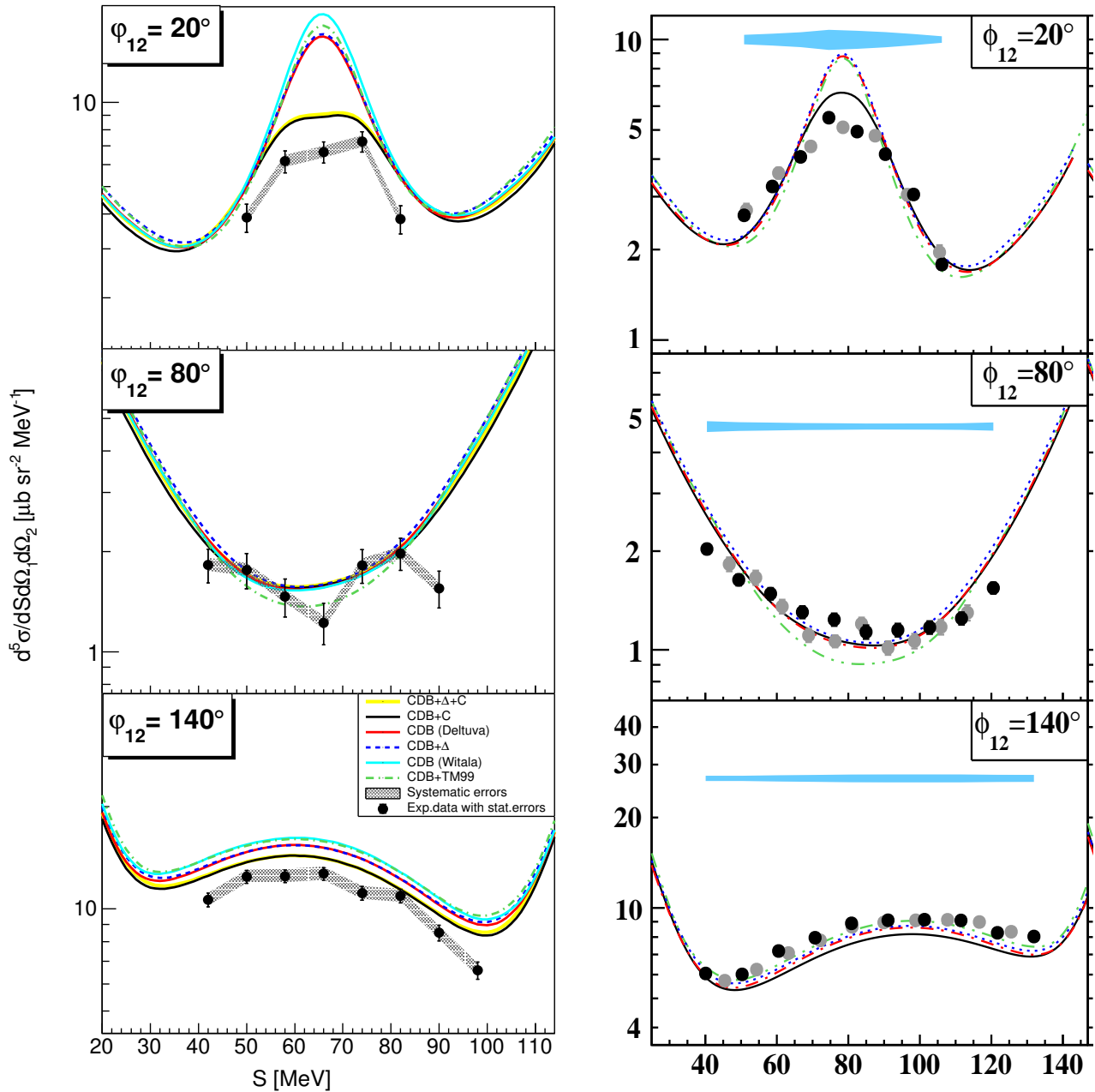
Fig. 6.10: The comparison of our data (*left panels*) with the data from [85] (*right panels*) obtained for a proton beam at 135 MeV for one combination $\theta_1 = 20°$, $\theta_2 = 24°$ for three different azimuthal angles, $\varphi_{12} = 20°$, $\varphi_{12} = 80°$, and $\varphi_{12} = 140°$, presented in a logarithmic scale.

of the phase-space. Configurations close to the so-called neutron-proton FSI are kinematically similar to the elastic scattering and can reveal stronger sensitivity to 3NF.

In order to put the results into a larger perspective, our experimental data (Fig. 6.10, *left panels*) were compared with the data from the same reaction for the nearest beam energy of 135 MeV, measured in KVI [85], presented in the *right panels* of Fig. 6.10. For comparison, we choose one combination of

$\theta_1 = 20°$ and $\theta_2 = 24°$ for three different azimuthal angles, $\varphi_{12} = 20°, \varphi_{12} = 80°$, and $\varphi_{12} = 140°$. The KVI data were sorted into mirror configurations, with $\theta_1 = 24°$ and $\theta_2 = 20°$, thus, the S-variable went in the opposite direction, and the cross section distributions have the mirror-reflected shape when compared to our data. All the distributions are presented in a logarithmic scale.

The data in the top panels of Fig. 6.10 (with the relative azimuthal angle $\varphi_{12} = 20°$) demonstrate a noticeable sensitivity to the Coulomb effect. Moreover, the data are underestimated in both cases, showing an even stronger Coulomb effect than predicted theoretically. The central panels show the results for $\varphi_{12} = 80°$, where the influence of Coulomb interaction is minimal, and all theories correctly describe the data for both energies. A difference between the two beam energies is observed at the largest φ_{12} of $140°$ (bottom panels). The breakup data at 108 MeV are overestimated, while at 135 MeV - underestimated by the theoretical predictions. The comparison with the data taken in 2019 for beam energy of 160 MeV will be essential for checking if these effects change systematically with energy.

Chapter 7

Summary and outlook

The main goal of this dissertation was to determine differential cross-sections for the ^{2}H(p,pp)n reaction. For this purpose, the BINA detection system has been installed at Cyclotron Center Bronowice. The data were registered by the forward part of BINA (Wall) at the first experimental run at CCB with a proton beam energy of 108 MeV, using a liquid deuterium target. This measurement was a part of the broader program focused on testing the three-nucleon system dynamics at beam energies of 108, 135, and 160 MeV. The work concentrated on the data analysis from two processes: elastic scattering and breakup reaction. The differential cross-section for the pd breakup was determined analyzing the proton pairs, while the deuterons from the elastic scattering were the basis of the normalization procedure to a known cross-section at 108 MeV measured at KVI [43]. As a result of this work, we have obtained differential cross sections for the breakup reaction for a set of 252 angular configurations of outgoing protons in the range of polar angles from 13 to 27 degrees and azimuthal angles from 10 to 180 degrees, which gives 1767 data points.

The experimental results have been compared to the state-of-the-art theoretical calculations based on the CD-Bonn potential, considering the 3NF effects introduced in two ways (TM99 and Δ-isobar models) and Coulomb interactions between protons. The quality of the data description was determined by performing the reduced chi-square (χ^2_{red}). Among all the compared theoretical models, the best agreement was obtained for the calculations including Coulomb interactions (CDB+C and CDB+Δ+C). For those models, the χ^2_{red} value was approximately 4, whereas within the same theoretical model, but without Coulomb interaction, the χ^2_{red} was more than twice higher. The results reveal that the Coulomb interaction has to be necessarily included in the theoretical description and cannot be neglected for the analyzed energy and angular configurations. The second main conclusion is that the impact of the Δ-isobar effect is negligible in the presented data and even slightly increases the χ^2_{red} value if added to a particular potential. On the other hand, the influence of another 3NF

model (TM99) is more significant and improves the agreement with the experimental data. The only region where the Coulomb effects are almost negligible corresponds to the relative azimuthal angles between 60 and 80 degrees. Additionally, we want to point out the observed discrepancy between the calculations with the pure CD-Bonn potential obtained for the different theoretical groups, very probably reflecting the sensitivity of the result to the assumed isospin.

By comparing the experimental results with theoretical predictions including Coulomb interactions, we observe a relatively good agreement concerning the shape of the cross-section in the whole range of measured angles. On the other hand, the measured observables are underestimated. It may suggest a stronger Coulomb effect than predicted theoretically, which was also observed previously in the data obtained in KVI [85] (see Fig. 6.10). However, this effect may also be caused by an unknown systematic bias of the applied normalization procedure based on the known cross section for the elastic scattering.

In order to verify the above conclusions, in future studies, we want to directly measure the absolute value of the differential cross section by using the solid CD_2 target, which would allow us to determine the luminosity value. To reduce the statistical error and analyze the configuration with $\theta = 28°$ and higher (collected with a limited acceptance in the azimuthal angles), averaging over a more comprehensive angular range is prepared. Moreover, we plan to combine the current data with the data set collected in 2019, which should double our statistics. The data collected at a beam energy of 160 MeV will be, in turn, used for checking the observed pattern of (dis)agreements between the data and theories for three proton beam energies: 108, 135, and 160 MeV. The extension of the experimental program is also planned by supplementing the BINA detection system with the dedicated neutron detector made of plastic scintillator [86]. The simultaneous and direct measurement of the elastic scattering and the breakup reaction in FSI configuration of pp and pn pairs can give new insight into isospin role in nuclear interactions, also in the 3NF. It would allow direct impact of Coulomb and isospin in FSI regions, particularly sensitive to these effects.

Finally, we intend to compare the experimental results with other theoretical predictions including the Coulomb interaction, based on the different NN potential (Av18) and the Urbana-Illinois X (UIX) 3NF model. In addition, one of the most interesting ideas is to compare our results with the newly developed Chiral Effective Field Theory, which has been used to calculate the pd breakup reaction with 3NF only for the NNLO. Nevertheless, according to the presented results, we point out that the Coulomb interaction is significant, which indicates the necessity to include this part of dynamics into the ChEFT calculations.

Appendix A

Breakup cross section results

Appendix A contains all the differential cross section results for the ^{2}H(p,pp)n breakup reaction at the beam energy of 108 MeV obtained in the analysis described in this work. The results are collected in 9 panels in one figure corresponding to individual azimuthal angles φ_{12} from $20°$ to $180°$ and one combination of θ_1 and θ_2 specified in the caption. The legend is presented in panel 10th.
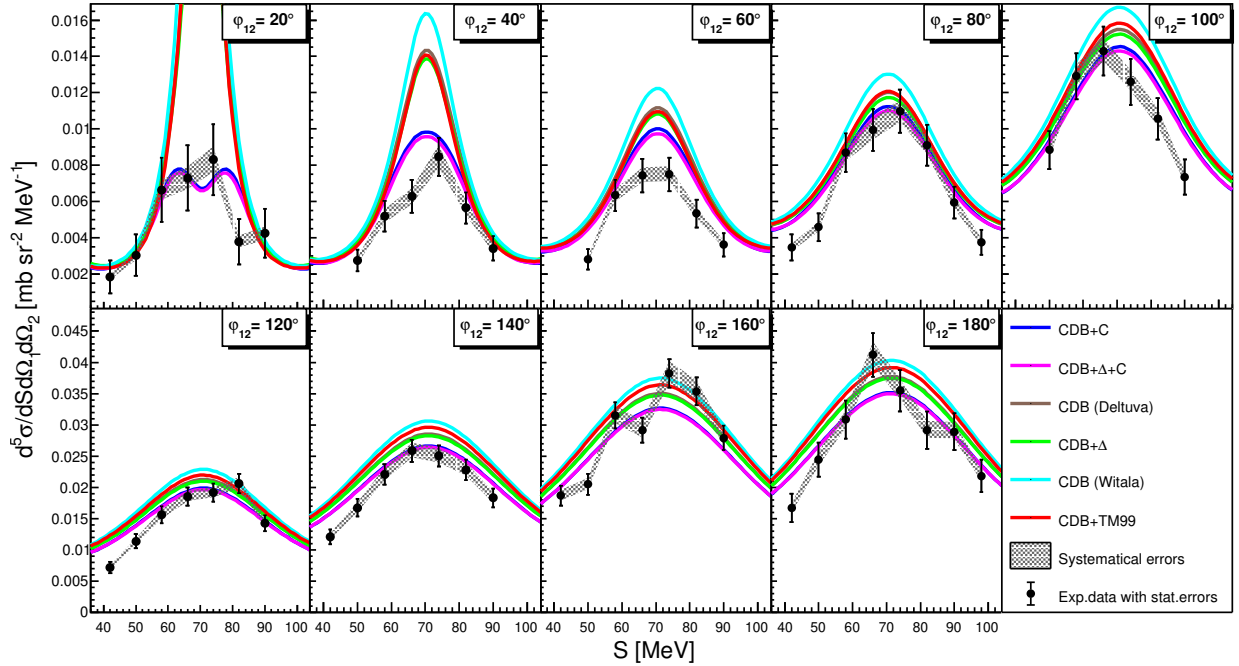

Fig. A.1: The differential cross section for pd breakup reaction obtained for polar angles $\theta_1 = 14°$ and $\theta_2 = 14°$ for different azimuthal angles φ_{12}. The black points represent the experimental data with statistical errors, and gray bands illustrate the systematic uncertainties. The available theoretical calculations are shown as a color lines, listed in the legend.
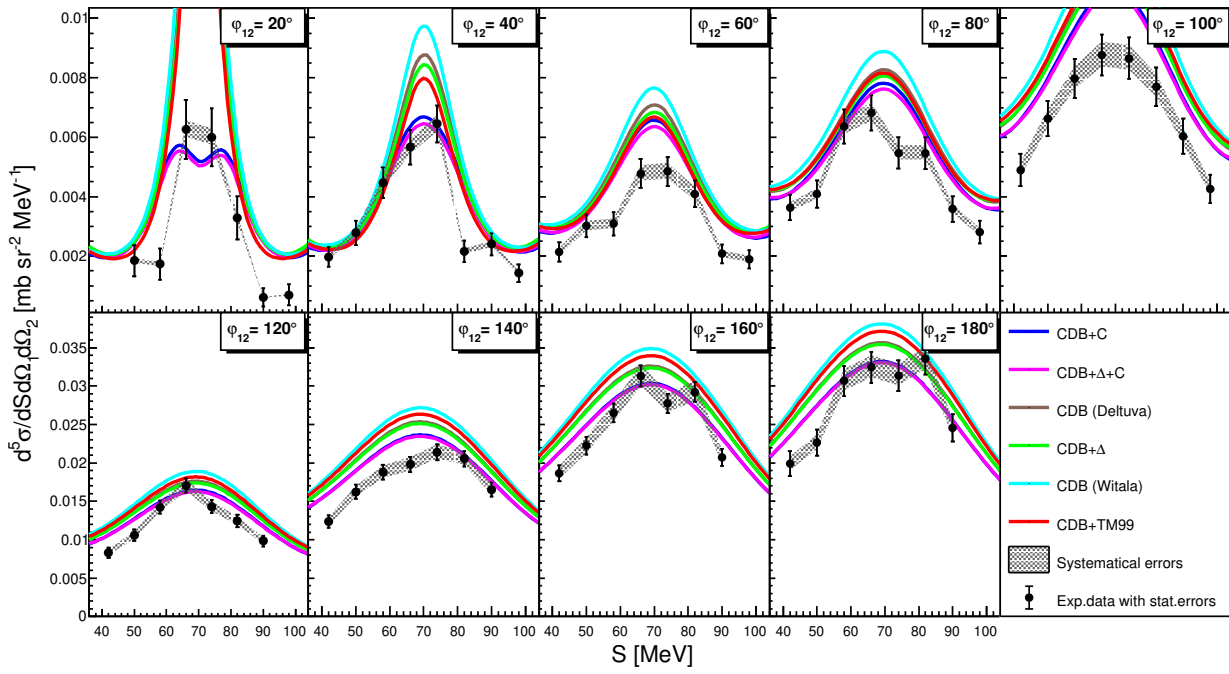
Fig. A.2: The same as Fig. A.1 but for polar angles $\theta_1 = 14°$ and $\theta_2 = 16°$.
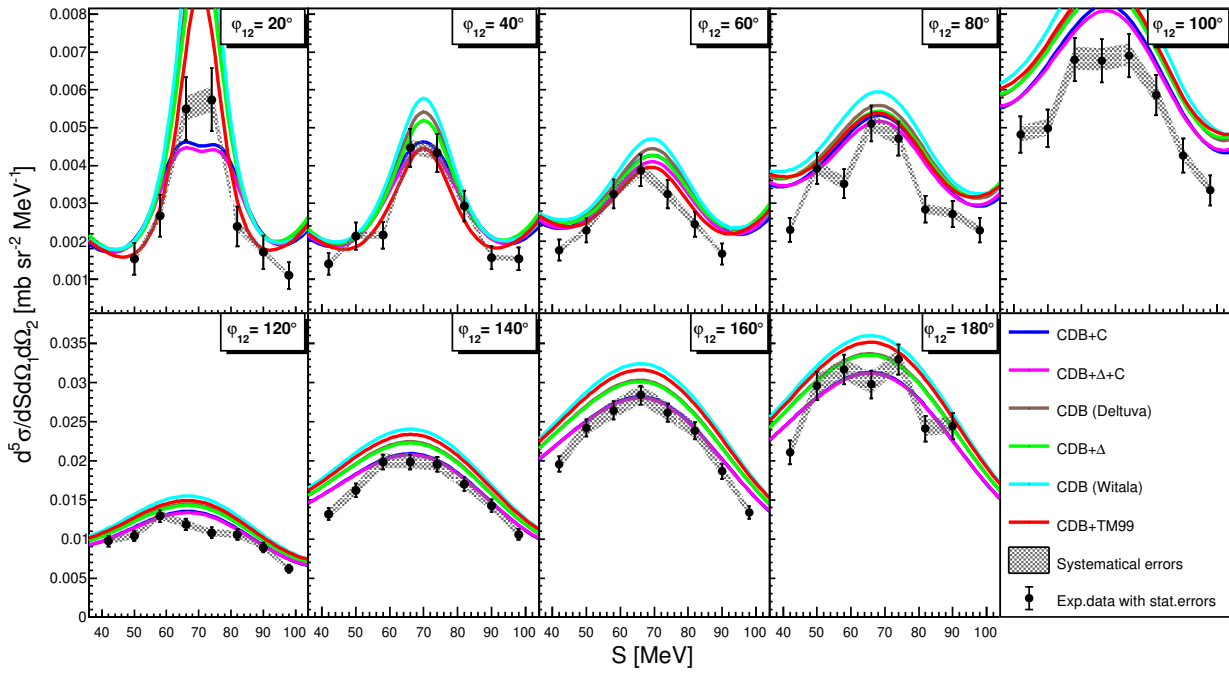
Fig. A.3: The same as Fig. A.1 but for polar angles $\theta_1 = 14°$ and $\theta_2 = 18°$.
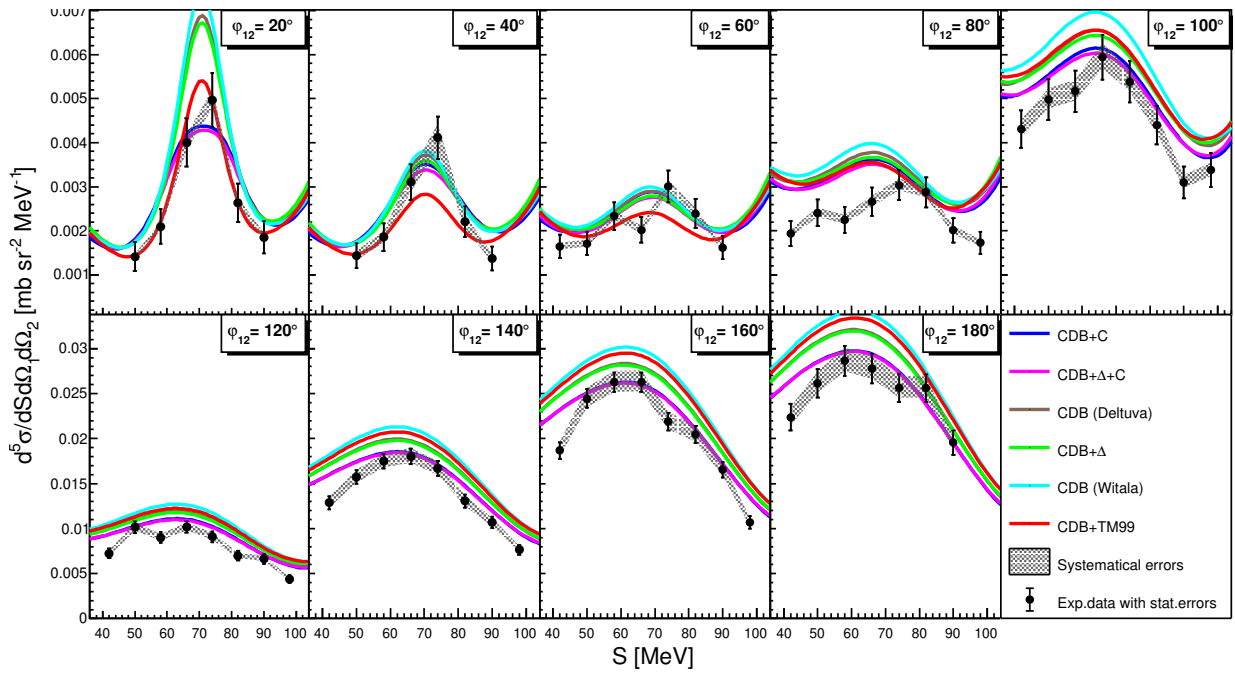
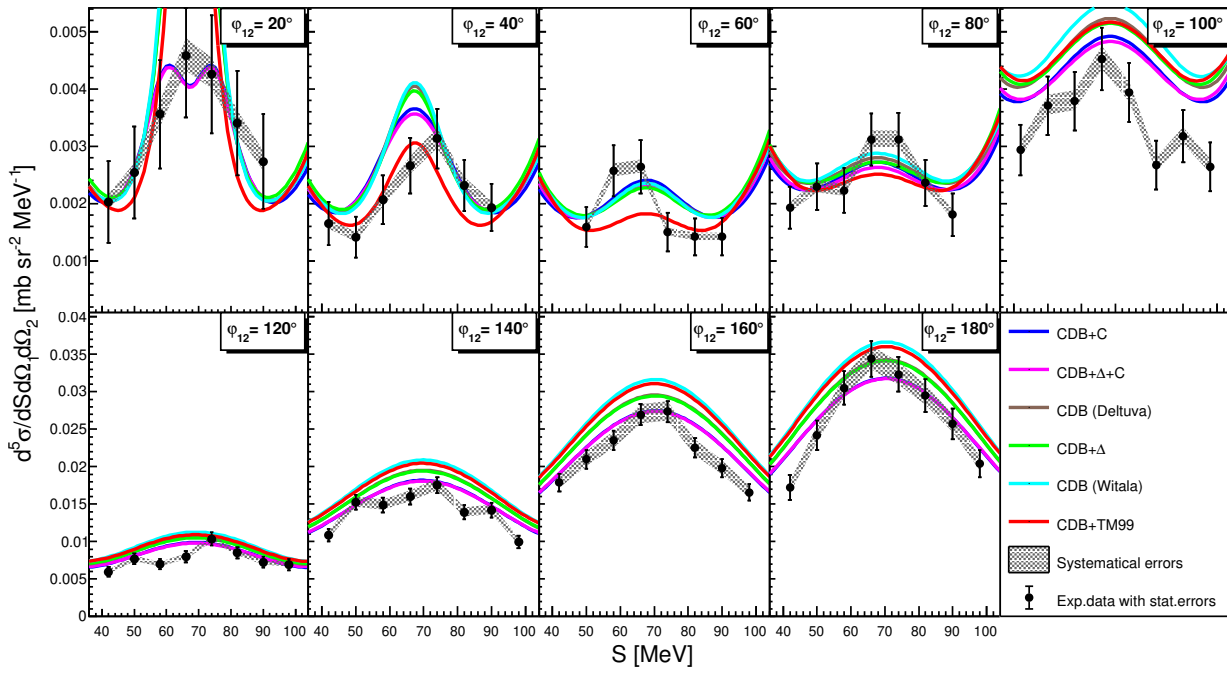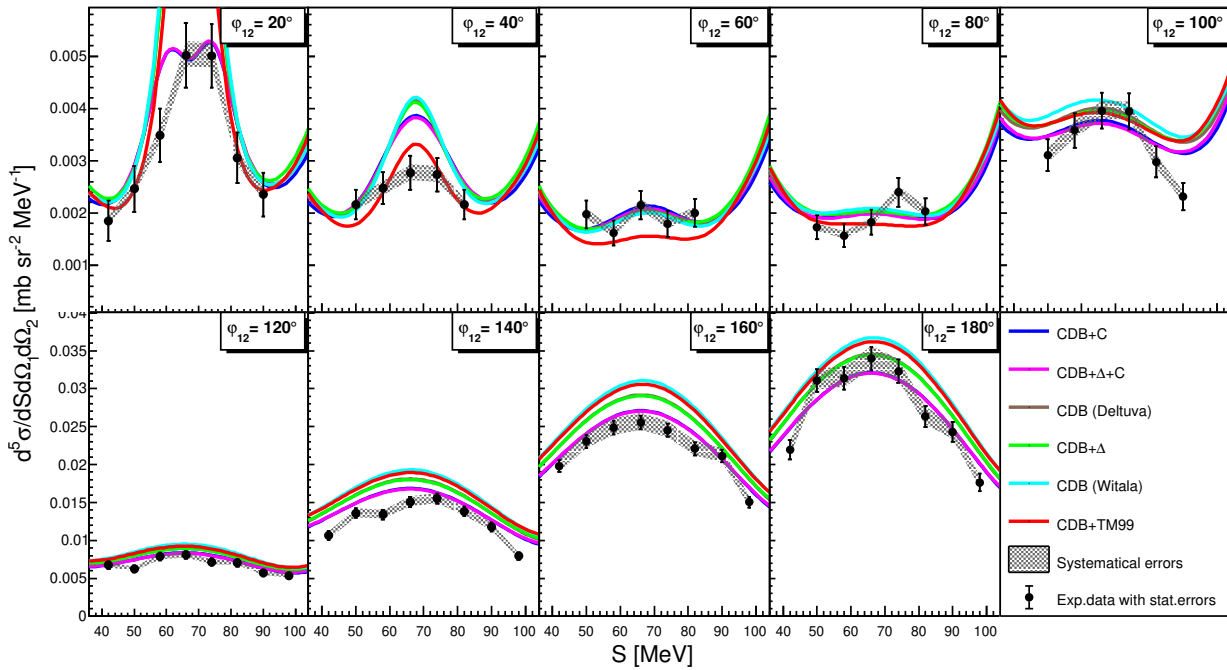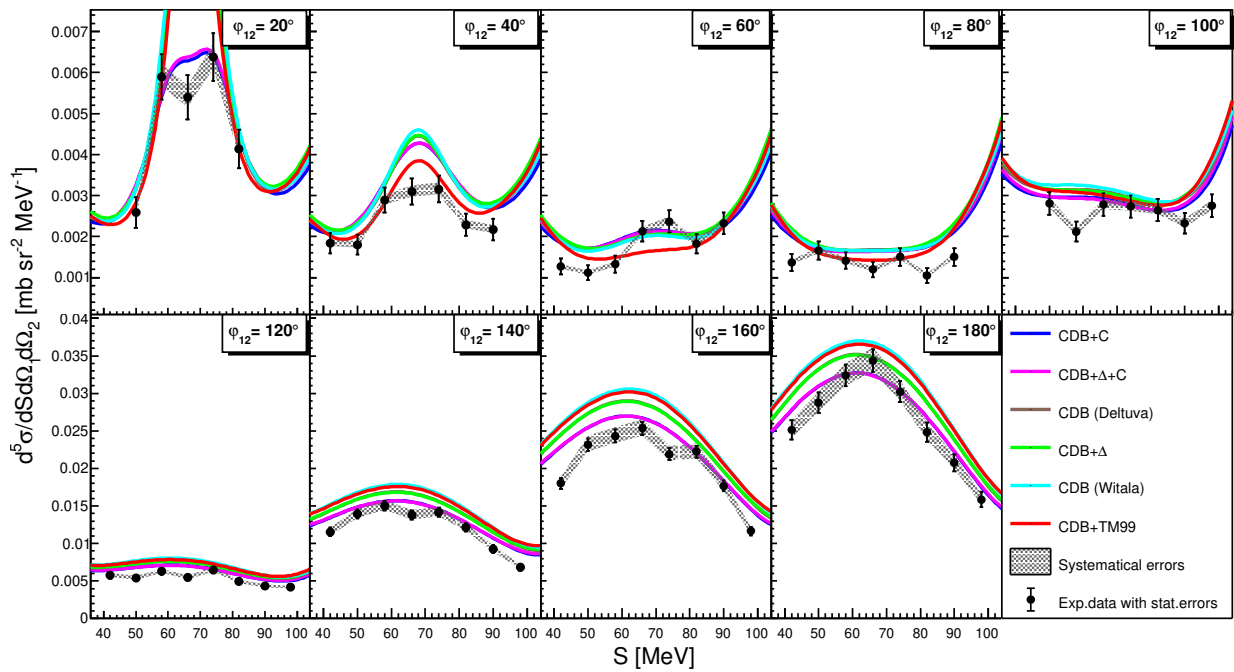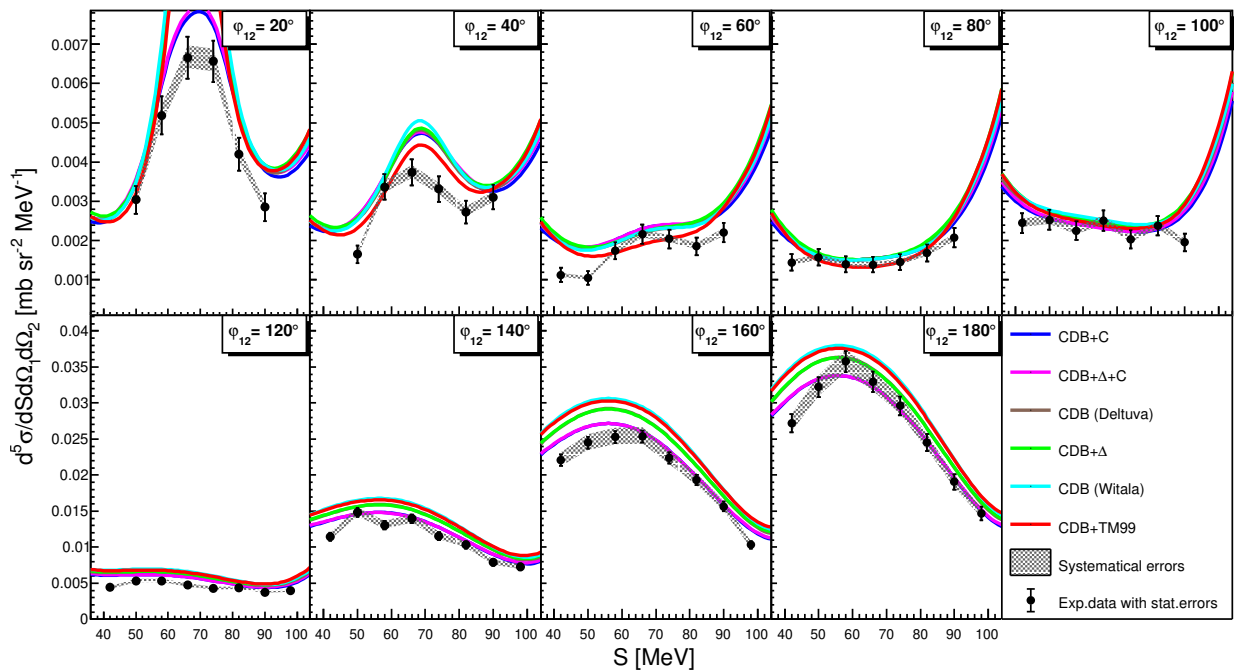**Fig. A.4:** The same as Fig. A.1 but for polar angles $\theta_1 = 14°$ and $\theta_2 = 20°$.
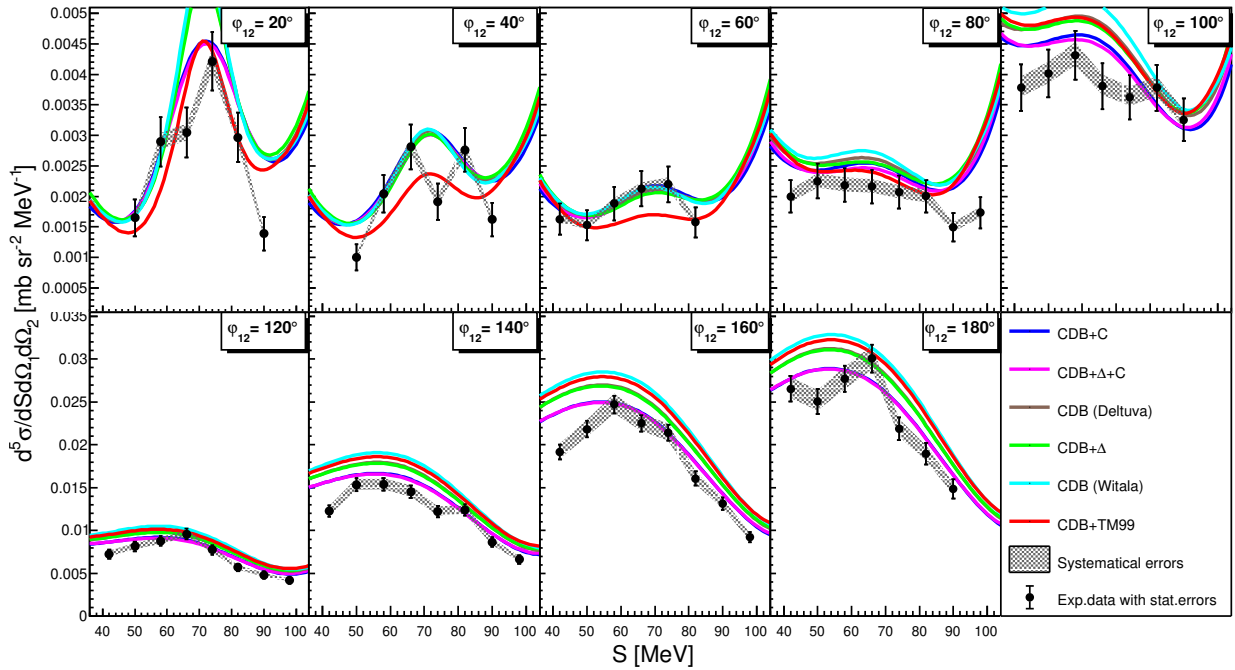
Fig. A.5: The same as Fig. A.1 but for polar angles $\theta_1 = 14°$ and $\theta_2 = 22°$.
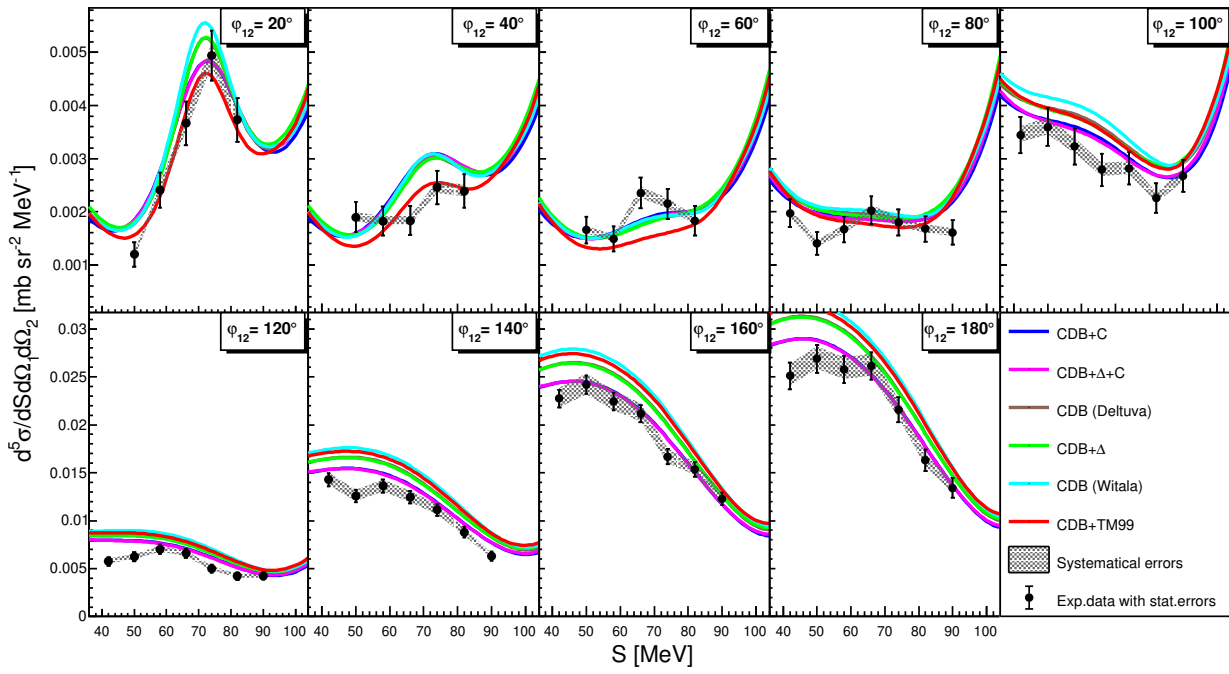
Fig. A.6: The same as Fig. A.1 but for polar angles $\theta_1 = 14°$ and $\theta_2 = 24°$.
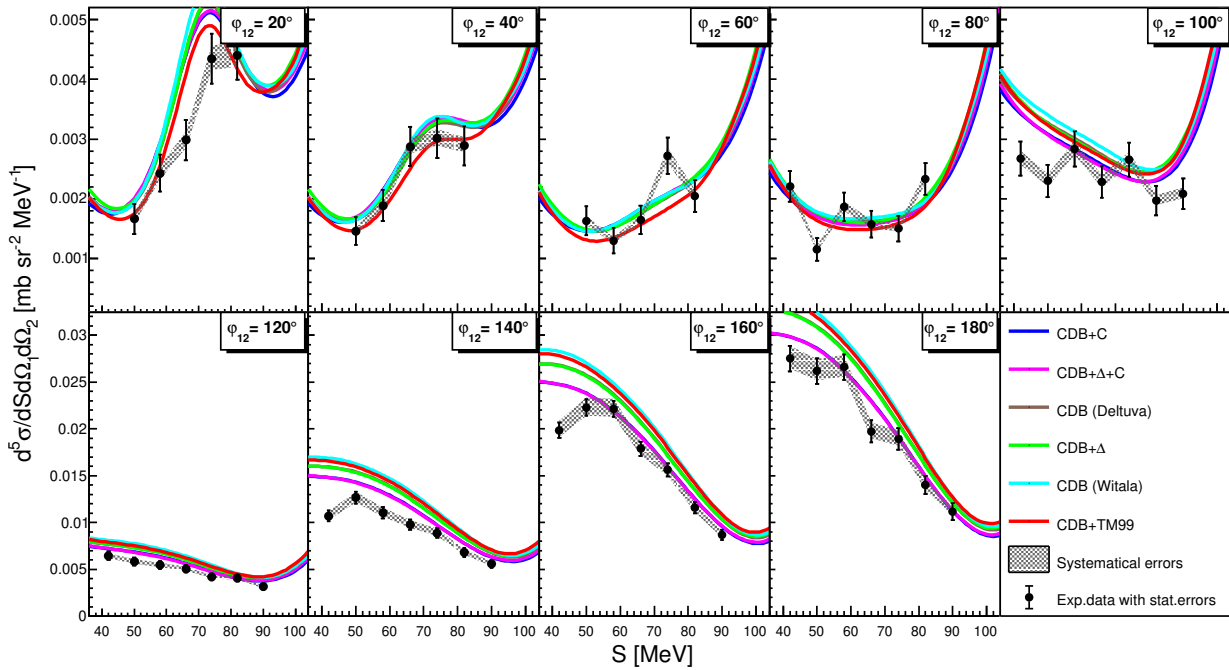
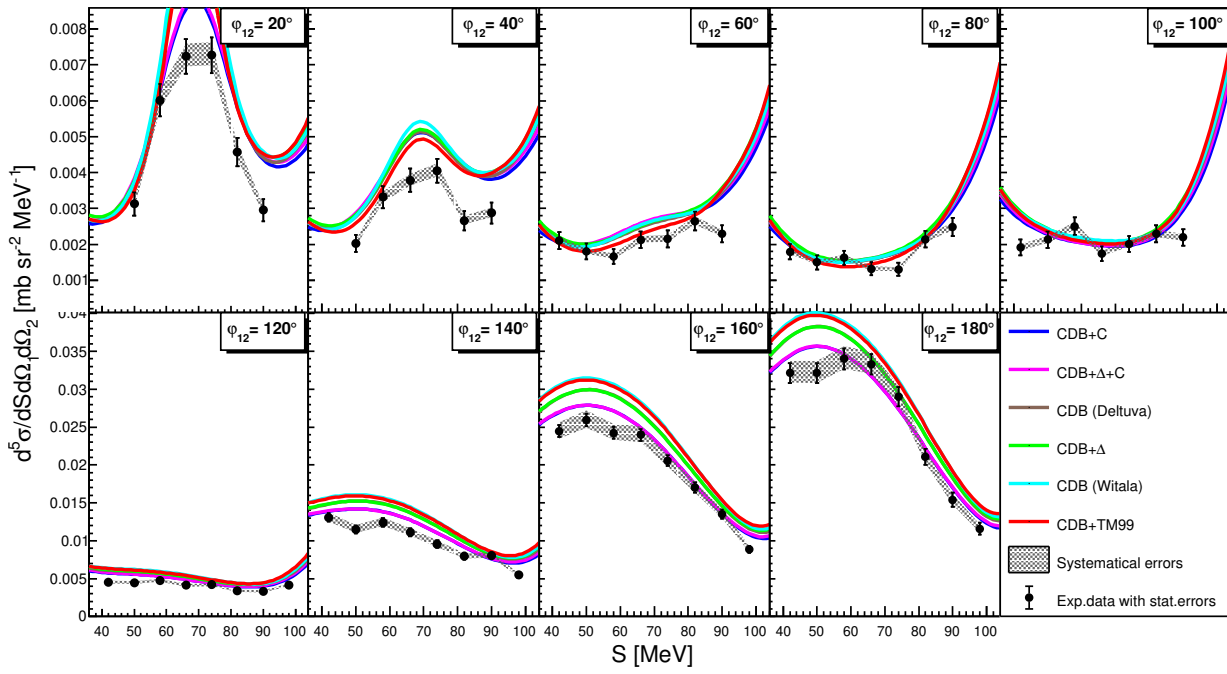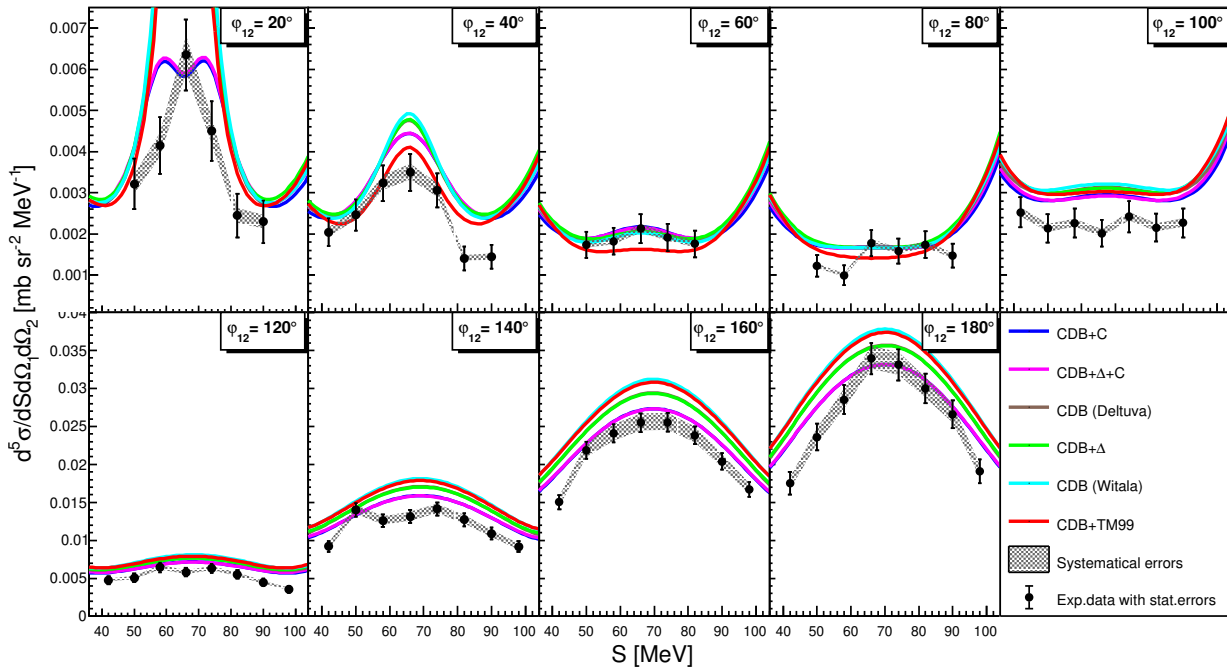
Fig. A.7: The same as Fig. A.1 but for polar angles $\theta_1 = 14°$ and $\theta_2 = 26°$.
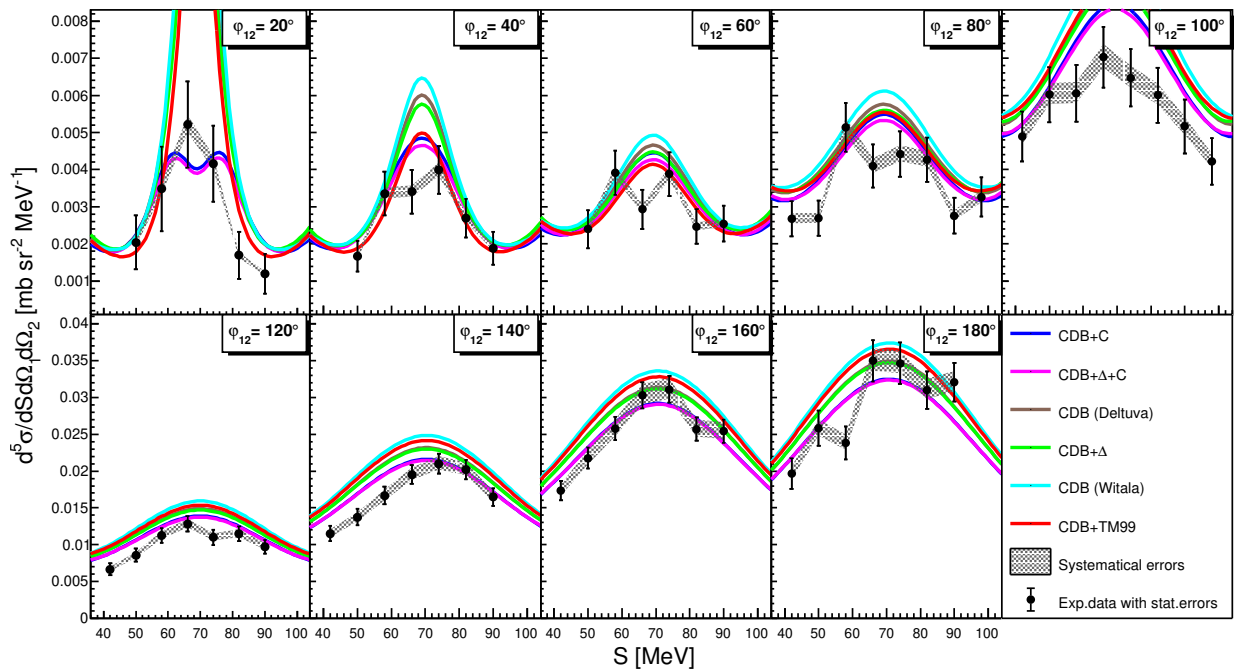
Fig. A.8: The same as Fig. A.1 but for polar angles $\theta_1 = 16°$ and $\theta_2 = 16°$.
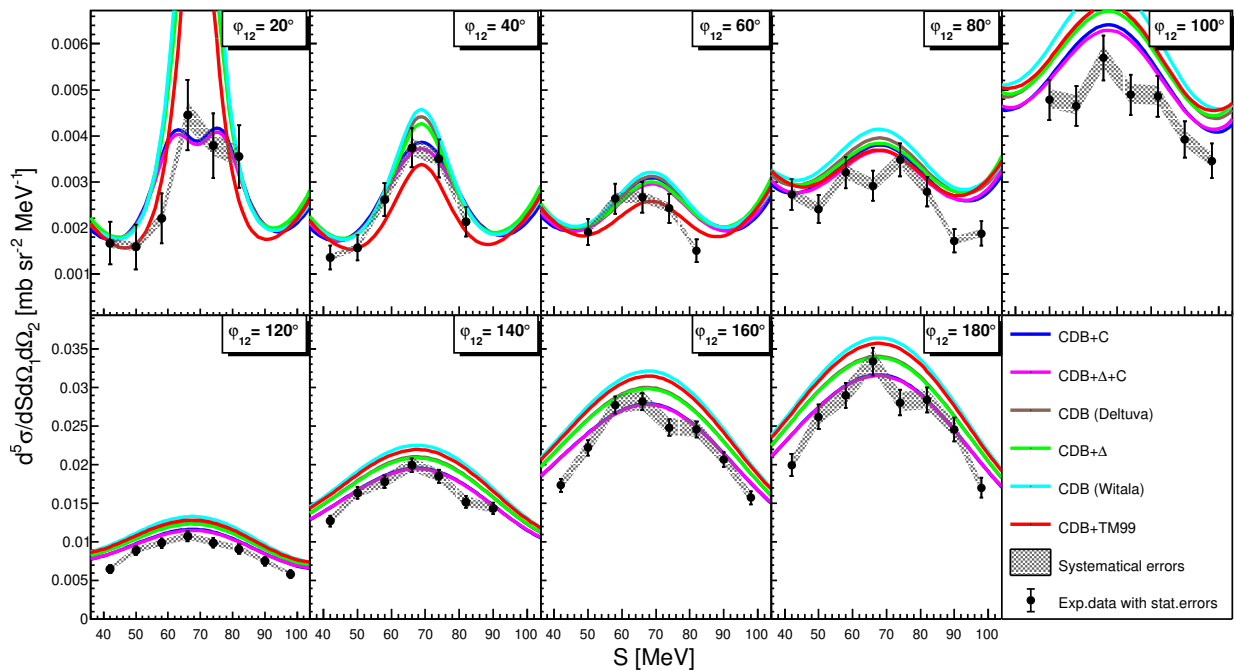
Fig. A.9: The same as Fig. A.1 but for polar angles $\theta_1 = 16°$ and $\theta_2 = 18°$.
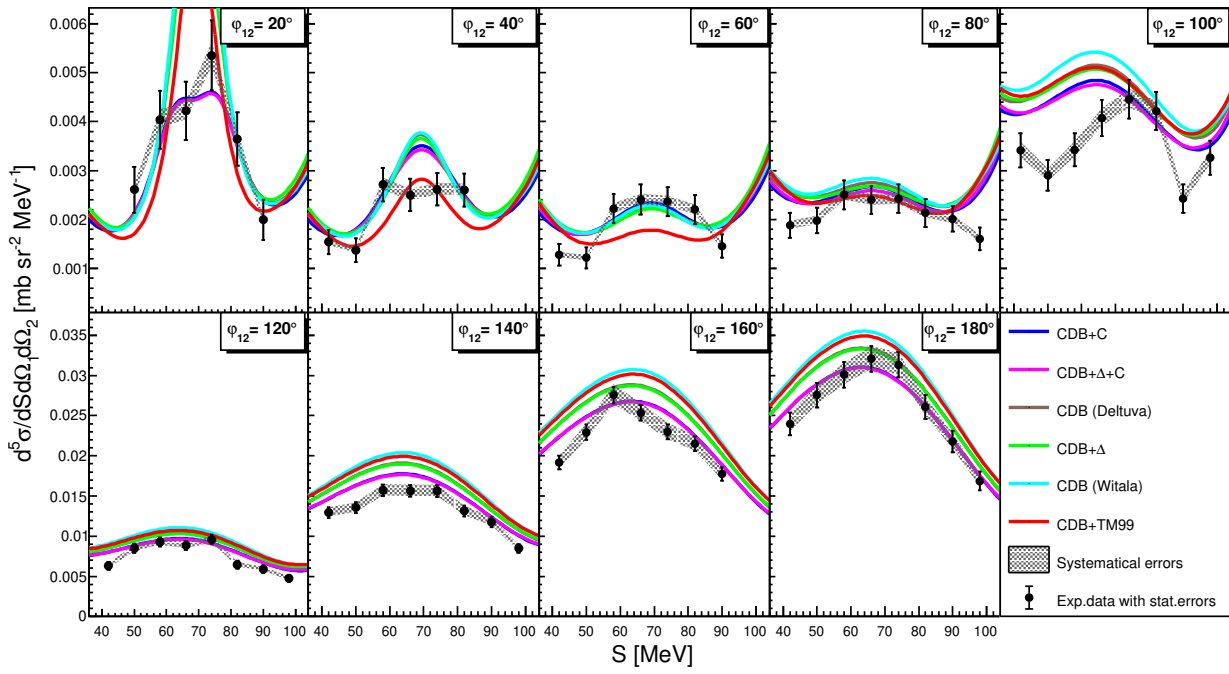
Fig. A.10: The same as Fig. A.1 but for polar angles $\theta_1 = 16°$ and $\theta_2 = 20°$.
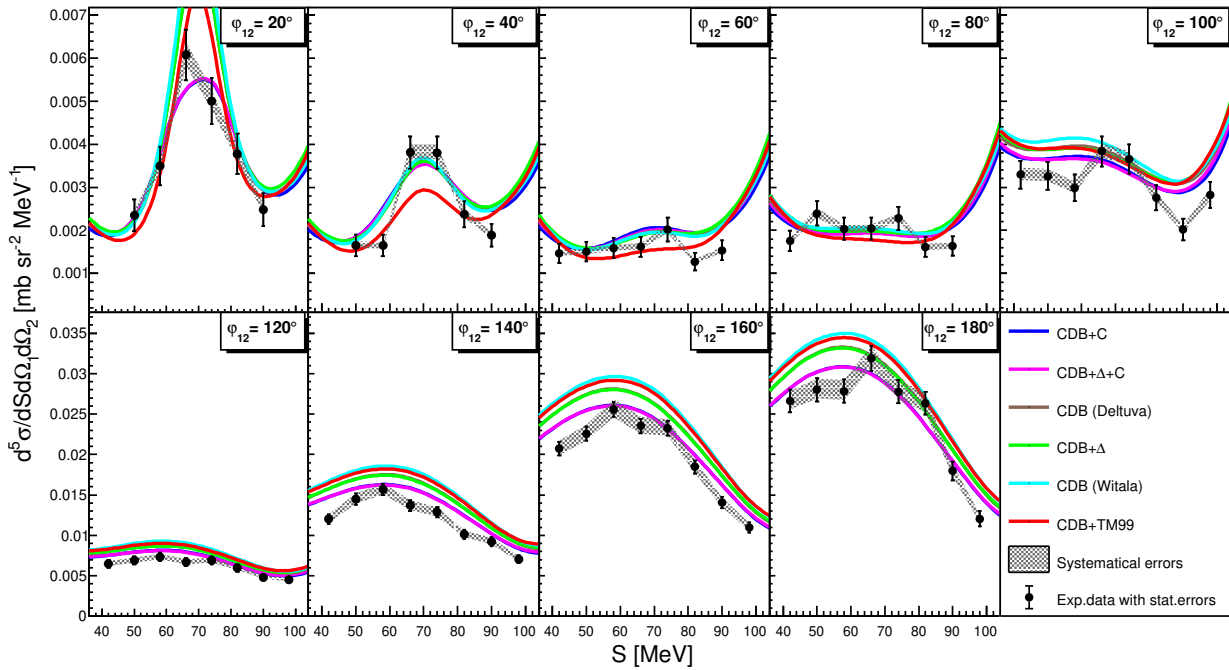
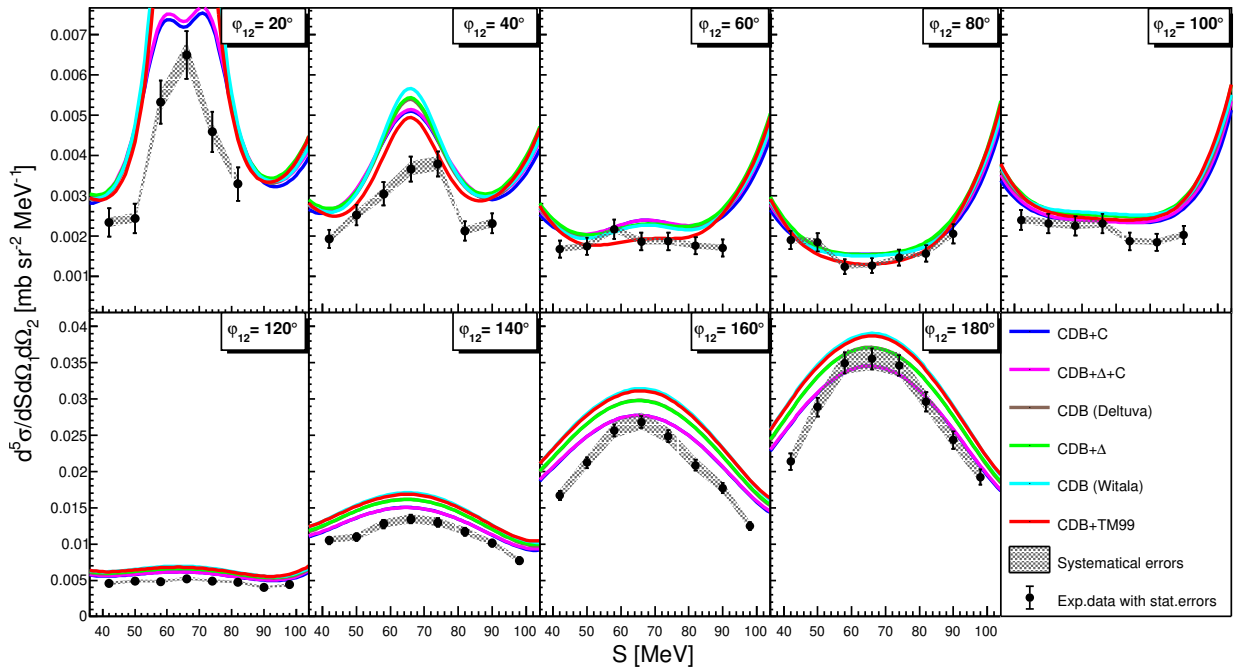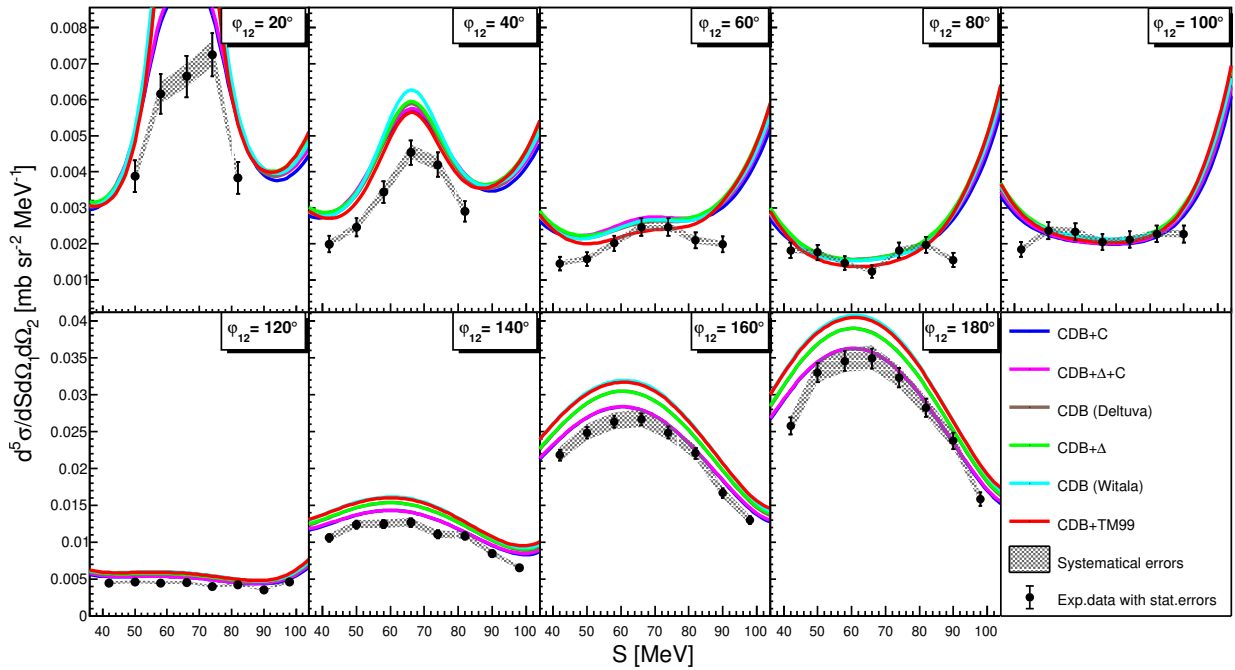

Fig. A.11: The same as Fig. A.1 but for polar angles $\theta_1 = 16°$ and $\theta_2 = 22°$.
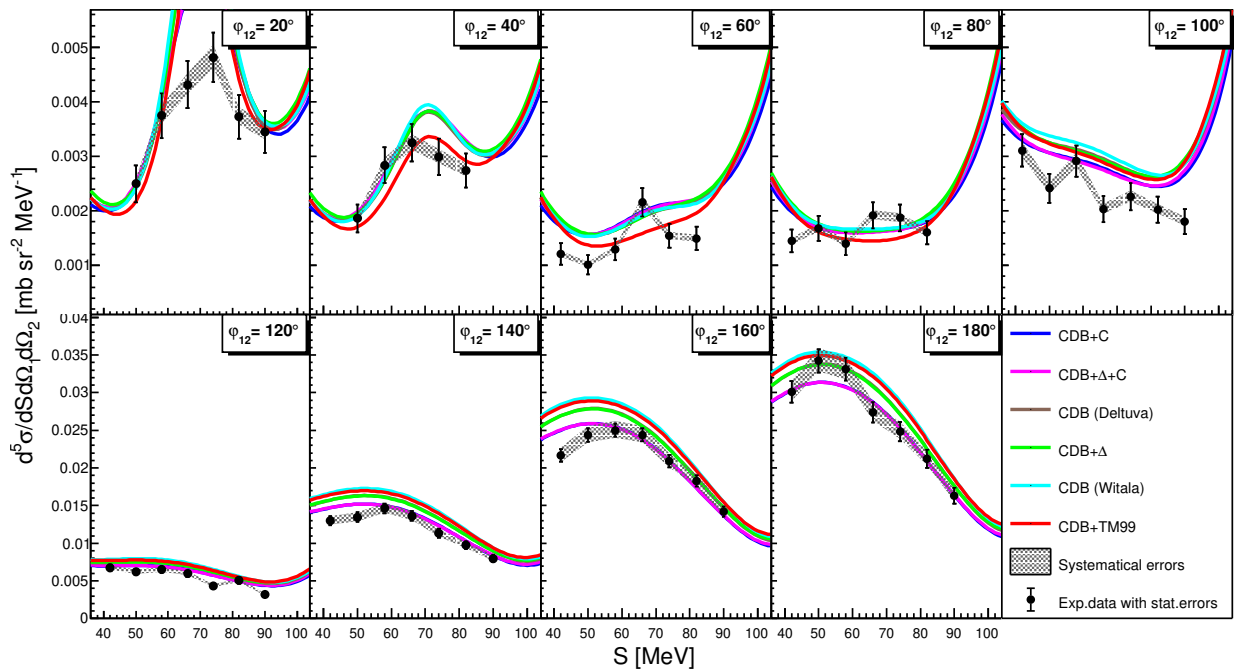
Fig. A.12: The same as Fig. A.1 but for polar angles $\theta_1 = 16°$ and $\theta_2 = 24°$.
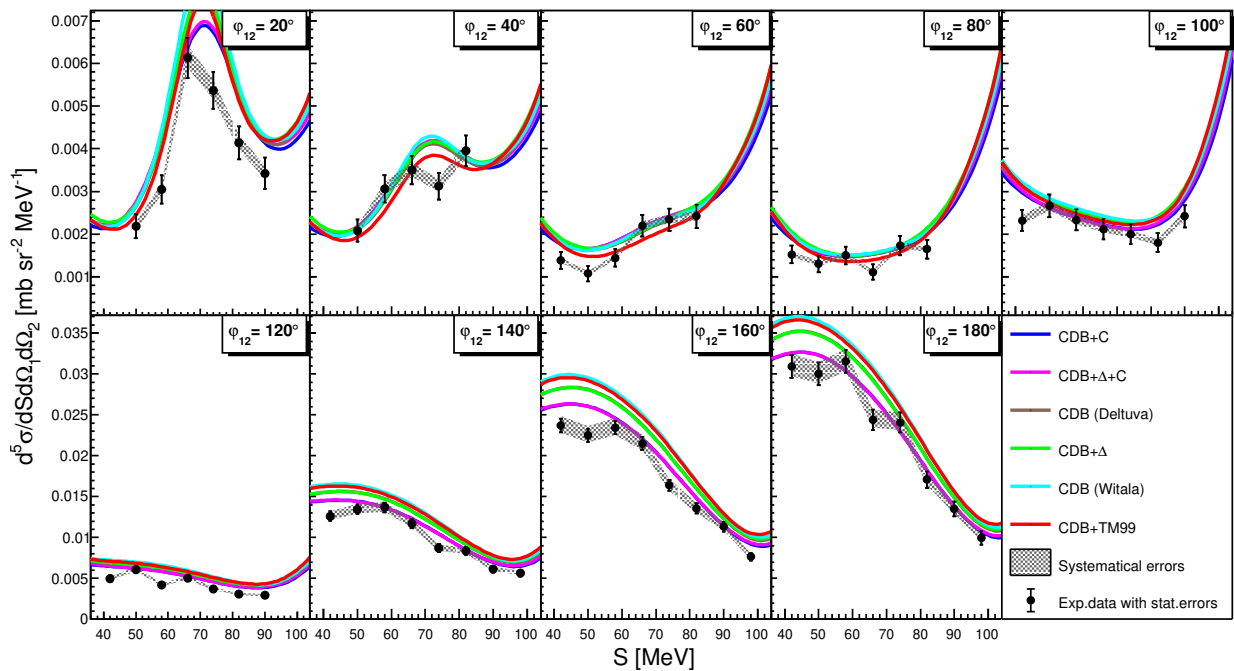
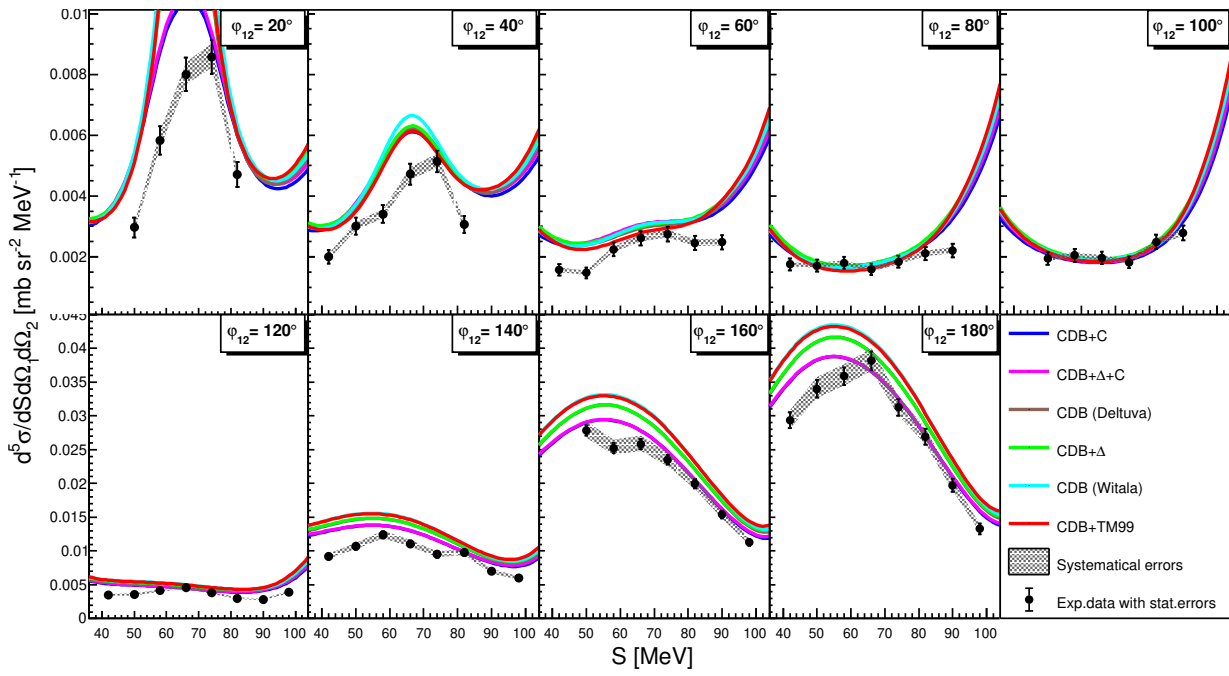

Fig. A.13: The same as Fig. A.1 but for polar angles $\theta_1 = 16°$ and $\theta_2 = 26°$.

Fig. A.14: The same as Fig. A.1 but for polar angles $\theta_1 = 18°$ and $\theta_2 = 18°$.

Fig. A.15: The same as Fig. A.1 but for polar angles $\theta_1 = 18°$ and $\theta_2 = 20°$.

Fig. A.16: The same as Fig. A.1 but for polar angles $\theta_1 = 18°$ and $\theta_2 = 22°$.

Fig. A.17: The same as Fig. A.1 but for polar angles $\theta_1 = 18°$ and $\theta_2 = 24°$.

Fig. A.18: The same as Fig. A.1 but for polar angles $\theta_1 = 18°$ and $\theta_2 = 26°$.

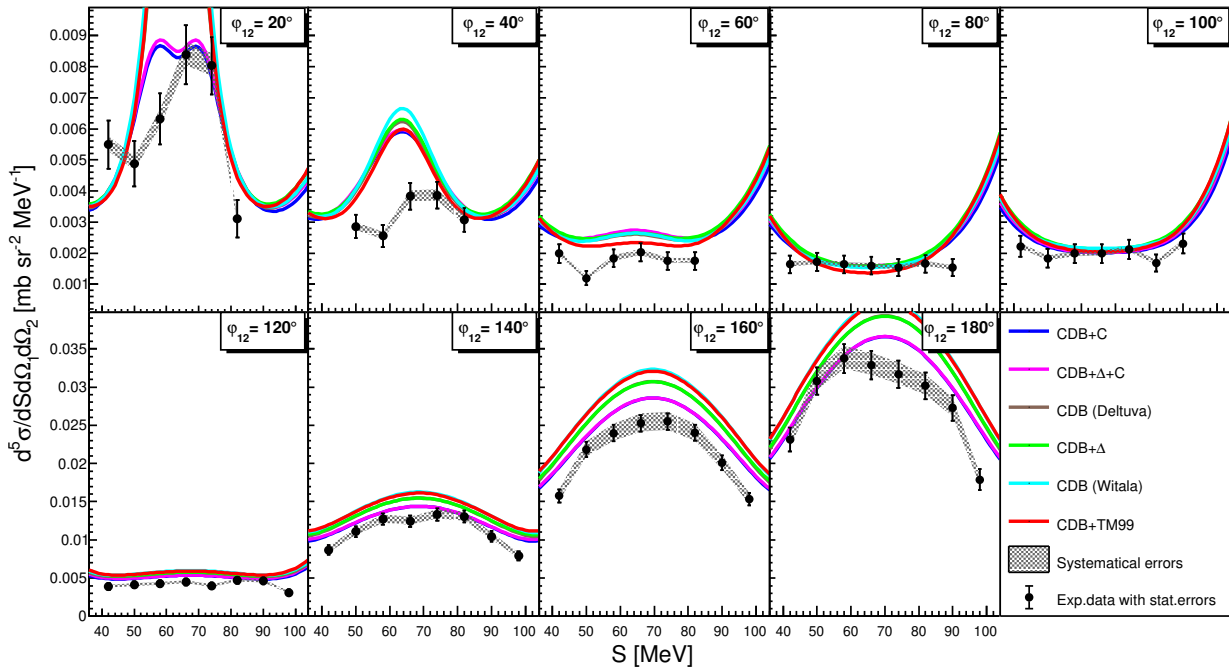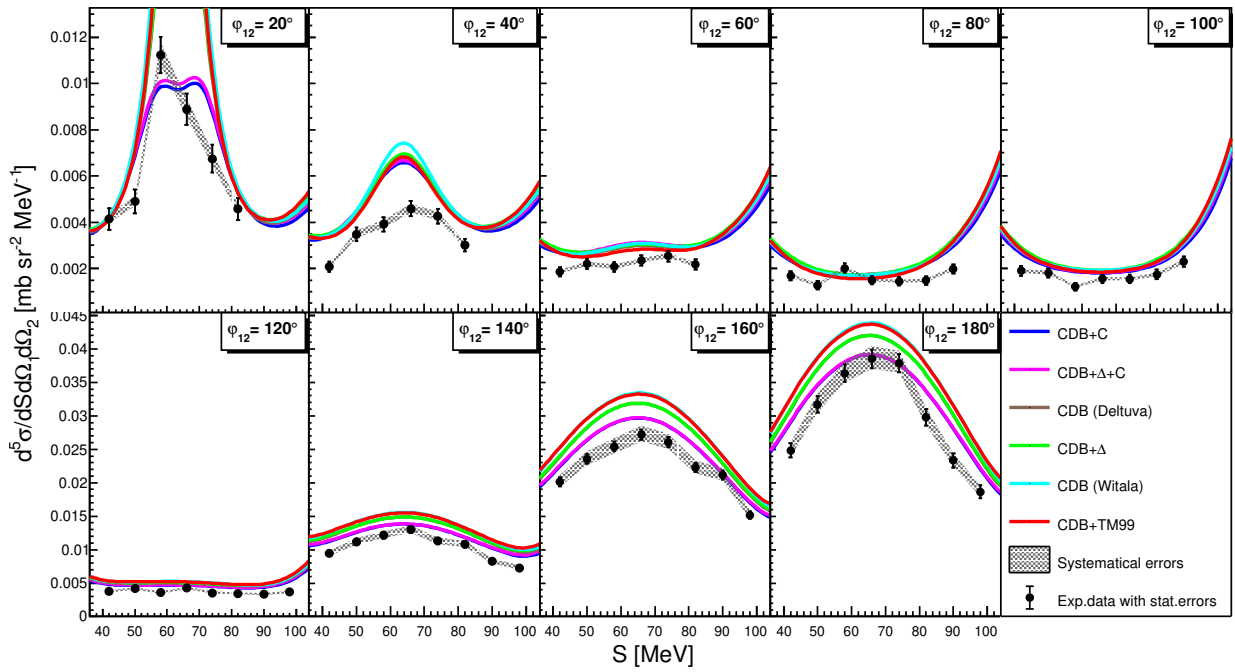**Fig. A.19:** The same as Fig. A.1 but for polar angles $\theta_1 = 20°$ and $\theta_2 = 20°$.

Fig. A.20: The same as Fig. A.1 but for polar angles $\theta_1 = 20°$ and $\theta_2 = 22°$.

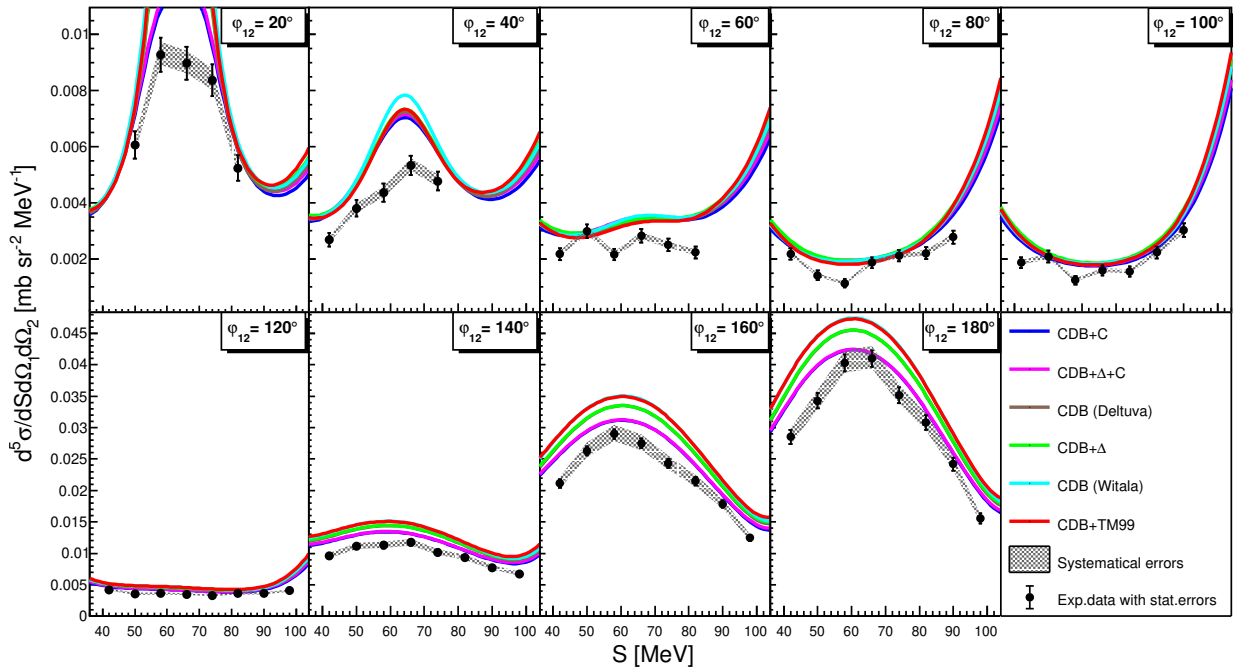**Fig. A.21:** The same as Fig. A.1 but for polar angles $\theta_1 = 20°$ and $\theta_2 = 24°$.

Fig. A.22: The same as Fig. A.1 but for polar angles $\theta_1 = 20°$ and $\theta_2 = 26°$.

Fig. A.23: The same as Fig. A.1 but for polar angles $\theta_1 = 22°$ and $\theta_2 = 22°$.

Fig. A.24: The same as Fig. A.1 but for polar angles $\theta_1 = 22°$ and $\theta_2 = 24°$.

Fig. A.25: The same as Fig. A.1 but for polar angles $\theta_1 = 22°$ and $\theta_2 = 26°$.

Fig. A.26: The same as Fig. A.1 but for polar angles $\theta_1 = 24°$ and $\theta_2 = 26°$.
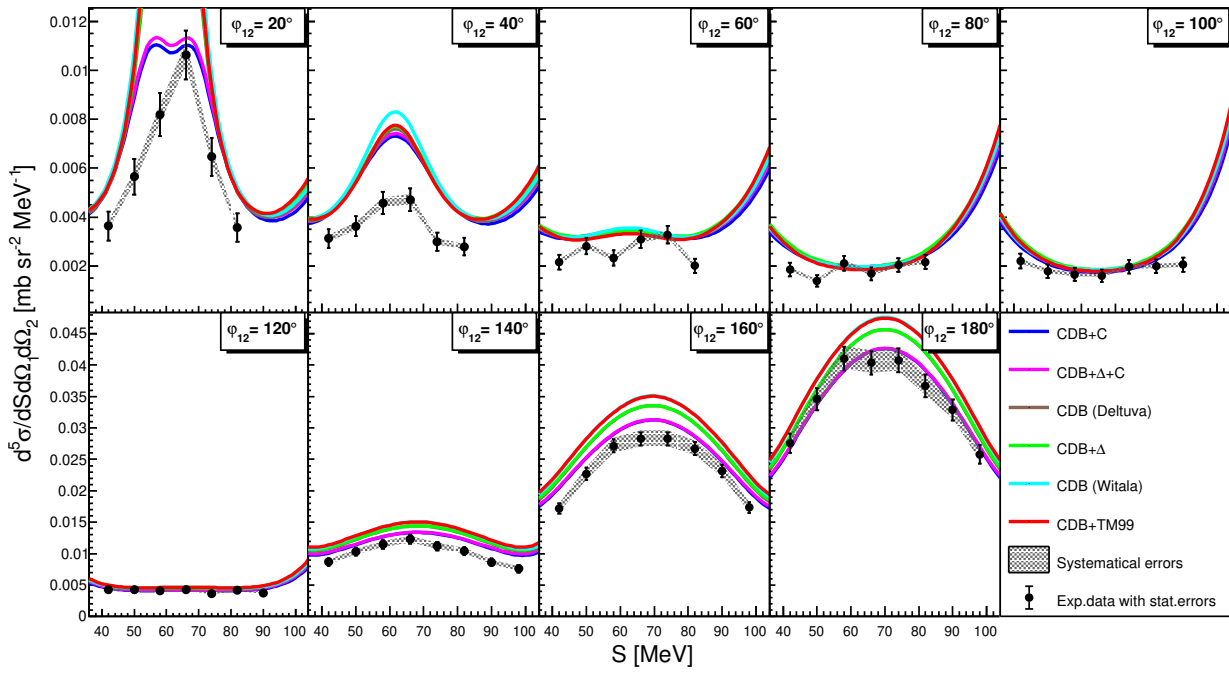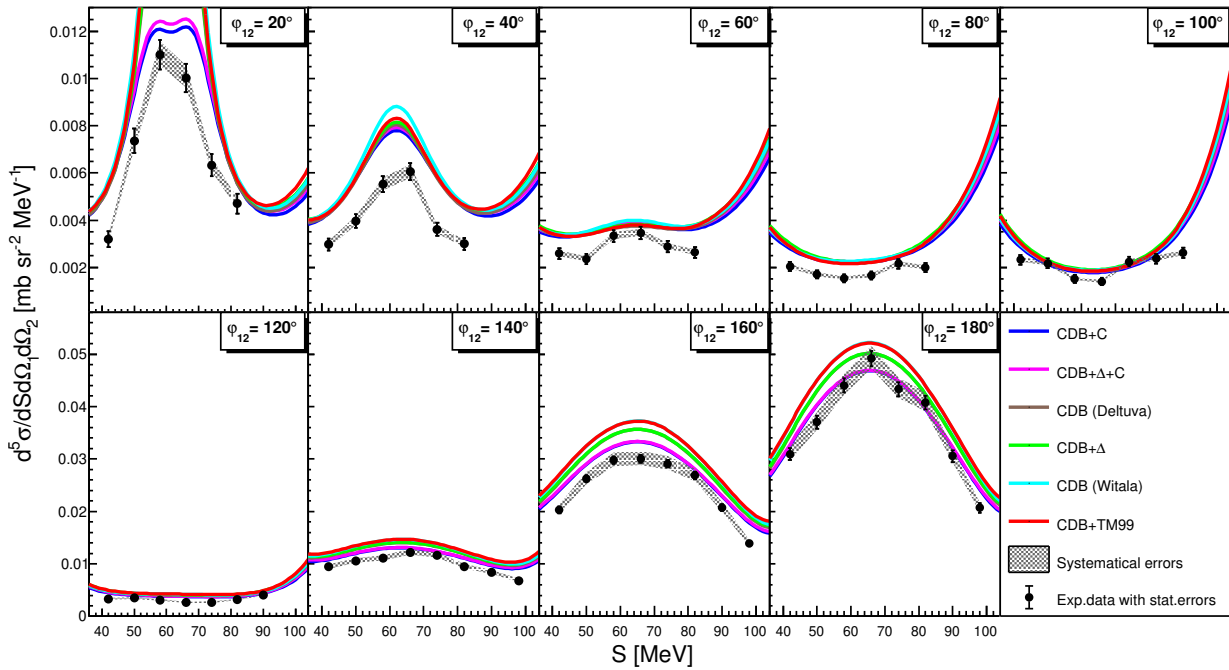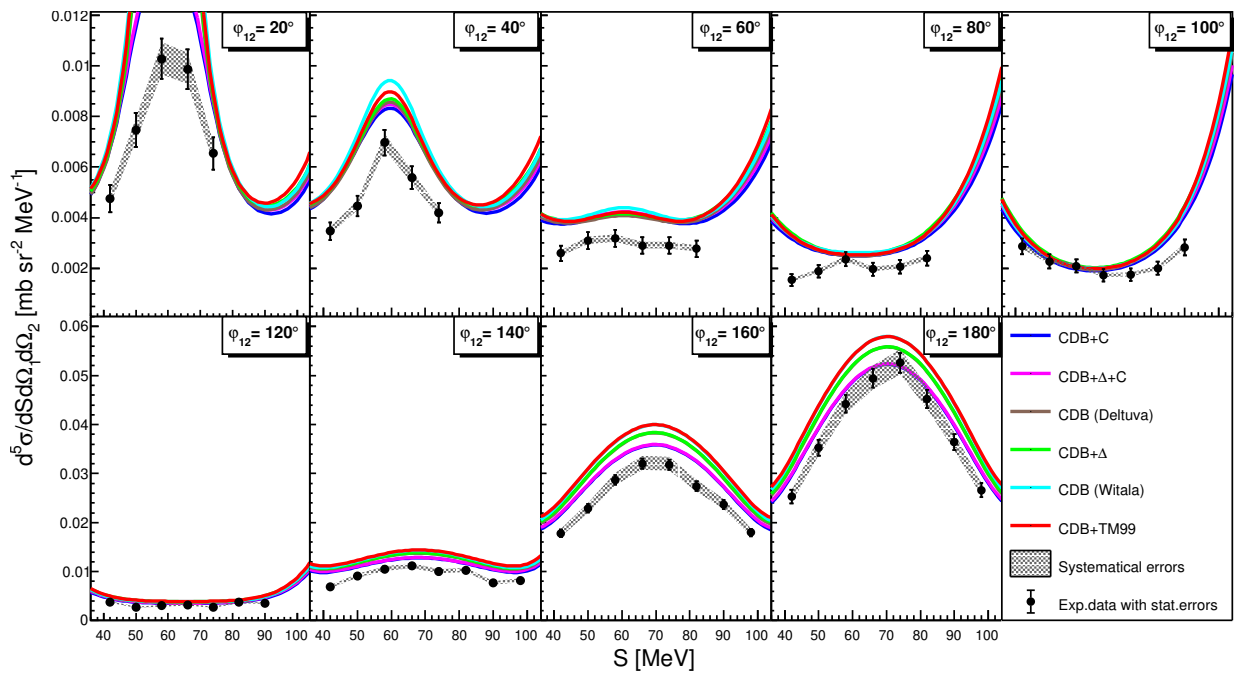

Fig. A.27: The same as Fig. A.1 but for polar angles $\theta_1 = 24°$ and $\theta_2 = 26°$.

Fig. A.28: The same as Fig. A.1 but for polar angles $\theta_1 = 26°$ and $\theta_2 = 26°$.

Acknowledgements

First of all, I would like to express my sincere gratitude to my supervisor **Dr. Hab. Elżbieta Stephan**, for the constant support and guidance throughout this project, without whom I would not have been able to complete this research. I am deeply grateful for all the fruitful discussions, comments, and her assistance at every stage of the research project. Her help with preparing and editing the manuscript was invaluable. I would like to also sincerely thank my co-supervisor, **Dr. Andrzej Wilczek**, who incredibly helped me with all aspects of my analysis and support me for all these years during my PhD studies. I wish to thank **Prof. Dr. Jan Kisiel** for enabling the doctoral dissertation realization in the nuclear physics group.

I would like to express my sincere thanks to **Prof. Dr. Stanisław Kistryn** and **Prof. Dr. Nasser Kalantar-Nayestanaki** for initiating a research program on the few-nucleon system. Moreover, I wish to thank all my colleagues from my research group:

Dr. Hab. Adam Kozela,

Dr. Hab. Barbara Kłos,

Dr. Hab. Jacek Zejma,

Dr. Hab. Izabela Ciepał,

Dr. Paweł Kulessa,

Dr. Bogusław Włoch,

Dr. Wiktor Parol,

Dr. Izabela Skwira-Chalot,

M.Sc. Albert Szadziński,

with whom I spent a lot of wonderful time preparing and performing the experiments. Thank you for the valuable discussions and great working atmosphere!

I wish to thank my beloved husband, **Dr. Marcin Łobejko**, for his incredible support and engagement in my research. Thank you for showing me the beauty of science and inspiring me to seek the truth.

I would like to express my sincere thanks to my supportive parents, who motivated me to apply and finish my PhD studies. Last but not least, I would like to extend my sincere thanks to my dearest friend **Sylwia Sałacińska**, all my sisters, and many other colleagues for their unwavering support and belief in me.

Bibliography

[1] H. Yukawa, Proc. Phys. Math. Soc., Jpn. **17**, 48 (1935).

[2] E. Epelbaum et al., Rev. Mod. Phys. **81**, 1773 (2009).

[3] A. Nogga et al., Phys. Rev. C **67**, 034004 (2003).

[4] P. Reinert et al., Eur. Phys. J. A **54**, 86 (2018).

[5] E. Epelbaum et al., Front. in Phys. **8**, 98 (2020).

[6] E. Epelbaum et al., Eur. Phys. J. A **56**, 92 (2020).

[7] D. R. Entem et al., Phys. Rev. C **96**, 024004 (2017).

[8] H. Witała et al., Phys. Rev. Lett. **81**, 1183 (1998).

[9] P. Mermod et al., Phys. Lett. B **597**, 243 (2004).

[10] A. Nogga et al., Phys. Rev. Lett. **85**, 944 (2000).

[11] A. Ramazani-Moghaddam-Arani et al., Phys. Rev. C **78**, 014006 (2008).

[12] H. Witała et al., Phys. Lett. B **634**, 374 (2006).

[13] R. Skibiński et al., Eur. Phys. J. A **30**, 369 (2006).

[14] H. Witała et al., Few-Body Syst. **49**, 61 (2011).

[15] H. Sakai et al., Phys. Rev. Lett. **84**, 5288 (2000).

[16] K. Sekiguchi et al., Phys. Rev. C **70**, 014001 (2004).

[17] K. Ermisch et al., Phys. Rev. Lett. **86**, 5862 (2001).

[18] A. Deltuva et al., Phys. Rev. C **72**, 054004 (2005).

[19] A. Deltuva et al., Phys. Rev. C **73**, 057001 (2006).

[20] A. Deltuva, Phys. Rev. C **80**, 064002 (2009).

[21] S. Kistryn et al., Phys. Rev. C **68**, 054004 (2003).

[22] S. Kistryn et al., Phys. Rev. C **72**, 044006 (2005).

[23] W. Parol et al., Phys. Rev. C **102**, 054002 (2020).

[24] S. Kistryn et al., Phys. Lett. B **641**, 23 (2006).

[25] S. Kistryn et al., J. Phys. G: Nucl. Part. Phys. **40**, 063101 (2013).

[26] I. Ciepał et al., Few-Body Syst. **56**, 665 (2015).

[27] P. Adlarson et al. (WASA-at-COSY Collaboration), Phys. Rev. C **101**, 044001 (2020).

[28] S. Kistryn et al., Nucl. Phys. A **548**, 49 (1992).

[29] M. Allet et al., Phys. Rev. C **50**, 602 (1994).

[30] M. Allet et al., Few-Body Syst. **20**, 27 (1996).

[31] J. Zejma et al., Phys. Rev. C **55**, 42 (1997).

[32] K. Bodek et al., Nucl. Phys. A, 687 (Mar 1998).

[33] I. Ciepał, "Investigation of the deuteron breakup on protons in the forward angular region", PhD thesis (Jagiellonian University, 2010).

[34] I. Ciepał et al., Phys. Rev. C **85**, 017001 (2012).

[35] E. Stephan et al., Phys. Rev. C **82**, 014003 (2010).

[36] E. Stephan et al., Eur. Phys. J. A **49**, 36 (2013).

[37] B. Włoch, "Studies of three-nucleon force effects in the $^1H(d, pn)p$ breakup reaction at 160 MeV", PhD thesis (Polish Academy of Sciences, 2021).

[38] M. Eslami-Kalantari et al., Mod. Phys. Lett. A **24**, 839 (2009).

[39] M. T. Bayat et al., Eur. Phys. J. A **56**, 249 (2020).

[40] H. Tavakoli-Zaniani et al., Eur. Phys. J. A **56** (2020).

[41] H. Mardanpour, "Investigation of nuclear forces in d+p elastic and p+d break-up reactions at intermediate energies", PhD thesis (University of Groningen, 2008).

[42] M. Mohammadi-Dadkan et al., Eur. Phys. J. A **56**, 81 (2020).

[43] K. Ermisch et al., Phys. Rev. C **71**, 064004 (2005).

[44] L. Faddeev et al., JETP **12**, 1014 (1961).

[45] R. Machleidt et al., Phys. Rev. C **53**, R1483 (1996).

[46] R. Machleidt, Phys. Rev. C **63**, 024001 (2001).

[47] R. B. Wiringa et al., Phys. Rev. C **51**, 38 (1995).

[48] V. G. J. Stoks et al., Phys. Rev. C **49**, 2950 (1994).

[49] M. Elbistan et al., J. Phys. G: Nucl. Part. Phys. **45**, 105103 (2018).

[50] J.-i. Fujita et al., Prog. Theor. Phys. **17**, 360 (1957).

[51] S. Kistryn, "Three-nucleon force effects in the deuteron-proton breakup reaction", habilitation (Jagiellonian University, 2005).

[52] S. A. Coon et al., Phys. Rev. C **23**, 1790 (1981).

[53] H. T. Coelho et al., Phys. Rev. C **28**, 1812 (1983).

[54] S. A. Coon et al., Few-Body Syst. **30**, 131 (2001).

[55] A. Nogga et al., Phys. Lett. B **409**, 19 (1997).

[56] B. S. Pudliner et al., Phys. Rev. C **56**, 1720 (1997).

[57] S. C. Pieper et al., Phys. Rev. C **64**, 014001 (2001).

[58] J. Carlson et al., Rev. Mod. Phys. **87**, 1067 (2015).

[59] D. Lonardoni et al., Phys. Rev. C **96**, 024326 (2017).

[60] A. Deltuva et al., Phys. Rev. C **67**, 034001 (2003).

[61] A. Deltuva et al., Phys. Rev. C **68**, 024005 (2003).

[62] E. Epelbaum et al., Phys. Rev. C **66**, 064001 (2002).

[63] E. Epelbaum et al., Nucl. Phys. A **747**, 362 (2005).

[64] S. Weinberg, Phys. Lett. B **251**, 288 (1990).

[65] S. Weinberg, Nucl. Phys. B **363**, 3 (1991).

[66] `https://www.lenpic.org`.

[67] E. Epelbaum et al., Eur. Phys. J. A **51**, 53 (2015).

[68] K. Sekiguchi et al., Phys. Rev. C **65**, 034003 (2002).

[69] `https://experimentsccb.ifj.edu.pl`.

[70] H. Mardanpour et al., Phys. Lett. B **687**, 149 (2010).

[71] G. Khatri, "Investigation of deuteron disintegration", PhD thesis (Jagiellonian University, 2015).

[72] M. Volkerts et al., Nucl. Instrum. Meth. A **428**, 432 (1999).

[73] R. Bitter et al., *Labview: advanced programming techniques* (Crc Press, 2006).

[74] N. Kalantar-Nayestanaki et al., Nucl. Instrum. Meth. A **417**, 215 (1998).

[75] R. Brun et al., Nucl. Instrum. Meth. A **389**, 81 (1997).

[76] J. Allison et al., Nucl. Instrum. Meth. A **835**, 186 (2016).

[77] W. Nowak, "Analiza własności układu detekcyjnego BINA w pomiarach reakcji rozszczepienia deuteronu", MA thesis (Jagiellonian University, 2005).

[78] A. Wilczek, "Simulations of BINA experimental setup for studies of three nucleon system", MA thesis (University of Silesia, 2010).

[79] G. O'Rielly et al., Nucl. Instrum. Meth. A **368**, 745 (1996).

[80] L. Reichhart et al., Phys. Rev. C **85**, 065801 (2012).

[81] D. Maier et al., EPJ Web of Conferences **225**, 01003 (2020).

[82] W. T. Eadie et al., *Statistical methods in experimental physics; 1st ed.* (North-Holland, Amsterdam, 1971).

[83] I. Ciepał et al., Phys. Rev. C **100**, 024003 (2019).

[84] R. Barlow, eConf **C030908**, edited by L. Lyons et al., WEMT002 (2003).

[85] H. Tavakolizaniani, "Proton-deuteron break-up studies with BINA and a review of three-nucleon database", PhD thesis (University of Groningen, 2020).

[86] A. Łobejko, PRELUDIUM NCN: 2020/37/N/ST2/02360.